A Model Elastomer with Modular Metal-Ligand Crosslinking

by

Patricia Nicole Johnson

Department of Chemistry
Duke University

Date:_____

Approved:

_____
Stephen L. Craig, Supervisor

_____
Katherine J. Franz

_____
David N. Beratan

_____
Ross A. Widenhoefer

Dissertation submitted in partial fulfillment of
the requirements for the degree of Doctor
of Philosophy in the Department of
Chemistry in the Graduate School
of Duke University

2022

ABSTRACT

A Model Elastomer with Modular Metal-Ligand Crosslinking

by

Patricia Nicole Johnson

Department of Chemistry
Duke University

Date:_____

Approved:

_____
Stephen L. Craig, Supervisor

_____
Katherine J. Franz

_____
David N. Beratan

_____
Ross A. Widenhoefer

An abstract of a dissertation submitted in partial
fulfillment of the requirements for the degree
of Doctor of Philosophy in the Department of
Chemistry in the Graduate School of
Duke University

2022

Abstract

Metallosupramolecular polymers are increasingly of interest for functional and degradable polymeric materials. In these materials, the metal-ligand bonds often bear an external mechanical load, but little is yet understood about the nature of mechanically-triggered reactions of metal-ligand bonds and how that reactivity influences the mechanical limits of the material. This dissertation presents a poly(cyclooctene) polymer bearing 2,6-bis(1′-methyl-benzimidazolyl)pyridine (Mebip) ligands on sidechains, which provides easy incorporation into polymer backbones and sidechains, binding to a large variety of metal species, and facile synthesis with sites for future study substituent effects. This platform is employed in proof-of-concept studies comparing the crosslinking behavior of iron(II) trifluoromethanesulfonate and copper(II) trifluoromethanesulfonate. It was found through small molecule spectroscopic studies that both metal species bind in the desired 2:1 MeBip:metal stoichiometry for crosslinking. When these small molecule complexes are polymerized as crosslinkers in gel and solid networks, though the extent of crosslinking is found to be similar, the copper(II)-crosslinked networks exhibited a faster relaxation than the iron(II)-crosslinked networks. Further, under high strains, the copper(II)-crosslinked networks exhibited significantly higher extensibility. This work lays the foundation for further

investigations of the effect of metal-ligand bonding on force-coupled properties of materials.

Contents

List of Tables

List of Figures

List of Schemes

List of Abbreviations

AFM	atomic force microscopy
COGEF	constrained geometry optimization
Da	Dalton
DMA	dynamic mechanical analysis
DSC	dynamic scanning calorimetry
EpoxyCOD	9-Oxabicyclo[6.1.0]non-4-ene
GPC	gel permeation chromatography
HIFU	high intensity focused ultrasound
ITC	isothermal titration calorimetry
MALS	multi-angle light scattering
MeBip	2,6-bis(1′-methyl-benzimidazolyl)pyridine
NHC	*N*-heterocyclic carbene
PMA	poly(methacrylate)
PMMA	poly(methyl methacrylate)
PTHF	poly(tetrahydrofuran)
RENT	real elastic network theory
ROMP	ring opening metathesis polymerization
SAXS	small-angle X-ray scattering
SCNPs	single-chain nanoparticles
SMFS	single-molecule force spectroscopy
Terpy	2,2';6',2''-terpyridine
Triflate	trifluoromethanesulfonate
UV	Ultraviolet
WAXS	wide-angle X-ray scattering

Acknowledgements

I would first like to acknowledge my parents, Nancy and Douglas Johnson, for their unwavering support and belief in me. I would also like to acknowledge my partner, James Cai, because I appreciate the compromises he made to support me in my graduate career and while writing this Dissertation.

I would like to acknowledge Grace Yao for her valuable experimental work and collaborative thought that helped shape these projects. I would also like to thank Dr. Tetsu Ouchi for his mentorship, training, and unending positivity in the face of experimental disaster.

I would like to acknowledge Dr. Stephen Craig, my supervisor, for his support of my exploration of difficult questions and new environments. I would also like to acknowledge Dr. Christoph Weder and Dr. Stephen Schrettl for hosting and advising me during my Fulbright tenure.

Finally, I would like to acknowledge my funding sources, the ARO through the NDSEG fellowship program, the Fulbright program, the Swiss Government Excellence Scholarship for Foreign Scholars, the Duke University Department of Chemistry, and MONET, for enabling me to pursue exciting research throughout my graduate career.

1. Introduction

All materials experience myriad forces throughout their lifetimes. In polymeric materials, that force is transduced along individual chains, and in networks it can affect stress-bearing crosslinks.[1] The chemical structure of those crosslinks is therefore integral to the material's mechanical properties.

Organometallic crosslinks in polymeric materials are attractive because of the wide variety of binding geometries and dissociation energies available in metal-ligand complexes.[2–9] How the structure of the organometallic complex structural influences the transduction of force to these crosslinks and influences the molecular response is not well understood.[6,10] Further, the connection between the molecular response and the limits of the material properties based upon these crosslinks is also poorly understood. In other words, there is a need to better understand how the molecular-level behavior of organometallic complexes under force translates to bulk material properties.

The first step towards filling this knowledge gap is to understand how force influences the chemistry of metal-ligand complexes at the molecular and linear polymer levels. The prior knowledge on this topic will be discussed in Chapter 2 of this dissertation, and suggestions for continued work in this area will be made in the conclusion of Chapter 3.

The next step is the design and synthesis of a bulk platform with modular organometallic complexes as stress-bearing crosslinks that can also be used for

molecular-level experiments. Such a platform is described in Chapter 3 of this dissertation in the context of elastomeric networks. The extension of this platform into work with gels is described in Chapter 4. This work provides the platform for bulk material observation, so the last step is to implement the described platform in single-molecule or linear polymer experiments. This last step is outside the scope of this dissertation, but its future achievement can be combined with extensions of the work presented here to correlate molecular-level force-coupled behavior and bulk properties of metallosupramolecular systems. Correlating the molecular chemistry of the crosslinks described in this work to bulk properties of the platform characterized in Chapter 3 will create molecule-to-material relationships that inform the design of next-generation metallosupramolecular polymeric materials.

2. Prior Molecular-Level Studies of Force Coupling to Metal-Ligand Dissociation

Metallosupramolecular polymeric materials are of interest for mechanically dynamic materials, optically active materials, and catalytic materials, because they incorporate properties of both organometallic complexes and organic polymer backbones.[11] The organometallic complexes provide dynamic bonding,[6] responsive changes in color,[2] and catalytic activity,[12] while the polymeric matrix offers processibility and protection from environmental degradation.[13,14] That said, there is still much to learn about the best paths for metallosupramolecular polymer design. One area of particular importance is mechanical properties, specifically how the bonding and reactivity of stress-bearing metal-ligand complexes respond to mechanical force.[15] For example, metal-ligand bonds are generally longer than carbon-carbon covalent bonds, leading to the hypothesis that they break at lower forces.[16] Knowledge of a range of metals' relative dissociation forces and reversibility would enable materials scientists to explore the influence of these parameters on the physical limits of a network, as well as to exploit the range of metal-ligand binding strengths and geometries for advanced material properties.

The first hurdle to understanding and exploiting these limits is the creation of a more complete picture of force-coupled chemistry of organometallic complexes. This is most easily done in single-molecule and solution-state experiments on linear polymers.

Therefore, this chapter reviews the current knowledge of molecular-level and solution-state force-coupling to metal-ligand bonds gained from single molecule force spectroscopy (SMFS) and ultrasonication, including an introductory section on the principles governing our understanding of how force couples to organometallic chemical reactions. The knowledge reviewed here is a starting point for understanding the change in energetics and probability of metal-ligand bond dissociation under force, which can later be paired with experiments on a modular model network crosslinked by organometallic complexes to set the stage for correlation between molecular-level and elastomeric studies.

2.1 The Relationship Between Force and the Reaction Coordinate

We begin by considering the underlying influence of mechanical force on molecular reactivity, the general principles of which apply to metal-ligand dissociation as well as covalent bonds.[17] Mechanical force is often destructive to materials, but it is simply another form of energy that can be harnessed to perform constructive chemistry.[18] Towards that aim, if we consider equation 1, we see that the change in distance Δx between the initial and terminal position of an object is proportional to the work W done to move the system from one position to the other.

$$W = F * \Delta x \qquad \text{Equation 1}$$

This relationship applies at the molecular scale as it does at the macroscale. The work W is an energy input, like light or heat, that enables a molecule to reach a transition state on a reaction coordinate. Due to the energy in the form of work provided by an applied force, less energy is required from thermal fluctuations. In other words, if $\Delta x > 0$, the force-coupled reaction coordinate has a lower activation barrier than the corresponding force-free reaction coordinate. Bell,[19] preceded by Eyring and Zurkhov, applied this idea in the context of the effect of mechanical force equilibria,[20] where the equilibrium constant K of a reaction under force can be described by equation 2:

$$\frac{d \ln K}{d F} = \frac{\Delta x}{k_B T} = \frac{x_{product} - x_{reactant}}{k_B T} \qquad \text{Equation 2}$$

where F is the force applied between two pulling points, $x_{product}$ is the average distance between pulling points of the product, and $x_{reactant}$ is the average distance between pulling points of the reactant.

The treatment can also be extended to kinetics. Using x_{TS}, the average distance between pulling points of the transition state, instead of $x_{product}$, one can find the force dependence of the rate coefficient k:

$$\frac{d \ln k}{d F} \approx \frac{\Delta x^{\ddagger}}{k_B T} = \frac{x_{TS} - x_{reactant}}{k_B T} \qquad \text{Equation 3}$$

The term $\Delta x^{\ddagger}$ is often referred to as the activation length. It is now well appreciated that force deforms the potential energy surface and all terms are therefore force-dependent, but early models of applied force on a reaction assumed the distances

$x_{product}$, $x_{reactanct}$, and x_{TS} to be constant. In that limit, there is an exponential dependence of force on the equilibrium constant and the rate coefficient, so that equations 2 and 3 can be stated as equations 4 and 5, respectively:

$$K(F) = K(0)e^{-\frac{\Delta G - F\Delta x}{k_B T}} = Ke^{\frac{F\Delta x}{k_B T}} \qquad \text{Equation 4}$$

$$k(F) = \frac{k_B T}{h} * e^{-\frac{\Delta G^{\ddagger} - F\Delta x^{\ddagger}}{k_B T}} = k_0 e^{\frac{F\Delta x^{\ddagger}}{k_B T}} \qquad \text{Equation 5}$$

As noted above, Δx and $\Delta x^{\ddagger}$ are actually functions of force, and so equations 2 through 5 are not exact. However, these equations capture the important physical underpinnings of force-coupled reactivity and are useful reference points for discussion. It should also be noted that the reaction rate depends on how well the force is coupled to the reaction pathway (given by Δx and $\Delta x^{\ddagger}$)

Because force does indeed deform molecules, the Bell model can be modified by considering the compliance (the inverse spring constant) of the stationary points. This term accounts for the force dependence of Δx and $\Delta x^{\ddagger}$, but it does assume that the compliances $\chi_{product}$, $\chi_{reactant}$, and χ_{TS} are constant. The influence of compliance is second order in F, and higher order terms can be added using a Taylor expansion to improve this description.[18]

$$K(F) = K(0)e^{\frac{F\Delta x(0)}{k_B T} + \frac{F^2 \Delta \chi}{2k_B T}} \qquad \text{Equation 6}$$

$$k(F) = k(0)e^{\frac{F\Delta x^{\ddagger}(0)}{k_B T} + \frac{F^2 \Delta \chi^{\ddagger}}{2k_B T}}$$ Equation 7

In practice, second order expansions suffice, so $\Delta x(0)$ and $\Delta x^{\ddagger}(0)$, the zero-force values of the reactant length and the activation length, respectively, along with $\Delta\chi$ and $\Delta\chi^{\ddagger}$ can be estimated using force-free electronic structure calculations.[20]

The takeaway here is that the longer Δx or $\Delta x^{\ddagger}$, the less force is required to do the same amount of work. For a given $\Delta G^{\ddagger}$, increasing $\Delta x^{\ddagger}$ correlates to a lower force at break or a lower dissociation force under dynamic loading and a higher probability of bond dissociation at constant force.[20] These underlying principles motivate study of how mechanophores including organometallic complexes respond to force, and most importantly, what factors impact $\Delta x^{\ddagger}$. It has been shown that thermodynamic stability cannot always predict mechanical stability or reactivity,[21–23] so simply referencing thermodynamic parameters of organometallic complexes is not sufficient to use them in mechanically active material design. To best understand structural effects on $\Delta x^{\ddagger}$ in organometallic complexes, we will begin at the molecular level with studies utilizing single molecule force spectroscopy (SMFS).

2.2 Single Molecule Force Spectroscopy of Metallopolymers

SMFS is the most quantitative method for determining the force at bond break and the kinetic parameters of force-coupled reactions. SMFS is often conducted as a modified method of atomic force microscopy (AFM), in which a polymer is held

vertically between a stage and the tip of the cantilever of the atomic force microscope.[18] The stage is then moved downward to stretch the polymer. The tension along the polymer chain increases with extension, and can be measured as a function of displacement of the stage. The resulting force-displacement curve is characterized by an initial region of low force that reflects the entropic unwinding of the polymer as it loses low-energy conformational degrees of freedom (Figure 1). At larger extensions, the conformational degrees of freedom start to run out, and the force begins to increase sharply as greater energy is required to distort bond angles and lengths. Finally, when the mechanical energy breaks a bond or detaches the analyte from either tip or stage, the force abruptly drops to zero and the curve ends.

The term "mechanophore" describes moieties in a polymer backbone that react chemically to mechanical force.[17] Mechanophores can be divided into two classes: scissile and nonscissile. Nonscissile means that the force-triggered reaction does not result in the breakage of the polymer backbone (Figure 1, bottom left), and that the applied force along the chain remains active even after the reaction occurs. Nonscissile mechanophores often release stored length as a result of ring opening. The force-displacement curves for polymers containing nonscissile mechanophores exhibit a characteristic plateau at the ring-opening force of the mechanophore (Figure 1, bottom right).[24] By taking the second derivative of the force-displacement curve and finding the inflection point at the plateau, one can find a characteristic f^* for that plateau.[22] The

precise value of f^* depends on the mechanophore and its reactivity, but also on a number of other factors including the length of the trapped subchain, the velocity of the stage retraction, and the number of mechanophores along the chain. Furthermore, the plateau can be characterized by fitting with the freely jointed chain (FJC) model to find the ratio L_2/L_1 where L_2 is the contour length of the polymer after mechanophore activation and L_1 is the contour length before activation. This ratio can be compared to computationally derived contour length changes.[22] SMFS has been used very productively to probe k versus F for nonscissile organic mechanophores, and a small but growing number of nonscissile metal-ligand complexes have recently been reported.[17]

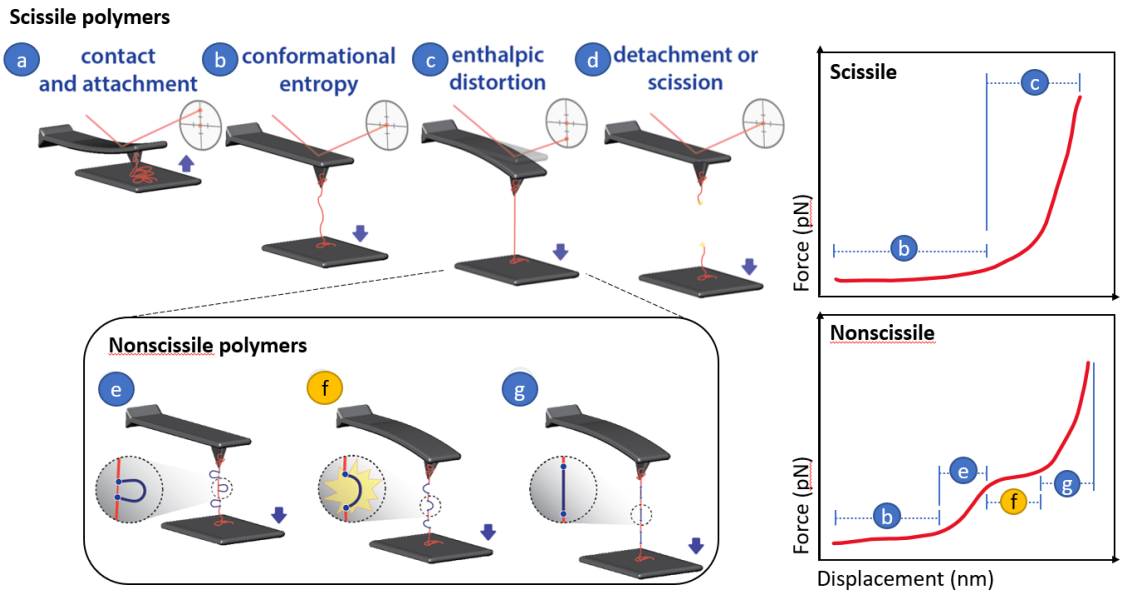

Figure 1. Diagram of Single-Molecule Force Spectroscopy. Representation of the AFM-based SMFS of scissile (top left) and nonscissile (bottom left) polymers, along with representations of the resulting force-displacement curves (right) with letters labeling the parts of the curves corresponding to the diagrams at left. Blue arrows represent direction of movement of the AFM substrate.

The subtlety of the effects that drive organometallic mechanochemistry is illustrated in an SMFS characterization of a series of ferrocenophanes (covalently bridged ferrocenes) (Figure 2, complexes 1, 2 and 3). The ring strain of the ferrocenophane does not affect the opening force as much as the conformational restriction of pulling direction on the polymer attachment sites as the reaction proceeds.[25] The distal attachment sites restrict reorientation of the pulling points, which in turn cause the ferrocenophanes to dissociate through a peeling-like mechanism, rather than a shearing-like mechanism observed in unconstrained ferrocenes. The bridged complexes' geometric restriction enables this change in mechanism to increase the rate constant of dissociation by several orders of magnitude at approximately 1 nN of force. The thermal stability of the ferrocenophanes is much higher than their mechanical stability, and this study highlights that eliminating or promoting a particular reaction pathway geometrically can make a large difference in mechanical activity. Furthermore, this study demonstrated that the effect contributes to the extent of activation observed in bulk networks, which is uncommon in the scope of SMFS studies.

Though there are several metalloenzymes that act as nonscissile mechanophores, the only other nonscissile metallomechanophore characterized using a multi-mechanophore polymer to obtain a force plateau, as in the case of the ferrocenophanes, has a very different structure from those sandwich complexes; it consists of a N-heterocyclic carbene (NHC) pincer ligand binding palladium in a square planar

geometry (Figure 2, 4).[15] The ligand was found to have a dissociation force of approximately 930 pN at a pulling rate of 300 nm·s^{-1}. This is a higher force than several organic covalent mechanophores.[17,24]

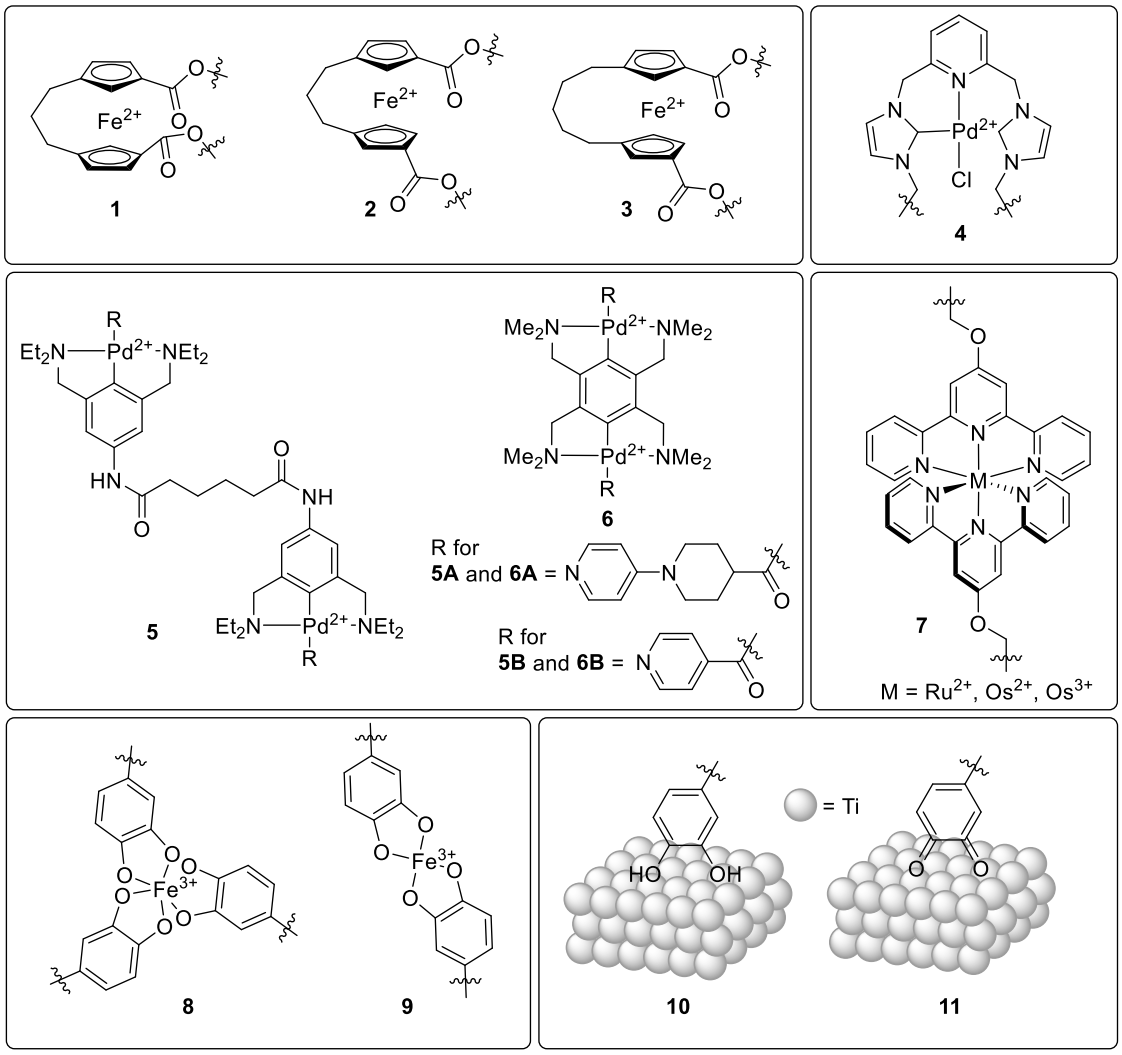

Figure 2. Metal-ligand bonds in polymers that have been characterized by SMFS: Wavy lines represent sites of polymer attachment. Counterions omitted for clarity.

Nonscissile mechanophores enable more reaction events per experiment, leading to less ambiguity surrounding the reaction versus polymer detachment from the tip or stage. However, the synthesis of multi-mechanophore nonscissile polymers is often

more complex than that of single-event, scissile mechanophore-containing polymers. SMFS of scissile mechanophores requires many repetitions of the experiment to determine the most probable force at break, often displayed in a histogram for a given loading condition. Due to the large extension of unfolding proteins and single chain nanoparticles (SCNPs), both of which are nonscissile, the histogram method is used for their characterization.

Li and coworkers[26] used single-chain nanoparticles (SCNPs) in an SMFS setup in which the polymers had catechol sidechains that bind Fe(III) metal centers. They found the dissociation force of two iron complexes, one with three catechols and one with two (8 and 9, respectively; see Figure 2). They interpreted the bimodal histogram results of SMFS experiments to mean that the bis-catechol species had a higher most probable dissociation force, with its histogram peak at approximately 200 pN compared to 100 pN for the tris-catechol species. At low iron concentrations or high pH, the system could be forced towards a unimodal histogram distribution centered at approximately 100 pN, which the authors cite as evidence that the tris-complex is favored in these conditions. Though the tris-catechol complex is thermodynamically more stable than the bis-complex, it is more mechanically labile (it has a larger $\Delta x^{\ddagger}$).

It is worth noting a few other studies on the dissociation of metal-ligand bonds in a different context, and one such study also concerns catechol-metal binding. Messersmith and coworkers[27] used a titanium surface as the substrate for SMFS and

attached a catechol-terminated chain to the cantilever tip of the atomic force microscope (AFM) (10**,** Figure 2). Upon retraction of the substrate from the tip, a mean force value of 805 ± 131 pN was observed, which was attributed to the dissociation of the catechol from titanium. The SCNP study included modeling of the binding of oxidized catechols to iron(III) and determined that it was thermodynamically unfavorable, explaining why a second, lower bimodal force distribution was not observed in their histograms.[26] However, Messersmith and coworkers[27] did report a bimodal low-force distribution that was attributed to oxidized catechols at an elevated pH of 9.7, with a mean force 80 ± 60 pN for the low-force regime and 740 ± 110 pN for the high-force regime. The high-force regime distribution was attributed to unoxidized catechol binding, while the low-force regime distribution was attributed to oxidized catechol binding (11**,** Figure 2). If this data indicates that the oxidized catechols are binding to titanium, then it also indicates that their binding to titanium is more thermodynamically favorable than their binding to Fe(III).

SMFS studies on metalloproteins can also shed some light on the subject of metal-ligand bond mechanical strength. Histidine binding to metals in proteins is common, so Schmitt, et al.[28] designed a system in which the cantilever tip was functionalized with chelating *N*-nitrilo-triacetic acid moiety and, once metalated with one of a variety of metals, the tip was brought into contact with a histidine-functionalized substrate. The retraction of the substrate was then used to determine the

rupture force of the histidine-metal bond. It was assumed that rupture would occur between the histidine and metal, rather than the *N*-nitrilo-triacetic acid and metal, because the triacetic acid has three stable bonds to the metal compared to the single, labile histidine association. The copper(II) bond to histidine has the strongest binding force at 58 ± 5 pN, followed by nickel(II) at 38 ± 4 pN, then zinc(II) at 28 ± 3 pN, then cobalt(II) at 22 ± 4 pN.

Cao, et al. reported that the presence of Ni(II)-histidine bonding causes a histidine-modified small protein GB1 to unfold at a higher force (243 pN, 198 pN, and 219 pN for three GB1 derivatives) than the metal-free modified protein (119 pN, 120 pN, and 160 pN for the same respective derivatives).[29] Additionally, the more directly the histidine-nickel(II) bond was centered within the force-bearing region of the amino acid sequence, the larger the mechanical stabilization of the protein.

Thiolate bonds to metal centers within proteins were also studied by SMFS due to their biological ubiquity. Zheng and Li found that two of four of the thiolate bonds to zinc(II) in protein rubredoxin rupture at an average force of 172 ± 58 pN.[30] The unfolding length of each rupture event matched well to Monte Carlo simulations of the unfolded protein length, so it can be concluded that the two bonds either rupture simultaneously or in such quick succession that it is observed as a single dissociation event by SMFS. In another report by the same authors, the rupture of two Fe(III)-thiolate bonds in rubredoxin displayed a broad force distribution with most probable dissociation force of

211 ± 86 pN.[31] The two bonds that rupture in rubredoxin have been shown to have two different Fe(III)-S bond lengths, so by creating mutated versions of the protein in which each cysteine in turn was replaced by a histidine (which has weaker metal coordination), the researchers determined that the shorter of the bonds ruptured at an average force of 203 ± 92 pN, while the longer ruptured at an average force of 121 ± 74 pN. The difference between these bond lengths is small, only 0.06 angstroms. Using an analogue of the protein with a higher covalency, this report further postulated that the rupture force of the iron(III)-thiolate bonds was governed by their covalent character, as the rupture force decreased with decreasing covalency from 258 ± 122 pN to 211 ± 86 pN. The difference is small, so additional study is needed to draw strong conclusions. Additionally, as seen for osmium previously,[32] the oxidation state does matter; the reduced version of the same protein analogue with iron(II) displayed an average rupture force of only 152 ± 62 pN. This aspect is further explored in a study of a mutant GB1 binding cobalt(II)/(III), which demonstrated that oxidation of the cobalt center caused its average force at rupture from histidine moieties to increase from 140 ± 45 pN to 260 ± 55 pN.[33] Further study of the iron(III)-rubredoxin system revealed that it exhibits significant mechanical anisotropy and that the iron center is released by a stochastic mechanism.[34,35]

The discussed protein-based studies highlight the difficulties of parsing out information about the intrinsic behavior of isolated metal-ligand bonds (as would be relevant to many coordination polymers) based on their behavior in proteins. The

complexities of force vectors can be difficult to unravel in the case of unfolding proteins, because protein secondary structure transduces force differently than a linear polymer.[36–38] Still, these studies give a clue to the force regime that can be expected for similar metal-ligand bonds, approximately 20 to 300 pN.

In linear polymers, the histogram method was used to characterize terpyridine complexes of ruthenium(II),[39] osmium(II), and osmium(III) (Figure 2, complex 7).[32] The Os(II) complex was found to have a most probable dissociation force of 80 ± 30 pN, while the Ru(II) complex was found to have a most probable dissociation force of 95 pN,[39] which falls into the error range of the osmium data.

The osmium(III) analog of **7** has a higher dissociation force than that of either the osmium(II) or ruthenium(II) analogs; the average dissociation force for the osmium(III) analog of **7** is 130 ± 60 pN. These findings demonstrated that the oxidation state of the metal species affects the dissociation force, which the authors tentatively attribute to an increase in sigma bonding to the ligand for osmium(III) compared to osmium(II), relocation of the electronic charge distribution to the metal center from the complex periphery in the osmium(III) state, and higher ligand field stabilization energy (LFSE) for osmium(III) compared to osmium(II).[32]

Kersey, et. al characterized the influence of a different aspect of molecular structure using scissile mechanophores: the ligand. The displacement of two pyridine-based ligands from square planar palladium(II) complexes was characterized at different

loading rates, which illustrated that force-dependent reaction kinetics scale with force-free reaction kinetics. Additionally, since $\Delta x^{\ddagger}$, the difference in length between the ground state and the transition state, is also very similar for the two force-coupled reactions, the force dependency is the same regardless of the difference in kinetic parameters. The data also enables extrapolation of force-free thermal off-rates of 1.4 s^{-1} for 5A and 40 s^{-1} for 5B, in excellent agreement to values of 0.7 ± 0.4 and 20 ± 3 s^{-1}, respectively, measured by dynamic ^{1}H NMR spectroscopy as the force-free dissociation rate constants. This study was the first to compare the mechanically-influenced kinetics of a reaction to the force-free kinetics and the first to connect mechanism and quantitative force dependence. In a later study, Kersey, et. al investigated complex 6A using a pincer ligand that had methyl groups on the amine coordination sites where 5A had ethyl groups.[8] Complex 6A is kinetically more labile than 5A due to the increased steric bulk of the ethyl groups, and it also ruptured at a lower average force of 92 pN compared to 164 pN for 5 (30 nN·s^{-1} loading rate).

All the SMFS studies discussed teach us about select organometallic systems, and they also point out that the diversity of metal-ligand bonding means that very simple, overarching mechanical reactivity rules (for example, that oxidation increases force at break) that apply to all metallomechanophores are likely to be forthcoming with systematic study.

2.3 Ultrasonication of Metallopolymers

Pulsed ultrasound, also called sonication, is an alternative method to SMFS used to apply force to mechanophores in linear polymers in solution (including in gels).[18] Though less quantitative than SMFS, sonication can be applied more easily to a variety of polymer backbones and mechanochemically active monomers.[17] Sonicated solutions give rise to cavitation events, which are essentially bubbles that grow and contract in size until unstable, at which point they collapse inwards on themselves. The collapse causes the surrounding solution to flow into the void left by the cavitation bubble. This elongational flow applies tension to polymers that are in the solution[18] and reaches high enough forces to break relatively strong carbon-carbon single bonds.[40] Weak bonds in mechanophores will preferentially break under sonication conditions, so both scissile and nonscissile mechanophores can easily be investigated by sonication if their activation produces an observable change to track alongside molecular weight, such as a spectroscopic signature.

Several groups have employed sonication in the investigation of metallosupramolecular polymers. Sonication of palladium(II) metallopolymer 12 led to the mechanical scission of the built-in weak bond between palladium(II) and the diphenylphosphine-terminated telechelic poly(tetrahydrofuran). The metal-ligand bond reforms upon removal of force,[41] and a follow-up study quantified the extent of scission through the use of dicyclohexylphosphine-terminated poly(tetrahydrofuran) 13 and

diphenylphosphine-containing stopper complexes to create heterocomplexes at scission sites.[42]

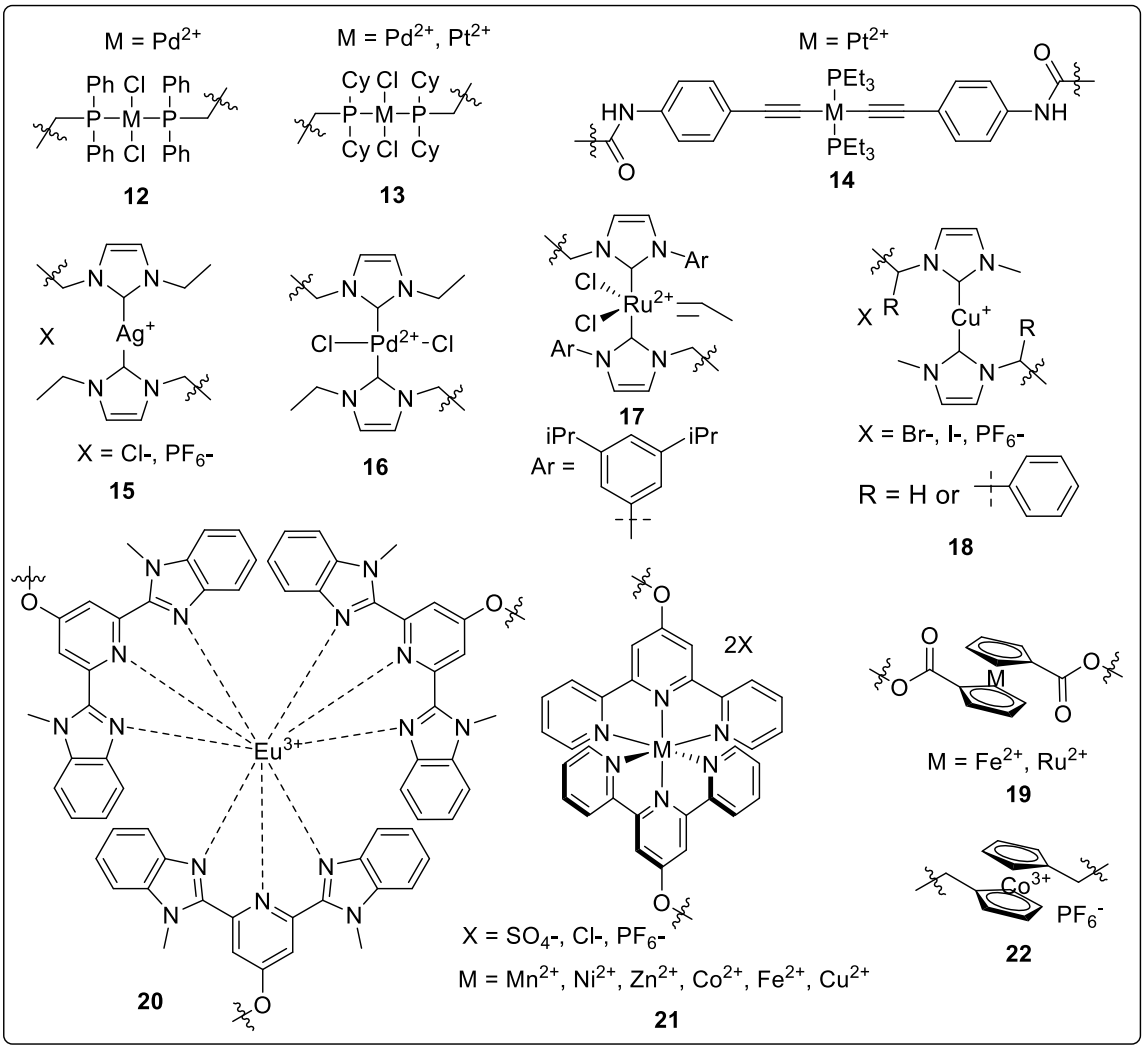

Figure 3. Organometallic complexes the dissociation of which has been investigated by pulsed ultrasound. Some counterions omitted for clarity.

Almost half of the polymeric homocomplexes were converted to heterocomplexes after 8 hours of sonication, indicating the effective scission of the metal-ligand bond by sonication.[42] The authors note that scavenging is not guaranteed to be quantitative even with excess stopper complex, so the observed results represent the

lower limit of chain scission occurring due to complex dissociation. In these experiments, it is assumed that rate of heterocomplex formation can be used as a proxy for rate of chain scission because the heterocomplex forms quickly compared to the rate of homocomplex reformation (corresponding to chain reformation).

It was further demonstrated that palladium complexes in 13 break at a higher rate than platinum complexes, as expected due to the greater thermal and kinetic stability of platinum complexes compared to analogous palladium complexes.[43] 63% of the palladium centers ruptured compared to 53% of the platinum centers in the same five hour sonication period. However, it is noted that the difference in mechanical stability between platinum and palladium complexes of this type is several orders of magnitude smaller than the difference in thermal stability. This discrepancy can be attributed to the collapse of the cavitation bubble acting as a rate limiting step.[44]

Platinum(II) and palladium(II) have also been used in a mechanochemical context with other types of ligands, namely N-heterocyclic carbenes (NHCs) and acetylides. As expected, polymers containing palladium(II)-NHC complexes (Figure 3, 16) preferentially break at the complex site, as is true for the polymers containing phosphine ligands.[16] It was demonstrated that, as is the case for covalent mechanophores, the rate of scission is increased for polymers of higher molecular weight.

Platinum(II)-acetylide complexes (14**,** Figure 3) are also the site of preferential scission under sonication,[45] and the rate constant increased with molecular weight. The reaction displayed first-order kinetics with respect to the metal complex. In control experiments sonicating 70 kDa poly(methyl acrylate) (PMA), little-to-no chain scission was observed. Though it is expected that the scission rate of covalent carbon-carbon bonds should be much lower than that of metal-ligand bonds, the extreme conditions at cavitation sites promotes at least some homolytic cleavage of even strong covalent bonds under the reported experimental conditions. This data indicates the need for repeated control experiments to demonstrate the relative weakness of the metal-ligand bond compared to a common covalent polymer backbone (PMA).

Several NHC complexes similar to 16 have also been studied using sonication. Sijbesma, et al. functionalized a Grubbs-type ruthenium catalyst with polymers (17, Figure 3).[46] Approximately 50% of the complex 17 in a 36 kDa polymer degrades to an catalytically inactive complex in 120 minutes of sonication. The ruthenium-NHC complex was further optimized as a catalyst in a later study.[12] In studies that indicate that the metals with an oxidation state of one are weaker than those with an oxidation state of two, other NHC complexes have been studies: the silver(I) complex 15 and the copper(I) complex 18. These complexes have polymer attachment points like those in 16 and 17. Whereas 16 and 17 were sonicated in toluene, 15 was sonicated in both toluene and acetonitrile. For a 13.4 kDa polymer in toluene with a hexafluorophosphate

counterion, 88% of 15 was converted to a polymeric imidazolium salt (indicating scission of the silver-ligand bond) in 10 minutes of sonication.[47] Given scission reached such a high ratio in spite of the polymer's small size and the short sonication time, it can be surmised that 15 is significantly easier to dissociate than 17. The more polar solvent acetonitrile was used to suppress halide-bridged dimerization when Cl^- was present. In an analogous 10 minute sonication experiment, this 13.4 kDa polymer of 15 degraded quantitatively to produce an imidazolium salt from the NHC complex. The authors suggest that the increased conversion of this polymer compared to that with the hexafluorophosphate counterion is due to a shift in the equilibrium to a slightly higher population of a monoligated silver(I) complex and free carbene. In a later study on the same type of complexes, it was found through constrained geometry optimization (COGEF) calculations that the dissociation force at the preferential silver(I)-NHC site is between 400 and 500 pN.[48] The facile scission of the silver(I)-carbene bond was used to enable sonication-induced catalysis in additional studies.[46,49]

Michael and Binder reported copper(I) complex 18 (Figure 3) as a latent, mechanically activated "click" catalyst.[50] Though the structure is similar to that of 15, sonication conditions were not. First, a solvent mixture of 30:1 THF:MeOH was used rather than toluene. Solvent does matter,[44] as noted in the supporting information of this study; the conversion of the substrate decreased from 10% in the aforementioned solvent mixture to only 2% in pure THF. Second, the sonicator amplitude was set to 30%, rather

than the more conventional 20% used in the other studies cited here. In any case, the highest conversion reached was 44% by the complex 18 functionalized with two polystyrene polymers to reach a molecular weight of 13.1 kDa. When **18** is functionalized with two poly(isobutane) polymers instead of two polystyrene polymers, it only reached a conversion of 27% in spite of a higher molecular weight, indicating that the steric bulk of a neighboring styrene may aid in the force-coupled dissociation of a ligand to activate the catalyst. Further optimization of the catalyst was reported in a later study.[51,52]

Multiple research groups have investigated the sono-mechanochemistry of metallocenes. Ferrocene is of particular interest because it is thermodynamically very stable. The utility of the cleavage of metal-organic bonds outside catalysis is highlighted in metallocenes by Di Giannantonio, et. al, who used the cleaved ferrocene units to enable oxidation and release of the iron ion.[53] Sha, et. al found that ferrocene is actually mechanically weak.[23] Through computational work for ferrocene, it was found that the nonscissile complex 19 ruptured through a different mechanism than the ferrocenophanes characterized by SMFS. It broke through a "shearing" type displacement of the two cyclopentadienyl groups, rather than a "peeling" type displacement found to varying degrees in ferrocenophanes. It was found through monitoring of a copolymerized internal standard that scission of ruthenocene is more difficult than that of ferrocene. Zhang, et al. showed that metallocene cleavage could be

used for network remodeling,[25] but it could also have future applications in drug delivery or catalytic materials.

The ruthenium(II) analog to ferrocene (ruthenocene) which is even more inert thermodynamically, is also weak mechanically, though stronger than ferrocene.[7] Another complex with the same valence electron number, cobaltocenium (with a hexafluorophosphate counterion) (Figure 3, 22) has been incorporated into a polymer backbone and dissociated by sonication.[54] Though cobaltocenium is isoelectronic to ferrocene, it was not stable with the electron-withdrawing ester polymer attachment groups used for ferrocene and required alkyl attachments for polymer incorporation. As observed for ferrocene and ruthenocene, despite the large thermal dissociation energy for cobaltocenium, it was the preferential scission site during sonication. This behavior indicates that cobaltocenium is mechanically weak compared to carbon-carbon bonds in the backbone, as with ferrocene, ferrocenophanes, and ruthenocene. Contrary to the neutral ferrocene and ruthenocene complexes, which dissociate in a "shearing" mechanism,[7,23] the cationic cobaltocenium was found by COGEF to have a combination "peeling" and "shearing" dissociation mechanism. "Peeling" is observed for geometrically constrained ferrocenophanes,[25] but in this case it is suggested that the association of the counterion in the transition state promotes this alternate mechanism.[54]

Finally, as with SMFS studies, terpyridine complexes were studied in the context of ultrasonication. Unfortunately, the dissociation of the same metal species investigated

with terpyridine by SMFS has not been studied by ultrasonication. Both available reports on sonication of terpyridine-functionalized polymers focus on first-row transition metals.[55,56] In 2014, polymer micelles were reported in which complex 21 with copper(II) centered in diblock copolymers, but high intensity focused ultrasound (HIFU) was used rather than a probe sonicator immersed in the reaction solution. Cargo release from the micelles containing the copper(II)-terpyridine bond (Figure 3, 21) as the designated weak bond is more efficient than the same system containing disulfide bonds as the weak bond.[55] Furthermore, replacing copper(II) with ruthenium(II) prevented micelle cargo release, leading to the conclusion that the ruthenium(II)-terpyridine bond is stronger than the copper(II)-terpyridine bond.

More conventional probe sonication was used to characterize a series of other transition metals in polymer-functionalized terpyridine complexes.[56] Metal complex scission was monitored by metal-mediated quenching of a fluorescent probe, and increased quenching indicated scission of the metal complex. The difference in quenching of nonsonicated versus sonicated solutions is greatest for cobalt (12%). The other complexes all exhibit increased quenching under sonication, but the extent of quenching increase is at most half of that observed for the cobalt(II) complexes. Interpretation is complicated by the fact that the nonsonicated solution data indicate that the polymer backbone has some effect on the stability of the complexes. For example, sonication of the same terpyridine complexes with a poly(tetrahydrofuran) (PTHF)

backbone results in a large 15% increase in quenching by nickel(II) complexes where there had only been a 5% increase with the original poly(methyl methacrylate) (PMMA) backbone. Conversely, sonicated cobalt(II) complexes exhibit significant quenching with the PMMA backbone, but no change in quenching for the analogous PTHF complexes. Zinc(II) complexes with the PTHF backbone also demonstrate no change in quenching under sonication, as compared to 4% quenching with the PMMA backbone. The authors cite these unexpected results as an indication that more study is needed on the stabilization of complexes by the backbone and on the kinetic contribution to the dissociation of these complexes.

Work by Balkenende, et al., indicates that europium(III)-MeBip bonds (20, Figure 3) in a polymer are broken by sonication and reform after force is removed.[2] The mechanically dissociated ligand could be intercepted by iron(II) ions, which do not displace europium(III) without sonication. The more strongly coordinating ligand dipicolinate was not dissociated from europium(III) by sonication under the same conditions.

Overall, ultrasonication studies reinforce some conclusions of SMFS studies. For the most part, the experimental conditions within these studies are similar; toluene is the preferred solvent, argon or nitrogen the preferred atmosphere, and 20% sonicator fluctuation amplitude is the most commonly used. This is an excellent start towards

creating a body of knowledge that can be used for design parameters for organometallic mechanophores.

2.3 Conclusion

Between sonication and SMFS, there is the beginning of a body of knowledge of how the bonding and reactivity of stress-bearing metal-ligand complexes respond to mechanical force. Still, there is more to learn concerning how organometallic complex structure affects $\Delta G^{\ddagger}$ and $\Delta x^{\ddagger}$, and it is difficult to discern trends through the few reported systems because they use diverse metal species and ligands. Furthermore, the studies that include SMFS or sonication often do not include in their scope correlation to bulk networks either in gels or solid elastomers. There are a few examples that do, particularly the extension of the SMFS system by Kersey, et al.[8,57] to behavior in gels.[8,58,59] The studies on ferrocenophanes[25] and europium(III)-MeBip complexes also include some bulk-level testing.[2] This still leaves a serious gap in the understanding of molecular-level force coupling to metal-ligand bonds and its relationship to macroscopic mechanical properties.

It is clear from the reviewed SMFS and sonication studies that there are several important factors to study in the future. The oxidation state, atomic radius, binding geometry, and electronic and steric effects of ligands are all worthy of consideration with respect to how they affect $\Delta G^{\ddagger}$ and $\Delta x^{\ddagger}$ and thereby mechanical reactivity. Furthermore, the surrounding environment beyond the ligand sphere can also affect the

force coupling to a metal center, such as a protein's folded structure, counterion choice (through stabilization of the transition state), or weakly associating solvent molecules.

Sonication data or SMFS characterization could be used to more systematically probe the effects of these factors with the development a system that binds to a wide range of metals with different binding geometries and oxidation states and that could easily be synthetically modified to investigate electronic and steric effects on the coordination sphere. Additionally, such a system should be able to be incorporated into bulk networks in order to correlate the trends observed at the molecular level to bulk material properties.

3. A Model Elastomer with Variable Metal-Ligand Crosslinking

3.1 Introduction

Metal-ligand bonding plays an increasingly important role in a range of polymer network studies and applications. Because metal-ligand bonds often act as stress-bearing moieties in these networks,[60] the relationship between the mechanics of the metal-ligand complex and those of the polymeric material are of great interest. In particular, Chapter 2 showed that metal-ligand bonds are often the sites of preferential scission in organic polymers. This fact raises questions concerning the effects of the metal identity and oxidation state, as well as ligand sphere sterics and electronics, on the behavior of metallopolymeric elastomers under mechanical force. One issue, discussed in Chapter 2 of this dissertation, is that the molecular-level behavior of metal-ligand bonds under force is not yet well-characterized. Furthermore, translation of work between the single-molecule and linear polymer level and the network level is made difficult by aggregation and microphase separation of the complexes from the polymer backbone in bulk elastomers, which alters force transduction through the material.It is therefore highly desirable to employ a modular metal-ligand platform the mechanics of which are characterized at the single molecule level and the influence of which on the macroscopic mechanics of networks can be measured.

To date, the closest such platform is that of Kersey and coworkers,[8] which has been studied in gels. Ferrocenophanes have been studied with SMFS and shown to be

active in the solid state,[25] but their structure cannot easily be extended to a wide variety of metal species. A MeBip-functionalized polymer, analogs of which have been studied in gels and solid elastomers,[11,13,14,61] was sonicated and incorporated into a solid to demonstrate mechanical activity, but its mechanical properties with the metals that were sonicated were not thoroughly characterized in the solid state.[2] Furthermore, MeBip-based materials are known to be prone to aggregation and microphase separation,[11,62] which complicates the pursuit of direct molecule-to-material relationships.

We therefore sought to develop a platform that would be amenable to such studies. In particular, we targeted homogenous elastomers because they would not be complicated by solution-state kinetics present in gels and because they are tractable in a wider range of applications than gels (especially if solvent evaporation is an issue). We were mindful of criteria that would impact the utility of such a platform, including: (i) the extent of aggregation and microphase separation in the solid state; (ii) ability to bind a variety of metal species; and, (iii) ability to be characterized by SMFS or sonication studies.

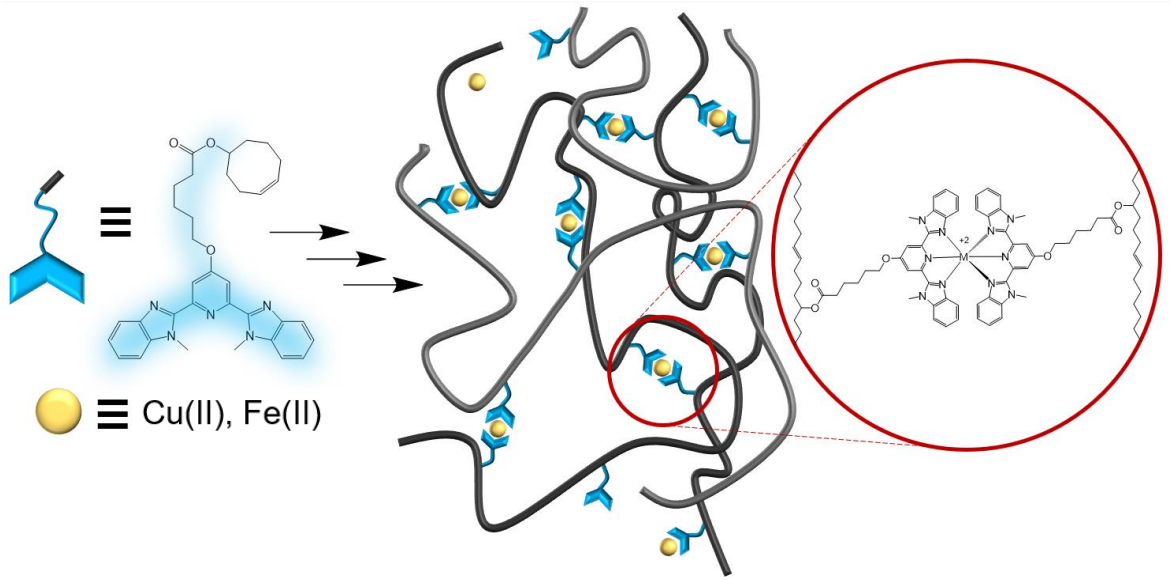

Figure 4. Overview diagram of the system used in this work. Schematic representation of the ligand (blue) as a small molecule and as a metal-chelating crosslinker in a polymeric network. Triflate counterions are omitted for clarity.

Based on previous reports of its use in polymeric systems,[2,62,63] the ligand 2,6-bis(1′-methyl-benzimidazolyl)pyridine, 1A, was chosen as the basis of our platform (Scheme 1). This ligand binds with a variety of transition metals and lanthanides, including cadmium,[64] chromium,[65] manganese,[66] iron,[2] cobalt,[13,67,68] nickel,[68] copper,[67] zinc,[13,67] ruthenium,[69] osmium,[70] platinum,[71] lanthanum,[13,72] and europium.[2,13,73] This versatility will make future extensions of this work facile. Additionally, a range of polymers can be easily functionalized with the ligand[2,13,62] through a synthetically accessible hydroxyl functionality (Scheme 1, bottom). Finally, the simple synthetic route to this type of ligand allows for several sites of substitution that set the stage for later

exploration of the effects of ligand electronic and steric effects on metal-ligand binding in material contexts (Scheme 1, bottom).

MeBip-functionalized polymers, however, tend to exhibit aggregation or microphase separation of the metal-ligand complexes.[62,74] It is therefore difficult to determine whether material property differences are due to the metal-ligand interaction or to large-scale topological features. In bulk materials reported to date, the MeBip ligand moieties form large aggregates or even crystallize, even when chelating a metal ion. This affects the material properties because it leads to hard ligand phases and soft polymer backbone phases which have different material properties.[1,74] We sought to identify a system in which metal-ligand bonds created crosslinks within a network without the complexes causing large aggregates or microphase separation.

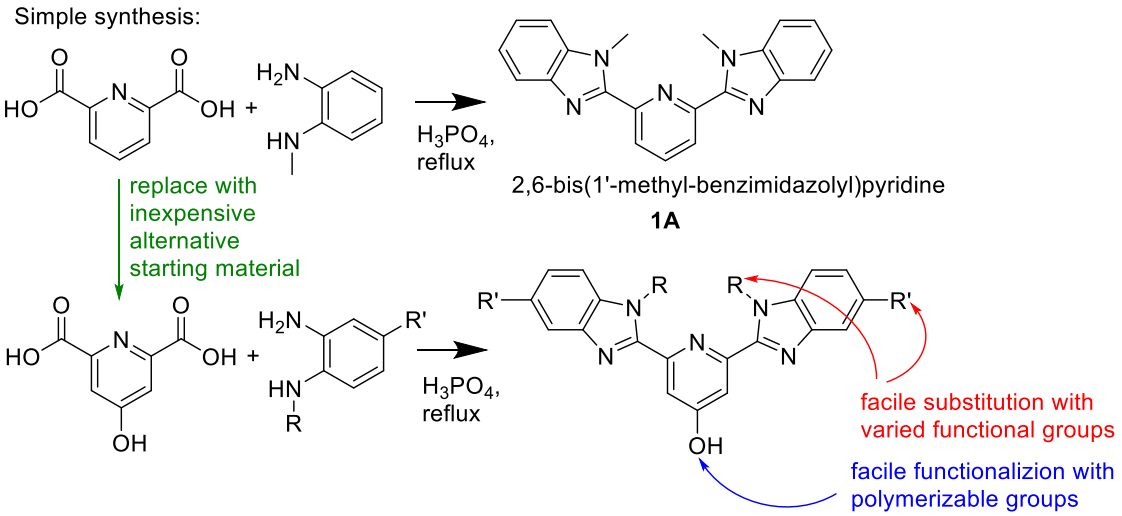

Scheme 1: Simple and versatile synthetic route to basic 2,6-bis(1′-methyl-benzimidazolyl)pyridine and polymerizable derivatives.

In this work, we use the 2,6-bis(1′-methyl-benzimidazolyl)pyridine (MeBip) ligand in a proof-of-concept study to elucidate differences in material properties based solely on the coordinating metal (Figure 4). A MeBip derivative was functionalized with cyclooctene to make it amenable to ring-opening metathesis polymerization (ROMP). This monomer was used first as a small molecule chelator in studies of solution-state binding. ROMP polymers incorporating the functionalized ligand were then synthesized and used to investigate the properties of elastomeric films crosslinked by organometallic complexes comprising two equivalents of the ligand. To determine whether the metal identity does indeed affect network properties, films crosslinked by Fe(II) trifluoromethanesulfonate or Cu(II) trifluoromethanesulfonate were characterized with respect to their homogeneity and their behavior under mechanical force.

3.2 Small Molecule Stoichiometry Studies

We began by characterizing the stoichiometry of small molecule model complexes, because the coordination number determines the network functionality, which in turn affects overall material properties.[60] As in previous reports,[74,75] UV-visible spectroscopy was used to investigate the binding stoichiometry of the chosen ligand, 3, with Fe(II) and Cu(II) trifluoromethanesulfonate (triflate) salts. Compound 3 is the monomer used in subsequent ring-opening metathesis polymerization (ROMP) and so provides a close analog of the ligand environment in the bulk materials studied in this

work. The ligand 3 was synthesized in three steps from commercially available materials (Scheme 2).

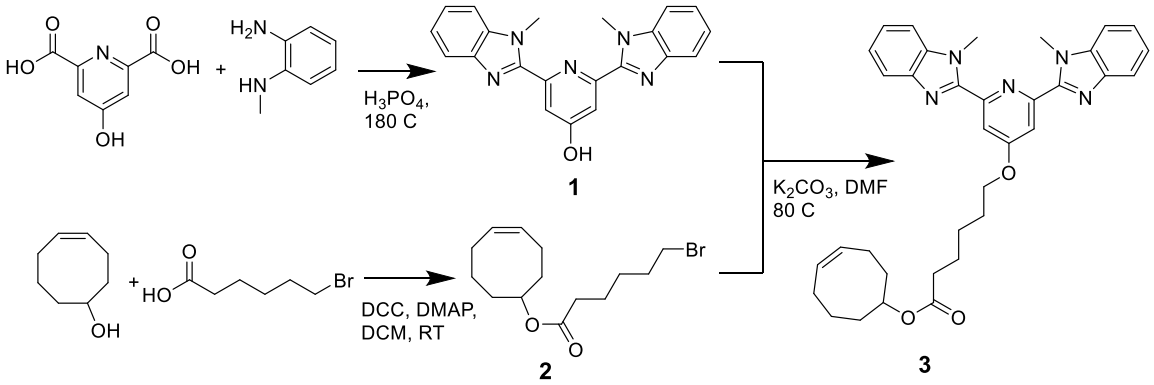

Scheme 2. Synthesis of ligand, compound 3.

A solution of the selected metal salt was titrated with a solution of 3 to verify the desired 1:2 binding stoichiometry. If 1:1 binding dominates, the metal centers would simply terminate sidechains along the polymer backbone rather than form a crosslink between two backbones.

3.2.1 Results and Discussion of Stoichiometry Studies

For both metals, a peak centered near 340 nm was monitored and attributed to the $\pi \rightarrow \pi^*$ transition of the bound ligand 3**.** When unbound to a metal center, this transition is marked by absorbance below 300 nm, and the 340 nm band increases as more ligand is added to the metal solution. The redshift of the $\pi \rightarrow \pi^*$ transition of the ligand is attributed to increased planarity upon binding and thereby better delocalization of electrons through the ligand π system.[62] As can be seen in the crystal

structure of the free MeBip ligand,[76] the imidazole groups are not fully in plane with the central pyridine (Figure 5).

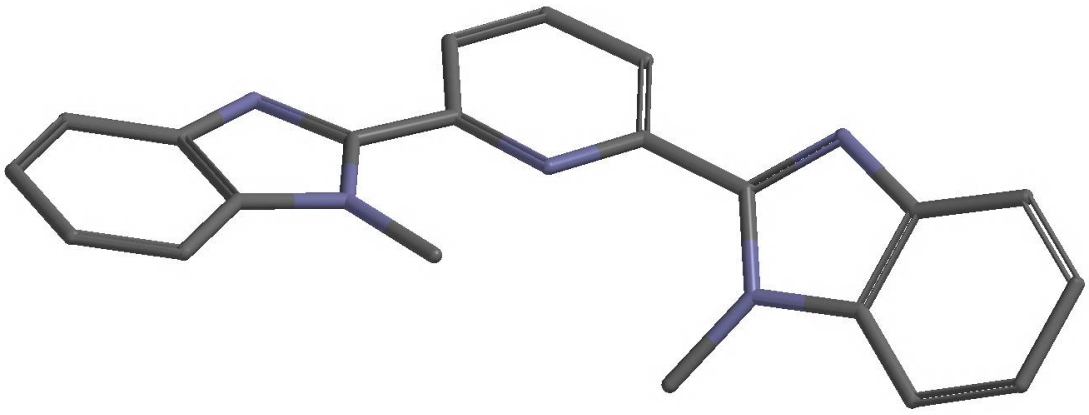

Figure 5. Crystal structure of free ligand MeBip, also named (2,6-bis(1′-methyl-benzimidazolyl)pyridine), ID QIFPOK[76] from the Cambridge Structural Database.

The absorbance of the UV peak near 340 nm was plotted against the molar ratio of the metal species to 3. The titration was continued past the expected binding ratio of 2:1 **3**:metal to determine whether the complex formed in solution maintained its 2:1 binding stoichiometry or was disrupted by the addition of excess metal. Examples of spectra throughout the metal salt titrations of a solution of 3 can be seen in Figures 7 and 8, while the metal salt solution spectra without ligand are in Figure 9.

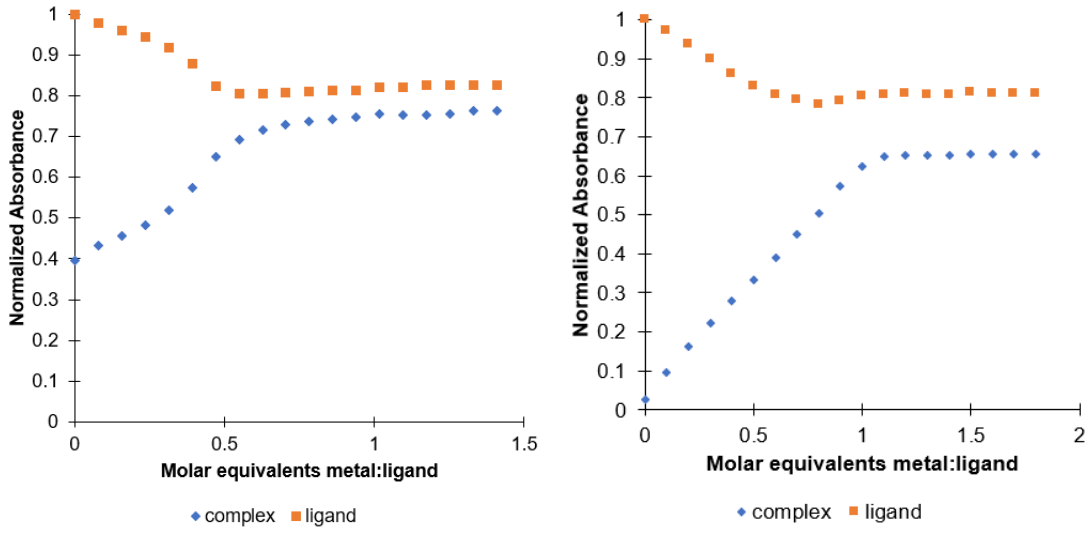

Figure 6: Plots of normalized absorbance versus molar equivalents metal:ligand. Left: The absorbance at 318 nm (orange) and 338 nm (blue) of 3 titrated with iron(II) tiflate. Right: The absorbance at 318 nm (orange) and 348 nm (blue) of 3 titrated with copper(II) triflate.

Titrations were conducted starting with a 1.14 μM solution of 3 and adding aliquots of a solution of Cu(II) triflate or Fe(II) triflate. This titration was conducted to at low concentrations to accurately monitor the highly absorptive 318 nm ligand absorption peak as it decreased due to metal binding. Example spectra of the ligand 3 being titrated with Fe(II) triflate or Cu(II) triflate can be seen in figures 7 and 8, respectively.

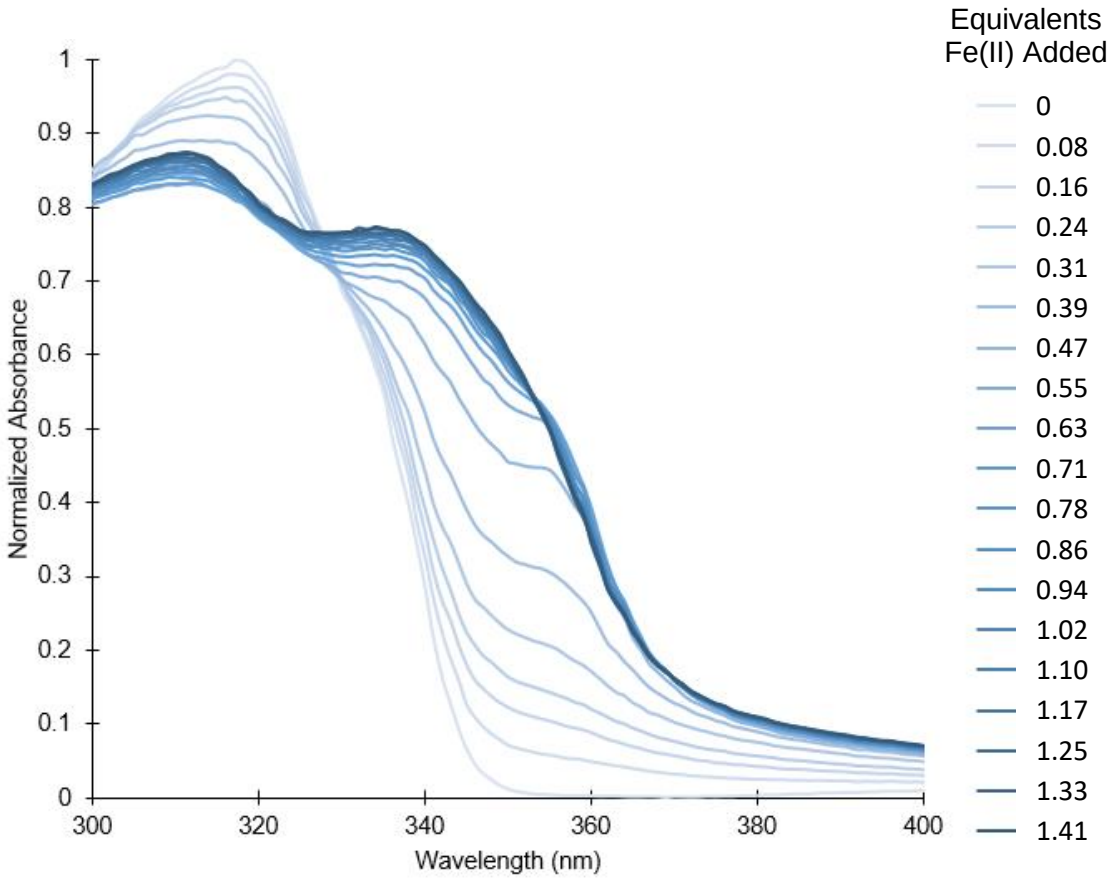

Figure 7. Representative spectra obtained during titration of 3 with Fe(II) triflate in 95:5 toluene:methanol. Initial [3] = 1.14 μM.

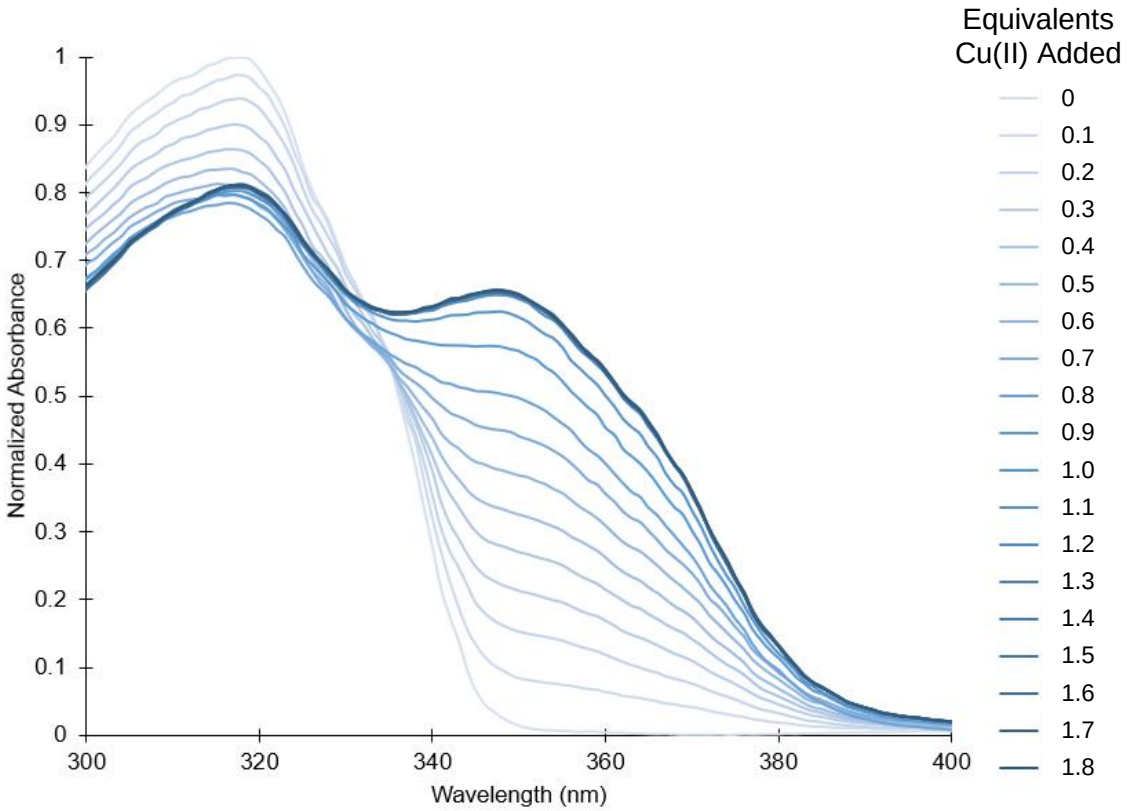

Figure 8. Representative spectra obtained during titration of 3 with Cu(II) triflate in 95:5 toluene:methanol. Initial [3] = 1.14 μM.

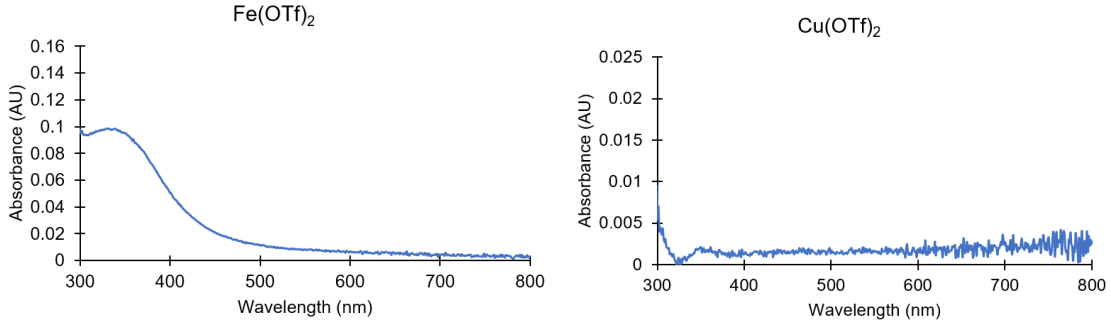

Figure 9. Spectra of metal salts. UV-Visible absorbance spectra of solutions of iron(II) triflate (left) and copper(II) triflate (right) in 95:5 toluene:methanol.

For Fe(II):3 binding, the $\pi \rightarrow \pi^*$ transition is centered at 338 nm, and this is the wavelength monitored throughout titration. Fe(II):3 binding was dominated by 1:2

binding as indicated by the cessation in absorbance increase of the $\pi \rightarrow \pi^*$ transition peak at 338 nm past the addition of 0.5 equivalents of Fe(II) triflate. This was previously shown to be the case in other solvents.[74] Our experiments confirm that the expected 1:2 Fe(II):3 binding holds in toluene (Figure 9, left).

For Cu(II), the $\pi \rightarrow \pi^*$ transition peak centered at 348 nm was monitored. The increase in the absorbance of this band was steady up to the addition of one equivalent of metal salt (Figure 9, right). We attribute the prominent increase of the 348 nm band between 0 and 1 added equivalents of metal salt to stronger 1:1 binding with Cu(II) ions than the subsequent second ligand binding. This hypothesis is supported by examination of the absorbance versus molar ratio curve for the 318 nm ligand absorption peak. Below 0.5 equivalents metal salt added, there is a steady decrease in absorbance as would be expected for two ligands binding to each metal. However, after 0.5 equivalents metal salt added, there are two inflection points. The first inflection point can be attributed to the dissociation of some of the ligand from the initially formed 2:1 ligand:metal complexes, the second inflection point at 1 equivalent ligand:metal can be attributed to the complete formation of 1:1 ligand:metal complexes, similar to the inflection point in the absorbance of the 348 nm peak.

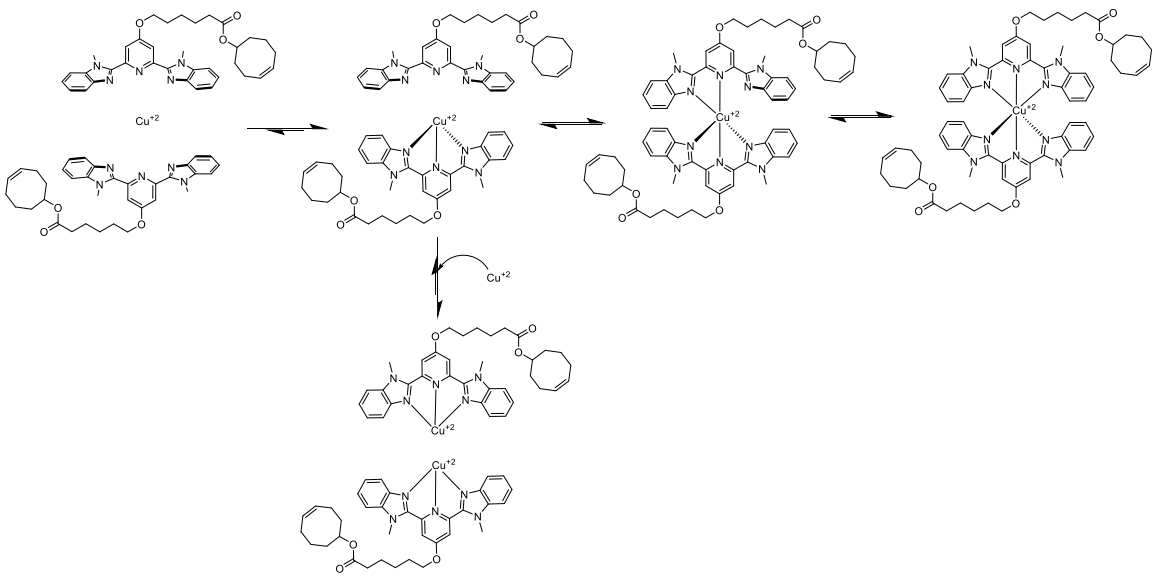

Scheme 3. Suggested association scheme of the first and second ligand equivalents to copper(II). While the first ligand is strongly bound, the second ligand can readily dissociate. Therefore, when there is excess Cu(II) present, two 1:1 complexes form quickly. Triflate counterions omitted for clarity.

Upon binding to Cu(II), the two imidazoles and the pyridine are forced into a planar orientation with the pyridine, as can be seen in the crystal structure POHXUI[77] (Figure 10, left). This also occurs with the first ligand binding to iron(II), as can be seen in the crystal structure VAPVIT[78] (Figure 10, right). For this reason, both metals induce a similar red-shift of the $\pi \rightarrow \pi^*$ transition at the first ligand binding event. Since the second ligand bound to iron(II) is also forced into a planar orientation, the new $\pi \rightarrow \pi^*$ transition peak increases upon the second ligand binding event to the same extent that it did for the first ligand binding event.

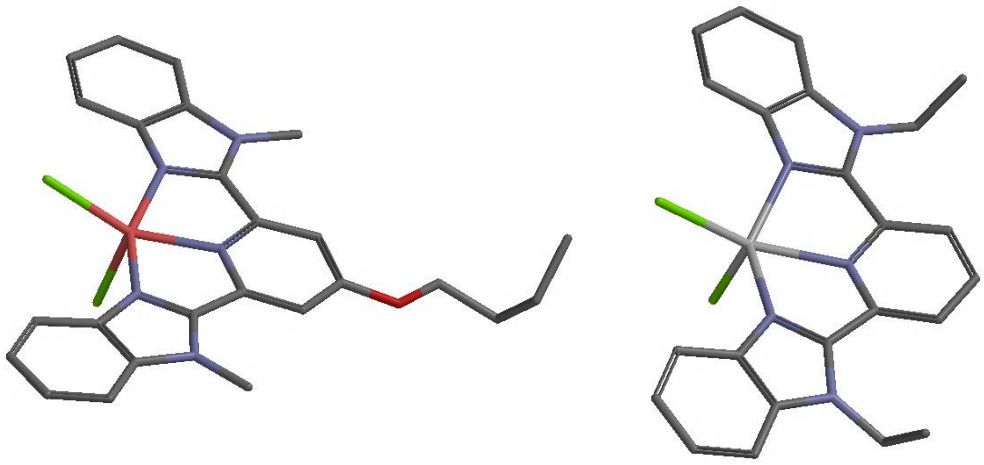

Figure 10. Crystal structures of one MeBip-type ligand bound to the pertinent metals. Left: Crystal structure POHXUI[77] from the Cambridge Structural Database of a MeBip-type ligand bound in a planar conformation to a Cu(II) center with 2 chlorides completing the coordination sphere. Right: Crystal structure VAPVIT[78] from the Cambridge Structural Database of a MeBip-type ligand bound in a planar conformation to an Fe(II) center with 2 chlorides completing the coordination sphere.

The less prominent absorbance increase after one equivalent of added ligand **3** to copper(II) is also attributed to binding of the ligand to the copper(II) center. However, Kotova, et. al and Allmann, et. al have reported that the binding of a second terpyridine, a structurally similar ligand, to copper is much weaker than the first[79,80]. It is likely that this is the case with ligand 3 as well. Additionally, as seen in crystal structure GEPSOJ[81] of copper(II) with two MeBip ligands, the second ligand does not bind in a tridentate, fully planar conformation as the first ligand does, but rather is bidentate and nonplanar (Figure 11). This decrease in planarity compared to the first bound ligand results in a lesser increase in absorbance at 360 nm as the second equivalent of ligand binds to the Cu(II) centers compared to the increase in absorbance observed for the first binding

event. The different modes of the first ligand and second ligand binding to the Cu(II) center would explain the broad inflection at 1:1 ligand:metal ratio and the plateau beginning at 2:1 ligand:metal ratio.

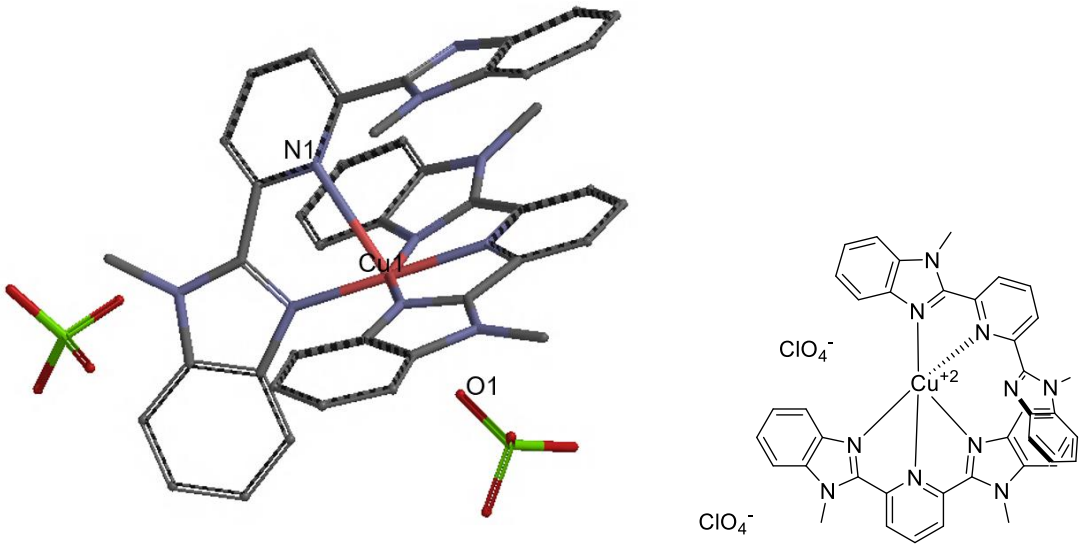

Figure 11. Representations of bidentate ligand binding to Cu(II). Left: crystal structure of Cu(II) complex GEPSOJ[81] from the Cambridge Structural Database. Right: schematic representation of the same complex.

There are fewer reports of MeBip-type ligands binding with copper in the literature. Jackson, et al. report that copper coordinates to MeBip-type ligands on acrylate polymers[62] and cites evidence from terpyridine-based studies that the second ligand binding is dynamic.[80] This claim is supported by viscometry results; the addition of copper results in barely any increase in viscosity, which would be the case if few crosslinks are forming in solution or if they exchange quickly.[62] Conversely, the zinc and cobalt solutions in the study, assumed to have strong 2:1 ligand:metal binding,

demonstrated a significant increase in viscosity upon addition of the metal salt in a 1:2 ratio with the ligand.

Overall, the evidence gathered from these spectroscopic studies points to 2:1 3:Fe(II) binding and 3:Cu(II) binding, though it seems that the first ligand's coordination to copper is stronger than that of the second ligand.

3.2 Metal-Crosslinked Elastomers

As it was confirmed through spectroscopic studies that both copper(II) and iron(II) were binding in a 2:1 ligand:metal fashion, both could be used as crosslinks in networks. However, the binding stoichiometry does not preclude the formation of aggregates and microphase separation upon introducing these complexes into bulk materials. Therefore, we next sought to characterize the morphology of solid films by dynamic scanning calorimetry (DSC) and small- and wide- angle X-ray scattering (SAXS and WAXS, respectively).

3.2.1 Network Formation

Polymer P1 was made by ROMP and characterized by ^{1}H NMR, the spectrum of which is shown in Figure 12. Based on ^{1}H NMR integrations, the chelating monomer **3** was incorporated at 4.7 mol%, close to the 5 mol% feed ratio used. The incorporation of the chelating monomer was determined by comparing the integration of proton H_A in Figure 12 with that of the total vinyl proton region from δ = 5.42-5.25 present for every

repeat unit. This value was used to determine the appropriate amount of metal salt to add when casting films.

Additionally, gel permeation chromatography (GPC) with a multi-angle light scattering (MALS) detector was used to determine the molecular weight of the polymer to be 21.6 kDa. This molecular weight and integration of proton A were used to calculate that there are on average 5 to 6 chelating sites per polymer chain.

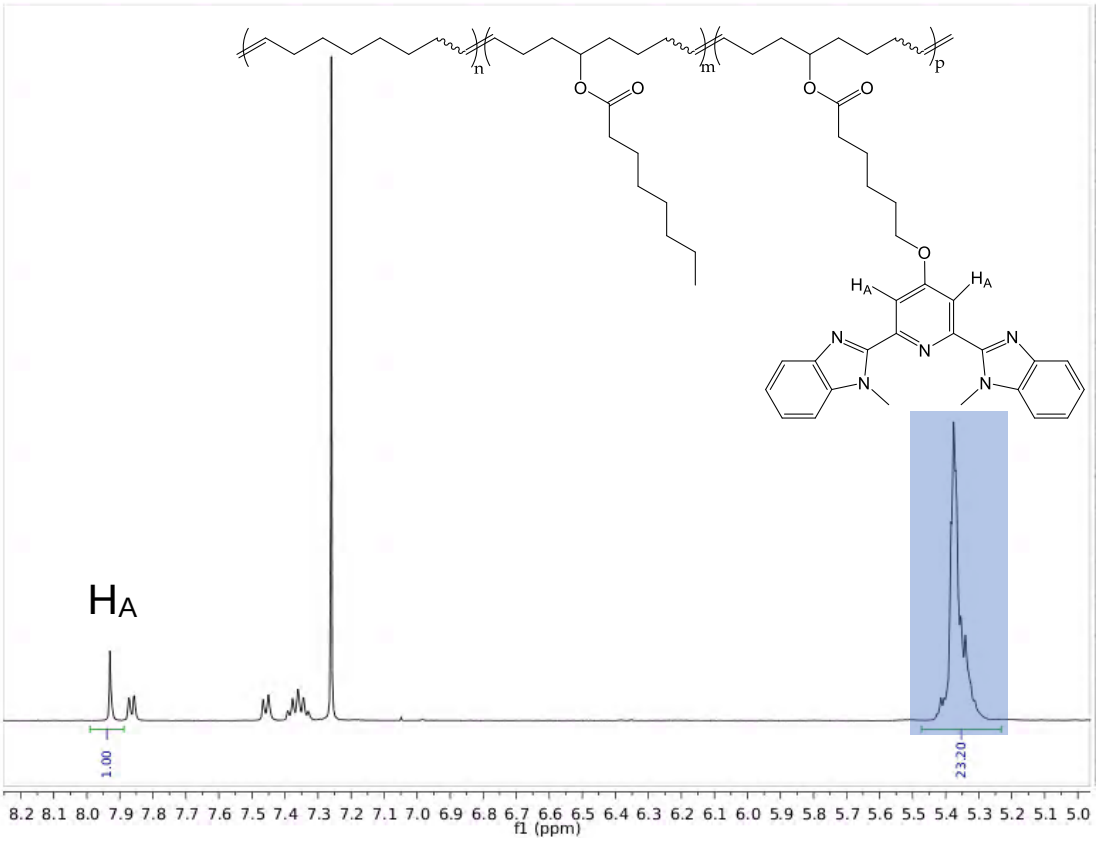

Figure 12. Vinyl and aryl proton region of the ^{1}H NMR spectrum of P1.

3.2.2 Network Morphology

DSC, SAXS, and WAXS were utilized to characterize the morphology of the films cast for rheology, tensile testing, and DMA. Films F1●Cu, F1●Fe, and F1 were tested by DSC within the range of -50 °C to 150 °C to discern the presence and temperature of any phase transitions. The uncrosslinked film F1, in black in Figure 13, exhibits a transition at approximately 9 °C that is attributed to the backbone crystallization temperature because it is a smooth step where the heat capacity after transition is similar to before, rather than a step where the heat capacity is different before and after as would be the case for a glass transition.[82] Additionally, the peaks during heating and cooling are separated, rather than at the same temperature, as would be the case for a phenomenon that required nucleation and growth, such as crystallization. The two crosslinked films exhibit nearly identical curves (F1●Cu in green and F1●Fe in purple in Figure 13) with a slightly sharper transition at approximately 5 °C. This is also attributed to a crystallization of the polymer backbone because it overlaps with the crystallization of F1. Crystallization temperatures are dependent upon preparation conditions,[1,82] so the small difference between the polymer's crystallization temperature in the metalated and unmetalated films is not unreasonable since the unmetalated film was prepared without metal and therefore has different entanglement architecture (discussed in Section 3.3).

Furthermore, simply the interaction of the metal and counterion with the polymer could shift the crystallizations by a few degrees. Notably, there are no

significant features in any of the films above room temperature (here measured to be 23 °C), which indicates that there are not crystalline or glassy features in the films at temperatures of 15 to 150 °C. Additionally, only one transition is observed, consistent with the hypothesis that the metalated complexes are not separately crystallizing. It is possible but unlikely that the crystallization peaks overlap or that are so small that they appear on the DSC curve as one feature.

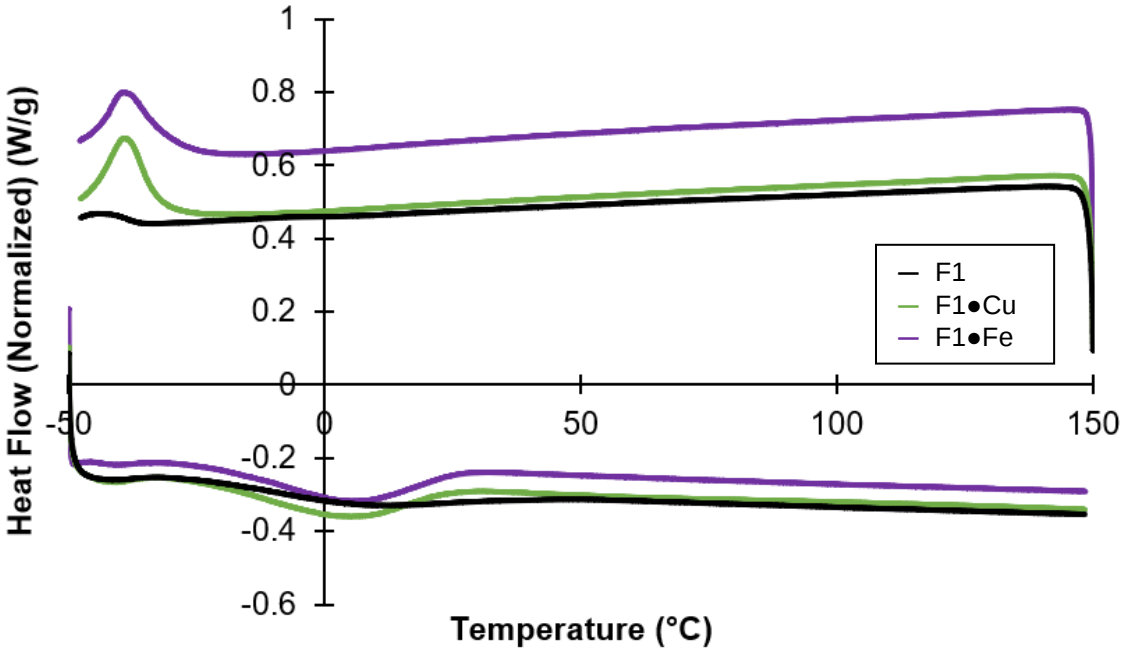

Figure 13. Differential Scanning Calorimetry data. DSC curves (second cycle) for the iron-crosslinked film F1●Fe (purple), the copper-crosslinked film F1●Cu (green), and the uncrosslinked control film F1 (black).

Films F1●Cu, F1●Fe, and F1 were further investigated for microstructures by SAXS and WAXS. The most prominent signal in the WAXS spectrum is a feature observed in all three samples (uncrosslinked F1, Cu(II) crosslinked F1●Cu, and Fe(II)

crosslinked F1●Fe) that corresponds to approximately two angstroms, which is attributed to the spacing between polymer chains themselves (Fig. 14, left). However, in SAXS, a prominent peak corresponding to $1/q$ = 11.8 Å is observed in F1●Cu and F1●Fe that is not observed in F1 (Fig. 14, right). This peak is attributed to small aggregates of the metal-ligand complexes. The uncrosslinked film F1 does not display the 11.8 Å signal, but it does display a broader signal peaking at $1/q$ of approximately 30 Å. This signal is not present in either coordinatively crosslinked film. It is possible that this signal is due to aggregation of the uncrosslinked ligand sidechains in the film F1. Upon fitting with equation 8 between q values of 0.05 and 0.15 based on the method by Yarusso and Cooper (equation 8),[83] the radii of the aggregates R_a and radii of closest approach R_c were found from the peaks as shown in Table 1. See Appendix for fitting and information on Porod scattering.

$$I(q) = I_e(q)V * \frac{1}{v_p} * {v_a}^2 * \rho^2 * \phi^2(qR_a) * S(q, R_c, R_a) \qquad \text{Equation 8}$$

where the structure factor $S(q, R, R)$ is

$$S(q, R_c, R_a) = \frac{1}{1 + 8\frac{v_c}{v_p}\epsilon\phi(2qR_c)} \qquad \text{Equation 9}$$

and

$$\phi(x) = \frac{\sin(x) - x\cos(x)}{x^3} \qquad \text{Equation 10}$$

$$v_a = \frac{4\pi {R_a}^3}{3}$$

$$v_a = \frac{4\pi {R_a}^3}{3}$$ Equation 11

$$v_c = \frac{4\pi {R_c}^3}{3}$$ Equation 12

So,

$$I(q) = \frac{S_0 {r_e}^2 (1 + cos^2\theta)}{2} V * \frac{1}{v_p} * \left(\frac{4\pi {R_a}^3}{3}\right)^2 * \rho^2 * \left(3\frac{\sin(qR_a) - qR_a\cos(qR_a)}{(qR_a)^3}\right)^2 * \frac{1}{1 + \left(8 * \frac{4\pi {R_c}^3}{3} * \frac{1}{v_p} * \epsilon * 3\frac{\sin(2qR_c) - 2qR_c\cos(2qR_c)}{(2qR_c)^3}\right)}$$

Equation 13

$$I(q) = A * \frac{4\pi {R_a}^3}{3} * \left(3\frac{\sin(qR_a) - qR_a\cos(qR_a)}{(qR_a)^3}\right)^2 * \frac{1}{1 + \left(8 * \frac{4\pi {R_c}^3}{3} * B * 3\frac{\sin(2qR_c) - 2qR_c\cos(2qR_c)}{(2qR_c)^3}\right)}$$

Equation 14

in which the parameters *A* and *B* are

$$A = \frac{S_0 {r_e}^2 (1 + cos^2\theta)}{2} V * \frac{1}{v_p} * \rho^2$$ Equation 15

$$B = \frac{1}{v_p} * \epsilon$$ Equation 16

where S_0 is the incident energy flux, r_e is the classical radius of an electron , θ is the angle of the incident beam, V is the volume of sample illuminated by the beam, v_p is the volume of polymer associated with each aggregate, ρ is the electron density of the aggregate, and ϵ is the dielectric constant of the aggregate.

Table 1. Fitting parameters for SAXS curves using equation 14.

	F1●Fe		F1●Cu		F1	
	value	+/-	value	+/-	value	+/-
A	1.32E-05	1.25E-07	3.13E-05	2.56E-07	6.86E-06	1.03E-07
B	3.87E-06	2.25E-08	3.00E-06	1.94E-08	1.46E-07	5.07E-09
R_a (Å)	16.73	0.09	16.53	0.07	26.95	0.20
R_c (Å)	32.05	0.05	32.23	0.06	65.29	0.39

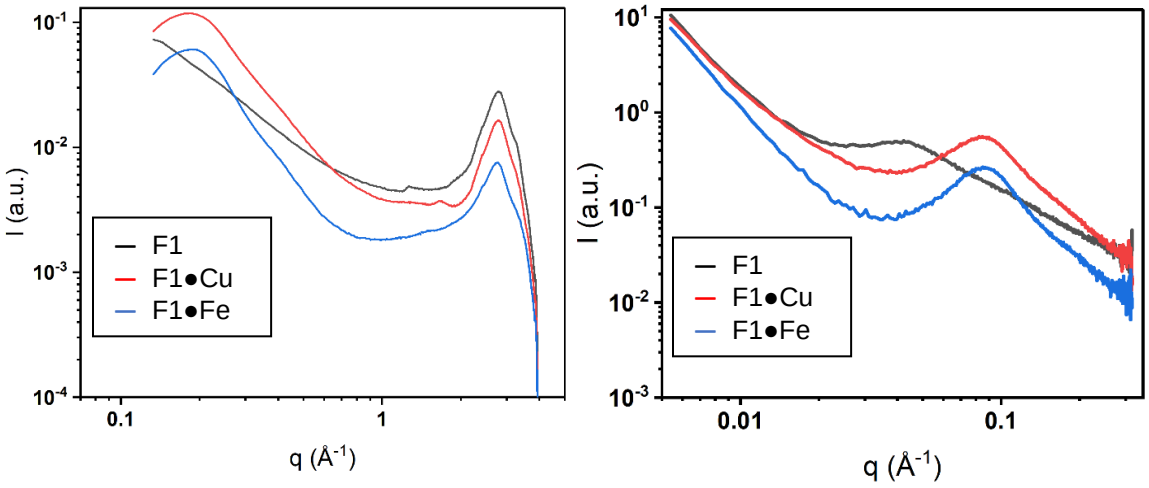

Figure 14. X-Ray Scattering data. WAXS (left) and SAXS (right) spectra of F1●Cu, F1●Fe, and F1. Data collected by Yunxin (Grace) Yao.

Using the R_a listed in Table XXX and the diameter of an individual complex as determined by geometry optimization at the semiempirical level using the PM3 method in Spartan (11.9 Å), there are approximately 2-3 complexes per aggregate. These are

quite small aggregates, and while not ideal, are of equivalent size and spacing between the two metal species used. This similarity will allow for direct comparison between the films' mechanical properties under the assumption that differences are due to the metal identity rather than to the size or spacing of these small aggregates.

3.3 Crosslink Density

We next consider whether the difference in mechanical properties of metalated versus unmetalated films can be reasonably attributed to crosslinking, as intended. To analyze the crosslinking, the storage moduli G' were used to determine ν, the molar density of active strands. To obtain G', films F1●Cu, F1●Fe, and F1 were characterized with a frequency sweep at 23 °C in air using 8 mm parallel plate geometry at 0.25% amplitude. The rheological data are shown in Figure 18. F1●Cu and F1●Fe have frequency-independent storage moduli of 1.22 MPa and 1.23 MPa, respectively from 0.1 to 100 rad/s. The storage modulus of F1 shows a slight frequency dependence across the same frequency range. The loss moduli of the metallated films both begin to curve upwards at low frequencies. This curve suggests the beginning of a peak due to relaxation of the crosslinks, which is supported by the absence of such a feature in the loss modulus of F1. Additionally, the low frequency regime of the relaxation feature means that crosslink relaxation is on the timescale of hours, rather than the several minutes required for the experiments used in this work.

The storage modulus is similar for F1●Fe and F1●Cu, and in the frequency regime tested they were close to that of F1. This indicates that: a) the storage modulus in the elastomeric state is dominated by physical entanglements also present in the uncrosslinked polymer, and b) that the number of active crosslinks in the two metal-crosslinked films is similar, supporting the conclusion that both copper(II) and iron(II) are binding 1:2 with the ligand in the solid state, and that they are both reacting effectively to form similar numbers of crosslinks within the polymer environment.

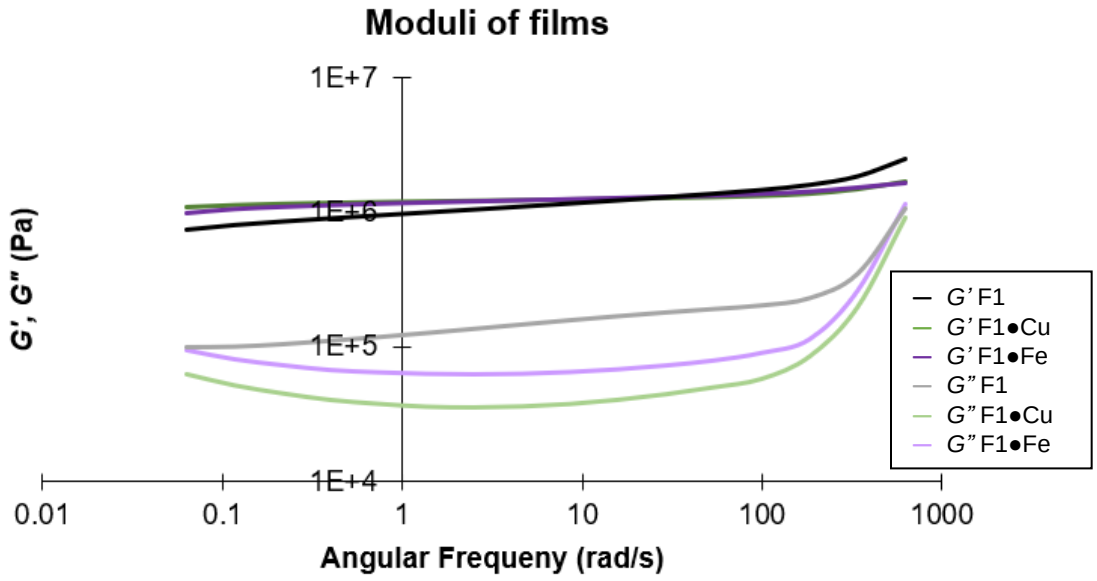

Figure 15. Data from rheological frequency sweeps of films. Storage and loss moduli of F1●Cu, F1●Fe, and F1 at 23 °C and 0.25 % amplitude using 8 mm parallel plate geometry.

If we take the storage modulus *G'* at X Hz of F1 to be an accurate representation of the contribution of entanglements, then the difference in *G'*(F1) and *G'*(F1●M) is an estimate of the modulus contributed by the metal-ligand crosslinking.

$$\Delta G'_{FeL} = G'(\boldsymbol{F1●Fe}) - G'(\boldsymbol{F1}) \qquad \text{Equation 17}$$

$$\Delta G'_{FeL} = 1.23\ MPa - 1.06\ MPa \qquad \text{Equation 18}$$

$$\Delta G'_{FeL} = 1.23\ MPa - 1.06\ MPa = 0.17\ MPa \qquad \text{Equation 19}$$

We next compare $\Delta G'_{ML}$ to the change in modulus expected. We employ the phantom network model of rubber elasticity, which is more appropriate for network in which junctions are subject to considerable fluctuation, such as F1●Fe and F1●Cu. The affine model assumes affine translation of junctions with deformation of the network, while the phantom network model assumes that these crosslinks are not fixed in space and so experience fluctuations in position. Higher junction functionalities, junctions with more strands coming from them, create more intermolecular connections and thereby reduce junction fluctuations[60]. Functionalities of both 3 and 4 are low, so there should be considerable junction fluctuation in our networks. For a functionality of 4, the region of radius r_0 is indeed half that of the free chain[84]. Since r_0 increases linearly with chain length, and the chain length between crosslinks M_c in this network is large, half of r_0 corresponds to large fluctuations in our networks. All of these considerations mean that the phantom network is more accurate for our networks due to the large junction fluctuations. So,

$$\nu = \frac{\Delta G'}{RT\left(\frac{f-2}{f}\right)} \qquad \text{Equation 20}$$

where f is the junction functionality. We first consider each M-L complex an independent junction with $f = 4$ (Figure 16), so

$$\nu_{Fe} = \frac{(1.23\ MPa - 1.06\ MPa) * 2}{R * 296K} = 138\ \frac{mol}{m^3}$$ Equation 21

Using the same treatment for F1● Cu,

$$\nu_{Cu} = \frac{(1.22\ MPa - 1.06\ MPa) * 2}{R * 296K} = 130\ \frac{mol}{m^3}$$ Equation 22

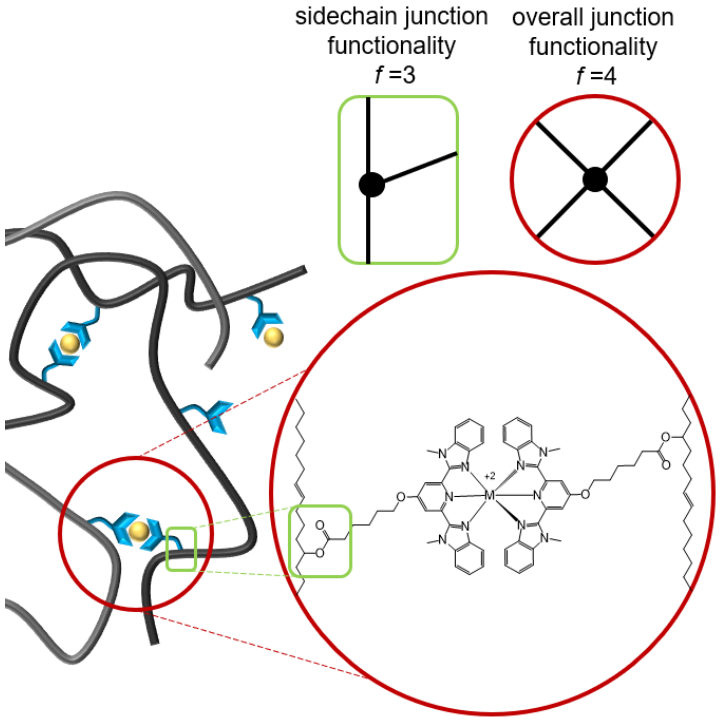

Figure 16. Crosslink functionality. Depiction of a crosslink with *f*=3 junctions where the sidechain meets the mainchain (green) and overall functionality of *f*=4 created by metal crosslinking (red).

If we instead treat an aggregate of 3 complexes as a junction, then the functionality is 12. This results in

$$\nu_{Fe} = \frac{(0.17\ MPa)}{RT\left(\frac{5}{6}\right)} = 83\ \frac{mol}{m^3}$$ Equation 23

$$\nu_{Cu} = \frac{(0.16\ MPa)}{RT\left(\frac{5}{6}\right)} = 78\,\frac{mol}{m^3}$$ Equation 24

If every crosslinking unit in the polymer were bound in 2:1 complex, then the concentration of the metal ion can be used to represent the ideal value $\nu_{calculated}$:

$$[M] = \frac{mol\ M}{\left(mass\ F1 \div \rho(F1)\right)}$$ Equation 25

$$[Fe] = \frac{1.37 * 10^{-5}\ mol\ Fe(OTf)_2}{\left(\frac{105.56\ mg\ F1}{1000000\,\frac{mg}{kg}} \div 848\,\frac{kg}{m^3}\right)} = 110\,\frac{mol}{m^3}$$ Equation 26

$$[Cu] = \frac{1.34 * 10^{-5}\ mol\ Cu(OTf)_2}{\left(\frac{105.49\ mg\ F1}{1000000\,\frac{mg}{kg}} \div 848\,\frac{kg}{m^3}\right)} = 108\,\frac{mol}{m^3}$$ Equation 27

Comparing *[Fe]* to ν_{Fe} and *[Cu]* to ν_{Cu}, we find that *[Fe]* and *[Cu]* fall above ν_{Fe} and ν_{Cu} when *f* is 12, but below ν_{Fe} and ν_{Cu} when *f* is 4. Several factors might account for this difference, including topological de fects in the network, the ambiguity of G'_{F1} due to its frequency dependency, or contribution to G'_{F1} from differences in entanglements between **F1** and the metalated films.

The phantom network model does not account for topological defects such as loops or dangling ends.[1] It is well documented that the moduli of real networks typically fall below what is predicted by the phantom network model.[85,86] Thus, the values of ν_{Fe} and ν_{Cu} when *f* is 12 are most realistic. A more complex model that compensated for

loops and dangling ends, such as real elastic network theory (RENT),[86] would lead to a lower $\nu_{calculated}$, but is outside the scope of this work.

Furthermore, the use of the uncrosslinked film as a control for this experiment is not perfect; the presence of crosslinks in the network during its preparation and drying would affect the entanglement of chains and therefore the dry film's modulus. During drying, this control network is not hindered in any way by crosslinks from becoming more entangled as it dries and its concentration increases. Consequently, it likely has more physical entanglements than the metal-crosslinked networks, falsely inflating its modulus in comparison to them. A smaller modulus for the uncrosslinked F1 sample would result in a higher observed ν_{Fe} and ν_{Cu}, closer to the calculated value if f is 12.

In reality, $\nu_{calculated}$ should be lower using a theory such as RENT[86] and the observed ν_{Fe} and ν_{Cu} should be higher, bringing the two values into better agreement assuming f is 12. Therefore, we conclude that, not only is the number of Fe(II) crosslinks similar to that of Cu(II) crosslinks, but also the extent of modulus increase observed in the metalated films is consistent with what can be attributed to crosslinking, as intended, and that it is more realistic to consider a small aggregate as a junction rather than independent crosslinks.

As additional supporting evidence that there are the same number of active crosslinks for Fe(II) and Cu(II), tensile testing at low strains confirms that the Young's moduli of the copper-crosslinked and iron-crosslinked films F1●Cu and F1●Fe are very

similar to one another, as they are in rheological testing (Figure 17). They are also similar to the modulus of the uncrosslinked control film F1, which supports the conclusions that properties are dominated by physical entanglements at low strains. Tensile testing at higher strains reveals differing material properties, as discussed in Section 3.5.

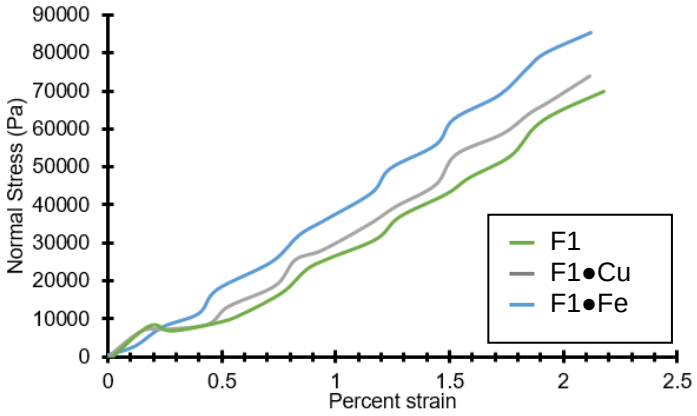

Figure 17. Uniaxial tensile testing at low strains yields very similar moduli for all three films. Testing done at 1% strain per second. Slope from 0.48% to 2% strain is 4.3 MPa (F1●Fe), 3.9 MPa (F1●Cu), and 3.7 MPa (F1). Data collected by Yunxin (Grace) Yao.

3.4 Relaxation of Films

Having verified the similarity of the network structures resulting from different metals in terms of number of crosslinks, we began characterizing the mechanical properties of the elastomers to determine whether there were differences solely due to metal identity. First, the relaxation behavior of the crosslinks was investigated by stress relaxation testing and dynamic mechanical analysis (DMA).

Stress relaxation tests were performed by holding the materials F1, F1●Fe, and F1●Cu at constant strain and constant temperature for an extended period of time. During this time, the stress was monitored.

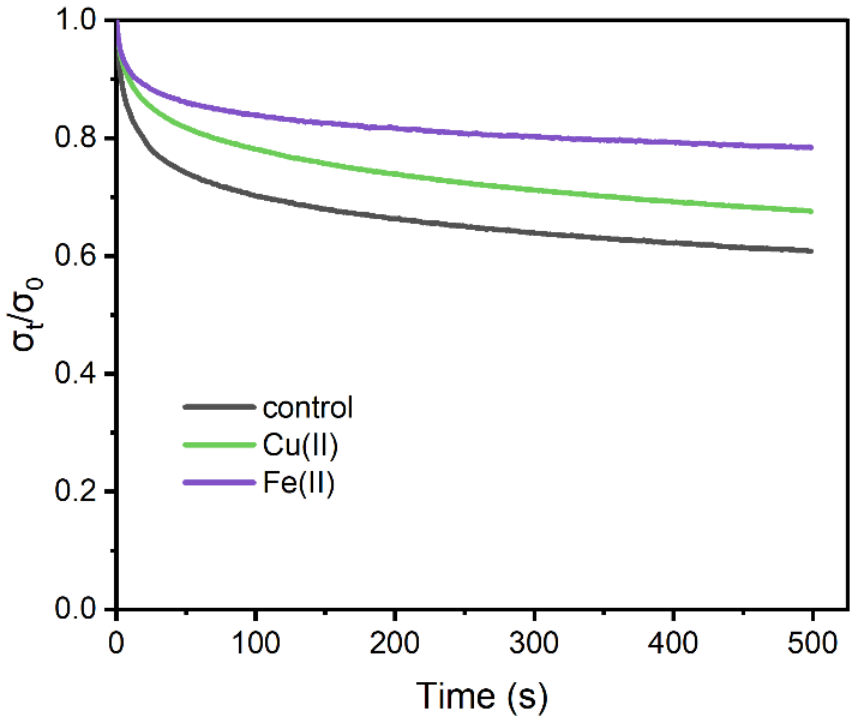

Figure 18. Stress relaxation test curves. F1●Cu (green) relaxes faster than the F1●Fe (purple), but slower than F1 (black), which contains no added metal ions for chemical crosslinking. Data collected by Yunxin (Grace) Yao.

The stress in figure 18 is reported as the stress ratio,

$$stress\ ratio = \frac{\sigma_t}{\sigma_0} \qquad \text{Equation 28}$$

where σ_t is the normal stress at time t after reaching constant strain and σ_0 is the normal stress at the time the constant strain is reached. Figure 18 begins at the time constant strain is reached. The use of the stress ratio allows direct comparison of different

samples because the normal stress at the chosen constant strain is not the same, so presenting the data as ratios compared to each sample's initial normal stress normalizes the curves.

When pulled at 50% strain per second to 50% strain and then held at 50% constant strain for 500 s, it is clear that F1●Cu relaxes more quickly than F1●Fe. The uncrosslinked F1 relaxes fastest, as expected because of the absence of chemical crosslinks; the relaxation observed for F1 is simply a function of physical disentanglement of polymer chains.

At 500 s, the stress in F1●Cu is approximately 0.66 of its initial stress, while for F1:Fe at the same timepoint the stress is 0.78 of its initial stress. Since F1●Cu does not relax to the point of F1, the copper crosslinks are still bearing stress. However, they are relaxing more quickly than the iron crosslinks, more easily dissociating under the experimental conditions.

The observation that the characteristic timescale of copper crosslink relaxation is smaller than that of iron crosslinks is corroborated by master curves obtained from dynamic mechanical analysis (DMA). In DMA, a sinusoidal deformation is applied to a sample and the resulting changes in stiffness and dampening are reported as a function of frequency, from which the storage and loss moduli G' and G'' can be obtained.[87] The frequency and temperature can be modulated over a large range, and this can be used in combination with the principles of time-temperature superposition[88] to obtain a master

curve for a material at a particular reference frequency or temperature. For example, in these experiments, the frequency was changed over a small range at 25 °C to obtain a frequency sweep; this sweep was then repeated at temperature intervals of 5 °C up to 150 °C. The resulting curves are used to obtain information on the moduli over a large range of frequencies at the reference temperature of 25 °C.

From the master curves for F1●Cu and F1●Fe (Figure 19), it is evident that F1●Cu relaxes significantly faster than F1●Fe. This information can be obtained from the local maxima observed in the loss moduli curves at $2.02*10^{-6}$ rad/s in F1●Cu and $2.00*10^{-7}$ rad/s in F1●Fe; the copper crosslinks are relaxing at an order of magnitude higher frequency than the iron crosslinks under the small stress applied during DMA, which is consistent with the observations made from creep testing data.

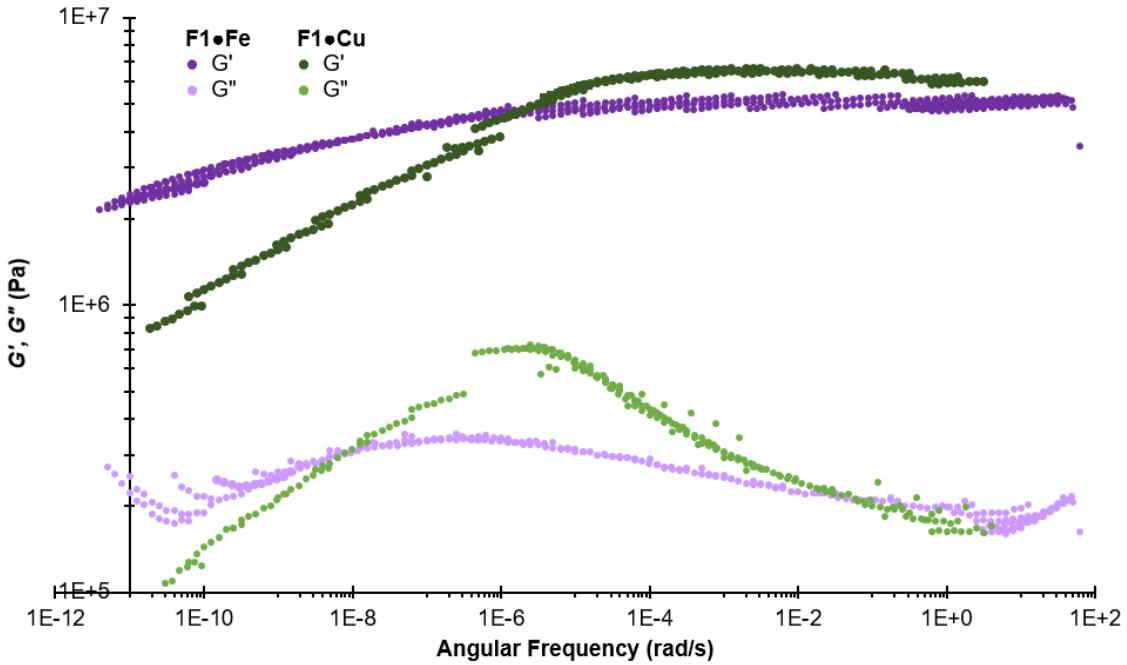

Figure 19. Dynamic mechanical analysis-derived master curves of the metalated films. F1●Fe is in purple and F1●Cu in green. The reference temperature is 25 °C. Data collected from 25 to 150 °C and manually shifted by shift factors listed in Table 2 to obtain the master curve.

The master curve for the unmetalated film F1 (Figure 20) could not be obtained via DMA because the material melted within the temperature range being tested. Instead, a master curve for this material was obtained using shear rheology. This curve does not show the large relaxation feature in the loss modulus evident in the two metalated films, which indicates that these observed relaxations are indeed due to crosslinks.

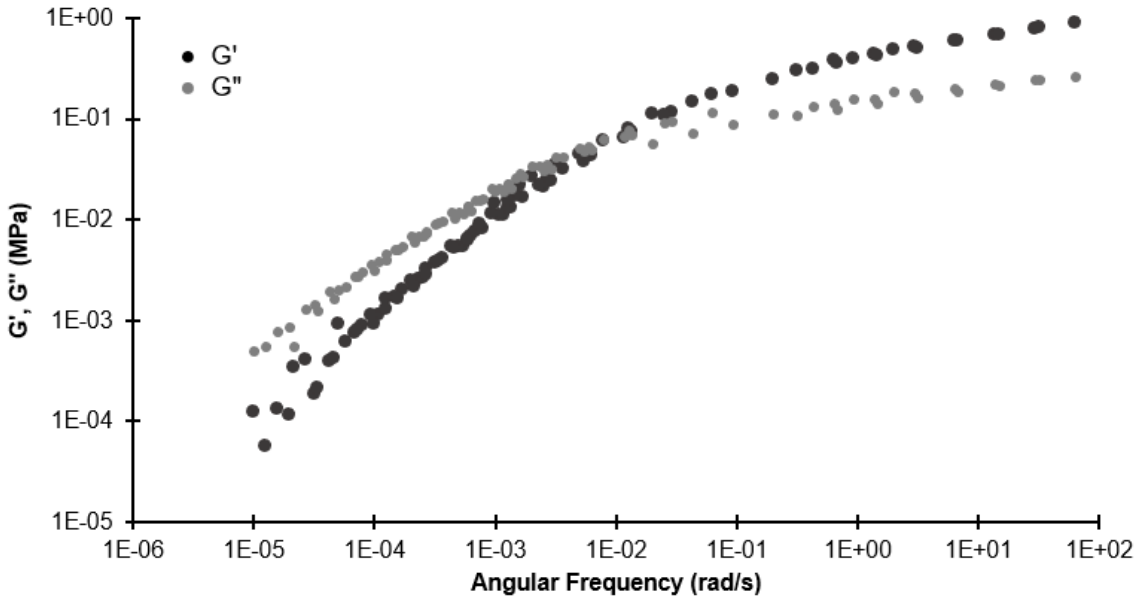

Figure 20. Rheologically-derived master curve for F1. The reference temperature is t 25 °C and the experiments were conducted under nitrogen atmosphere with 25 mm cone and plate geometry and 0.25% amplitude. Data was collected from 25 to 145 °C and manually shifted by the shift factors in Table 2 to obtain the master curves.

Table 2. Shift factors for the DMA-derived master curves for F1●Fe and F1●Cu, as well as the shift factors for the rheology-derived master curve for F1.

T (°C)	shift factor for **F1●Fe**	shift factor for **F1●Cu**	shift factor for **F1**
25	1.00E+00	1.00E+00	1.00E+00
30	7.50E-01	4.50E-01	
35	6.50E-01	1.00E-01	5.01E-01
40	6.00E-01	3.00E-02	
45	5.00E-01	9.00E-03	3.16E-02
50	2.00E-01	3.00E-03	
55	3.50E-02	1.00E-03	1.00E-03
60	3.50E-03	4.00E-04	
65	5.00E-04	2.00E-04	1.00E-03
70	1.00E-04	9.00E-05	
75	2.00E-05	4.00E-05	3.98E-04
80	5.00E-06	2.00E-05	
85	1.00E-06	1.00E-05	2.00E-04
90	2.00E-07	6.00E-06	
95	6.00E-08	4.00E-06	1.26E-04
100	2.00E-08	2.00E-06	
105	1.00E-08	7.00E-07	7.94E-05
110	4.00E-09	3.00E-07	
115	1.00E-09	1.00E-07	5.01E-05
120	3.00E-10	2.00E-08	
125	1.00E-10	5.00E-09	3.16E-05
130	3.00E-11	1.50E-09	
135	8.00E-12	4.00E-10	2.51E-05
140	2.00E-12	1.00E-10	
145	1.00E-12	3.00E-11	2.00E-05
150	5.00E-13	1.00E-11	

Both the creep testing and DMA data indicate the faster relaxation of the copper crosslinks under minimal force as compared to the iron crosslinks, and the comparison of both data sets to the uncrosslinked film data set indicates that there are interactions

contributing to the modulus in the crosslinked films that are not present in the uncrosslinked film, which relies only on physical entanglement for its material properties. This confirms that the addition of metal ions does indeed affect the material properties, most likely by creating crosslinks. Furthermore, we are able to manipulate the material properties of the networks by simply changing the metal salt added.

Another hypothesis for the difference in material properties due to changing the metal identity is possible. Since most of the ligand is occupied in complexes, the exchange time depends not only on dissociation but also on the probability of finding a new partner versus recombining with the old partner. This exchange time is termed the normalized lifetime by Rubinstein and Semenov.[89] It is possible that the normalized lifetime is very sensitive to small differences in concentration of free ligand, meaning that if the preparation procedure yielded metal:ligand stoichiometry that is slightly different for each metal (for example due to increased water absorption by one metal salt), the relaxation times could differ. One way to rule out this possibility would be to compare films in which the metal:ligand stoichiometry was intentionally changed at the limits of uncertainty in stoichiometry. For instance, one could vary the metal added by 1% more and 1% less than the amount calculated to achieve 1:2 metal:ligand stoichiometry, then observe the resultant change in the *G″* relaxation peak. If there was little change, it would support the hypothesis that the difference in relaxation is due to the difference in metal binding dynamics. If there was significant change, it would

support the hypothesis that the difference in relaxation is simply due to imprecise addition of metal equivalents.

3.5 Elastomer Behavior Under High Strains

The material properties of the elastomeric films were further characterized by uniaxial tensile testing to high strains. It was initially hypothesized that F1●Cu would fail at lower strains than F1●Fe because its crosslinks relaxed more quickly, leading us to believe they would be weaker under strain. However, this is not the case.

At high strain during tensile testing, it is obvious that the copper-crosslinked and iron-crosslinked films F1●Cu and F1●Fe exhibit significantly different behaviors (Fig. 21). Both of the metalated films (purple and green curves) exhibit higher tensile stress and extensibility than the unmetalated film F1 (gray curve). The higher tensile stress conforms to expectation because the crosslinks bear some of the stress. The decreased extensibility for the unmetalated films is interesting, because it is expected that an uncrosslinked film would be more extensible than a crosslinked one due to lack of translational constraint of polymer strands by stronger interactions than simple physical entanglements.[90] The low extensibility of F1 could be due to the presence of ligand aggregate "hard phases" in the unmetalated film where there are no aggregates in the crosslinked films, as discussed in Section 3.2 pertaining to SAXS data.

Comparing the two metalated films, F1●Cu exhibits much higher extensibility than the F1●Fe. Initially, the curves are extremely similar, but at strains of

approximately 50 % they start to diverge. The tensile stress of F1●Fe first dips below that of F1●Cu, but then significantly increases to be higher than that of F1●Cu until the film breaks at a lower percent strain than F1●Cu, which indicates that more iron crosslinks are breaking at the same percent strain than copper crosslinks.

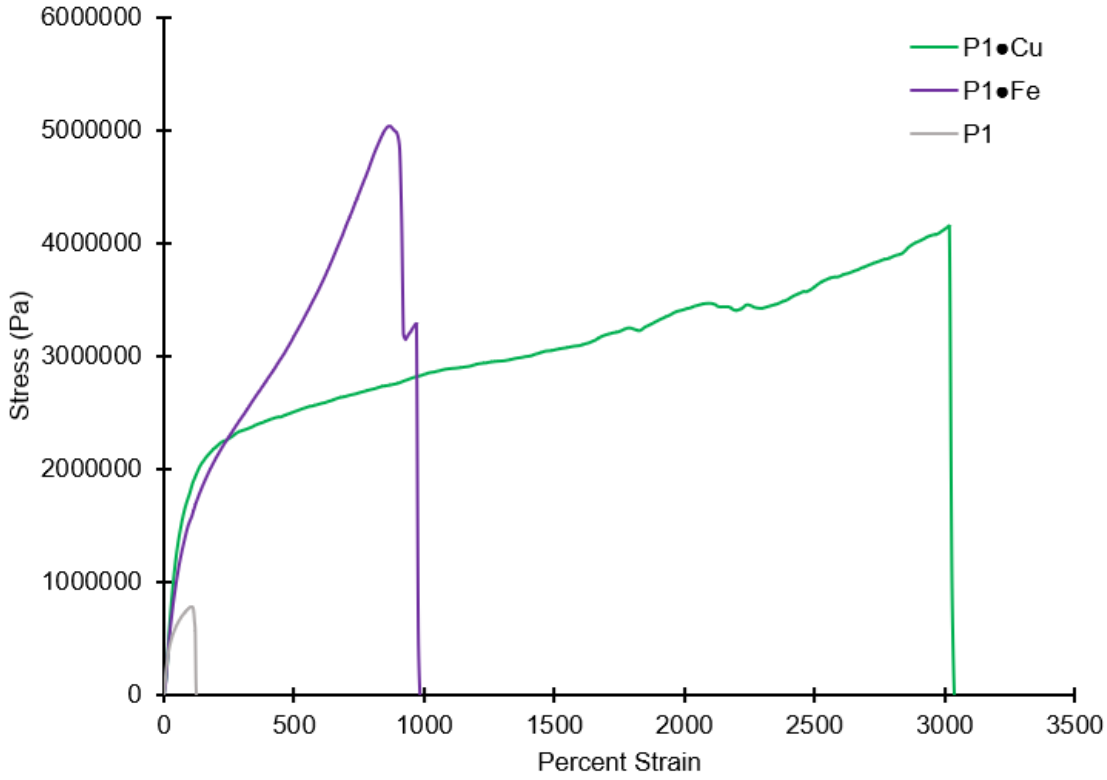

Figure 21. Stress-strain curves for F1●Cu (green), F1●Fe (purple), and F1 (gray) films. These data were collected at a strain rate of 10% strain per second in air at 23 °C. Data collected by Yunxin (Grace) Yao.

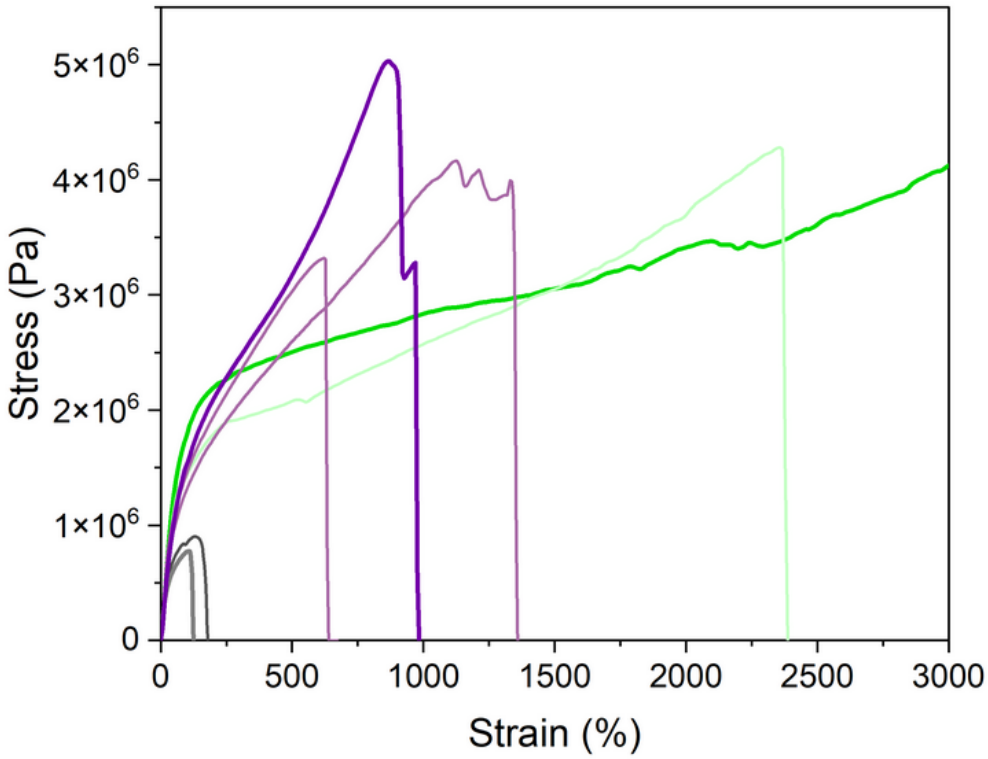

Figure 22. Repeatability of uniaxial tensile testing stress-strain curves at 10% strain rate. Purple curves are for F1●Fe, green curves for F1●Cu, and gray curves for F1. Data collected by Yunxin (Grace) Yao.

3.6 Discussion of Divergent Elastomer Behavior

One hypothesis arising from the uniaxial tensile testing results is that when force is coupled to the reaction coordinate during tensile testing, the iron-ligand bond is more susceptible to force-coupled dissociation than the copper-ligand bond. The effect of mechanical force on chemical kinetics is described in Chapter 2 of this work. Importantly, the extended Bell model enables the use of $\Delta x(0)$ and $\Delta x^{\ddagger}(0)$, the zero-force values of the reaction length and the activation length, respectively, to analyze force coupling.[20] These zero-force lengths and the compliance values $\Delta\chi$ and $\Delta\chi^{\ddagger}$ can be estimated using force-free electronic structure calculations. Collaborators are in the

process of performing such calculations. Preliminary results suggest that it is most thermodynamically stable for both Fe(II) and Cu(II) in the gas phase to have two ligands bound, each in a tridentate manner, to the metal center. They also suggest that the energy required for partial dissociation and full dissociation of the first ligand (Scheme 4) are very similar for both metals, which could indicate that the partially dissociated intermediate is transient. Notably, the dissociation energy is lower for Cu(II) than for Fe(II). Finally, these preliminary computational results show a lower critical force for dissociation for one ligand from Cu(II) than from Fe(II).

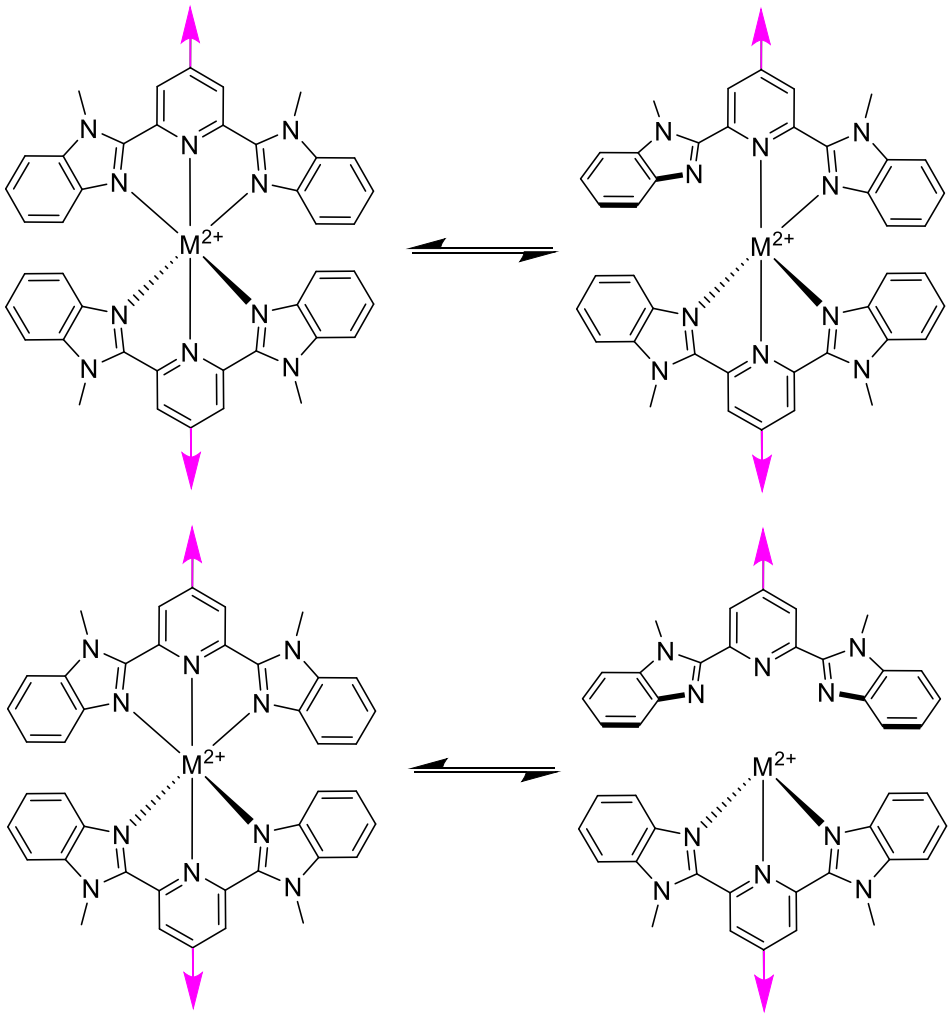

Scheme 4. Dissociation of MeBip from a metal center. Top: Partial dissociation of one Mebip-type ligand to a bidentate conformation. Bottom: Full dissociation of one Mebip-type ligand. Pink arrows represent polymer attachment and pulling points. Triflate counterions omitted for clarity.

These computational results are a recent addition to the data for this project. Previously, literature crystal structures were used to rationalize the differing dissociation behavior for Cu(II) and Fe(II) crosslinks. As mentioned in Section 3.1, based on the only crystal structure of Cu(II) with two MeBip-type ligands,[81] Cu(II) is

pseudooctahedral and binds the first MeBip ligand in a three-coordinate fashion but binds only two of the second ligand's chelating sites (Figure 11). The sixth site in the pseudooctahedral geometry is occupied by a counterion's oxygen atom O1. Both the pyridine N1 of the two-coordinate MeBip and the counterion are more than 0.5 Å further from the metal center than the other coordinating nitrogens. This can be ascribed to an elongational Jahn-Teller effect, present in copper due to degenerate d orbitals in the standard octahedral geometry.[80,91] In this complex, N1 and O1 are occupying the axial positions of the elongated pseudooctahedral structure (Tables 1 and 2).[81] The elongation of these bonds shifts the d^9 Cu(II)'s d orbitals with a z component to lower energy, breaking the degeneracy (Fig. 23).

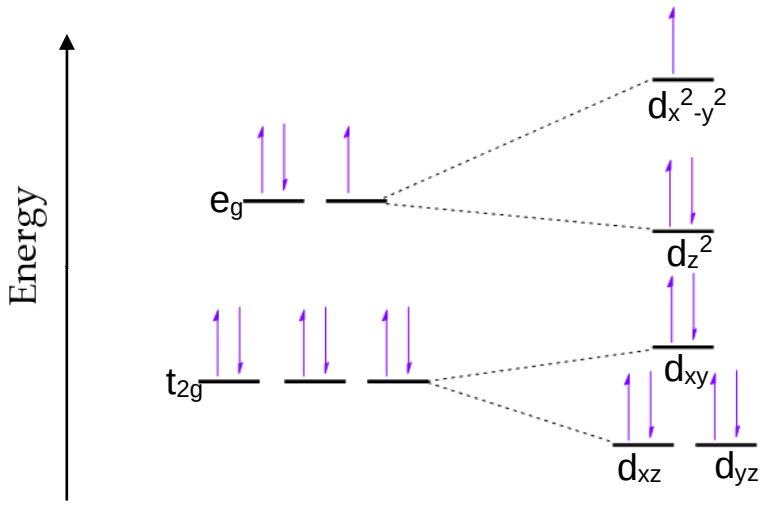

Figure 23. Crystal field splitting diagrams. Diagrams of d orbitals in a d^9 octahedral complex (left) and elongated pseudooctahedral complex experiencing a Jahn-Teller effect (right).

Conversely, Fe(II) binds to all three chelating sites in both ligands at distances within 0.1 Å, making it an octahedral complex.[92] There is not an available crystal structure specifically with MeBip as the ligand, but other Bip-type ligands bind in the described fashion, for example those in Figure 24. The two crystal structures depicted here were chosen because the perchlorate counterion in Figure 24A is comparable to that in the available copper crystal structure, and the triflate counterion in Figure 24B is relevant to the complexes in this work. The effect of the counterion is small, though most metal-nitrogen bonds in the structure with triflate are slightly longer than those in the structure with perchlorate. The counterions are also further from the metal in the triflate-containing crystals than in the perchlorate-containing crystals. The lack of Jahn-Teller distortions indicates that these complexes are low spin because the low-spin state for d^6 iron does not require distortion to reach a low-energy state.

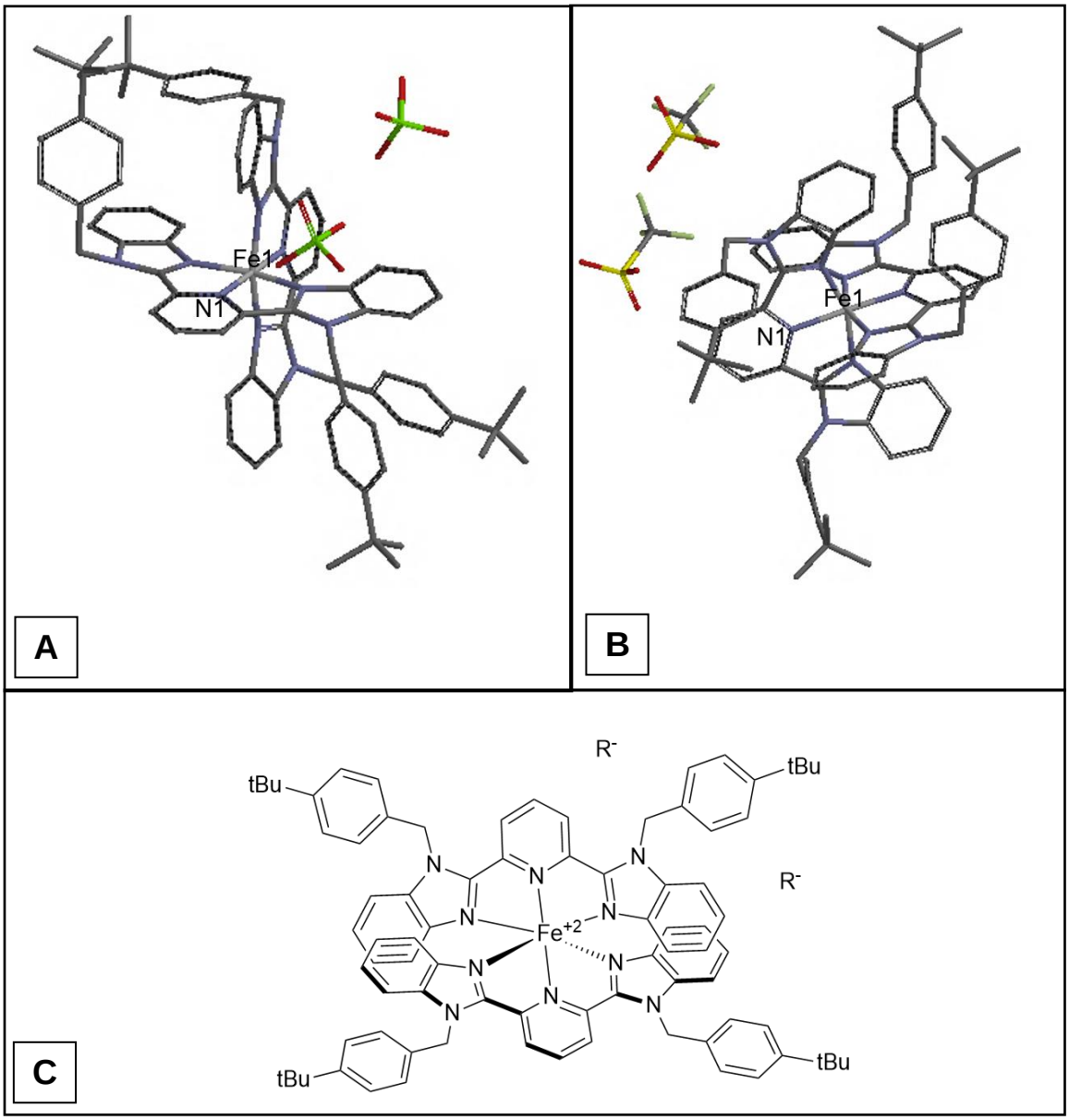

Figure 24. Representations of Fe(II) complexes with MeBip-type ligands. A: crystal structure of Fe(II) complex MAFBII[92] from the Cambridge Structural Database, which has perchlorate counterions. B: crystal structure of Fe(II) complex MAFCIJ[92] from the Cambridge Structural Database, which has triflate counterions. C: schematic representation of top complexes with generic counterion R^-.

Table 3. Metal-nitrogen bond lengths in crystal structures. Dark blue boxes represent full coordination to the metal, light blue represents weak semicoordination, and white represents no coordination.

Crystal structure	Metal	Anion	metal-$N_{pyridine}$ bond 1 (Å)	metal-**N1**$_{pyridine}$ bond 2 (Å)	metal-$N_{imidazole}$ bond 1 (Å)	metal-$N_{imidazole}$ bond 2 (Å)	metal-$N_{imidazole}$ bond 3 (Å)	metal-$N_{imidazole}$ distance 4 (Å)
Fig. 11(left)	Cu(II)	ClO_4^-	1.974	2.510	2.003	2.042	1.959	4.549
Fig. 24A	Fe(II)	ClO_4^-	1.909	1.908	1.956	1.968	1.965	1.964
Fig. 24B	Fe(II)	OTf^-	1.914	1.912	1.971	1.960	1.978	1.946

Table 4. Metal-oxygen distances in crystal structures to the closest oxygen of each counterion. Highlighted blue box represents semicoordination of closest counterion oxygen to the metal center.

Crystal structure	Metal center	Counterion	metal-O (counterion) distance 1 (Å)	metal-O (counterion) distance 2 (Å)
Fig. 11(left)	Cu(II)	ClO_4^-	2.698	5.590
Fig. 24A	Fe(II)	ClO_4^-	5.293	5.288
Fig. 24B	Fe(II)	OTf^-	8.398	7.085

Let us consider these crystal structures to be the starting position for the ligand dissociation reaction, and assume that (a) N1 of the dissociating ligand leaves the Van der Waal's radius of the metal center at approximately the same distance for Fe(II) and Cu(II), and (b) that N1 leaving this radius is the rate determining step for ligand dissociation. If this is the case, then N1 for the Cu(II) structure starts closer to dissociation than N1 for the Fe(II) structure. If we name that distance as $\Delta x^{\ddagger}(0)$ and the energy input W is the same, then the force required for ligand dissociation from Cu(II) should be higher than that required for dissociation from Fe(II) assuming the same compliance χ.

This picture is in direct opposition to our collaborators' preliminary computational results. The computational results are in the gas phase and the solution state (using water as the solvent), rather than the solid crystalline state. It is possible that the dissociation energy is different when solvated, especially with a polar solvent that could stabilize the metal center such as water. The elastomeric films used for the experiments in this chapter do not have a solvent, but the polymer matrix surrounding the complexes is very nonpolar, and so likely has a very different dielectric constant than water. This difference will be taken into account in the next iteration of computational experiments.

3.7 Conclusion

This work has developed a platform to systematically analyze the effects coordinative crosslinking at the elastomer level on mechanical properties. It was determined that the metals chosen for this proof-of-concept study, iron(II) and copper(II), both bound in a 1:2 metal:ligand ratio using small molecule spectroscopic studies. Upon incorporation of the small molecule complexes as crosslinkers in a polymer network, the homogeneity of the networks was confirmed. Furthermore, the effect of the coordinative crosslinking on the material was determined: both metals caused a slight and nearly identical increase in storage modulus compared to an uncrosslinked film, confirming that crosslinking was occurring and occurred to a similar extent for both metals. The frequency dependence of the loss modulus reveals that

relaxation of the copper-crosslinked film occurs more quickly than that of the iron-crosslinked film, indicating that facile manipulation of material properties can be achieved by simply changing the metal salt used in film preparation. This observation is reinforced by testing at high strains, under which the copper-crosslinked films were significantly more extensible than the iron-crosslinked films despite similar active strand density. We tentatively attributed the difference in behavior under force to more effective force coupling to the iron-N1 bond compared to the copper-N1 bond based on literature crystal structures, but computational experiments seeking to explain the divergent force-coupled dissociation behavior is still underway.

As discussed in Chapter 2 of this work and in the introduction of this chapter, there is a significant lack of knowledge connecting the single molecule behavior of organometallic bonds under force to bulk network behavior. This work developed a platform that was implemented in the network area of study, but was designed to be easily extended to linear polymer and single molecule work. Modeled after the system used by Li et al.[26], this polymer system can be used in pulsed ultrasonication studies and, with minor modification, SMFS studies.

The methodology for ultrasonication and SMFS would rely on using the same polymer P1 in SCNPs (Figure 25). To obtain SCNPs for ultrasonication, the preparation conditions would need to be considerably more dilute than described in this work to

avoid inter-strand crosslinking as was desired in films. Dynamic light scattering (DLS) characterization of the resulting SCNPs to determine their size would also be necessary.

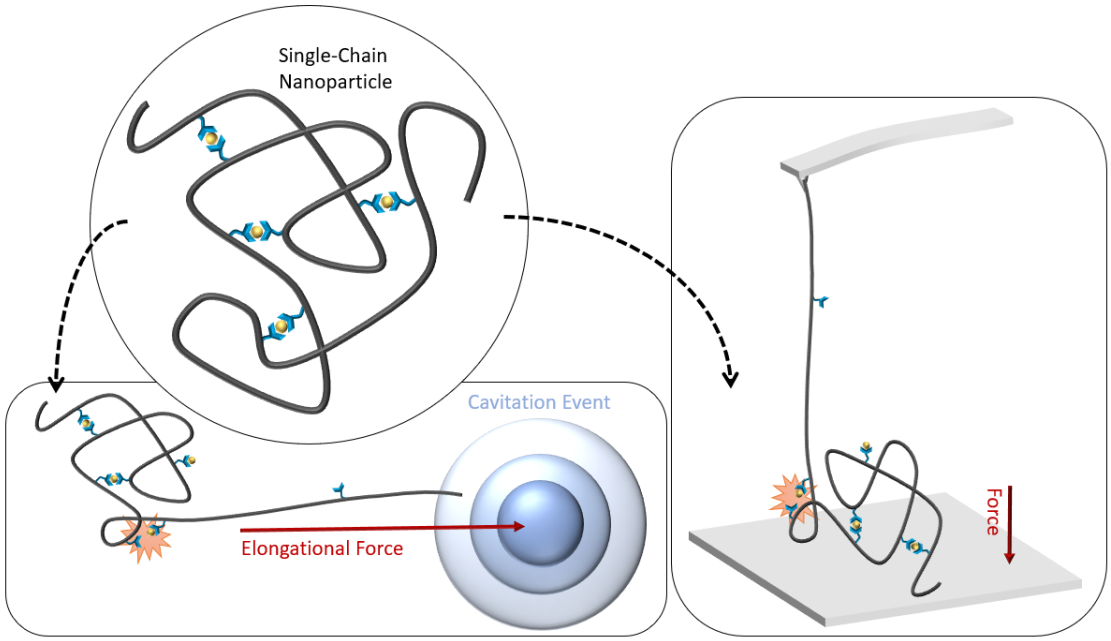

Figure 25. Schematic representation of metal-crosslinked SCNPs for sonication (bottom) and SMFS (right).

To obtain SCNPs for SMFS, *cis*-cyclooctene must be replaced with 9-oxabicyclo[6.1.0]non-4-ene (epoxy-COD) (Scheme 5). Epoxy-COD serves in SMFS to aid in polymer attachment to the cantilever tip. Once this modification is implemented, the same procedure used by Li et al.[26] can be used for SMFS.

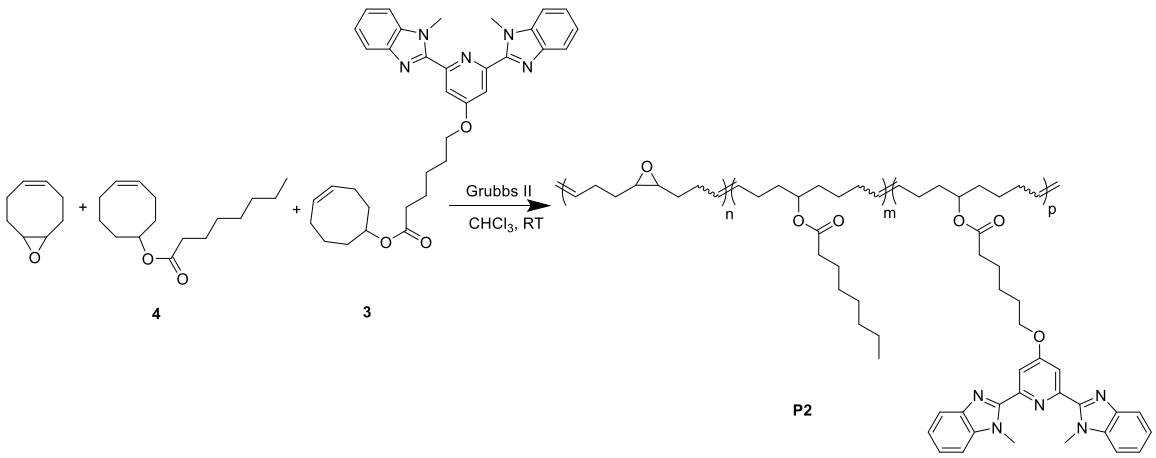

Scheme 5. Syntheis of P2 using 9-oxabicyclo[6.1.0]non-4-ene in place of *cis*-cyccooctene: useful for SMFS.

One difference between the ligand in the aforementioned study and the one used in this work is the denticity; the ligand in the study by Li, et al.[26] is bidentate, while ours is tridentate. The tridentate and bulky nature of the MeBip-type ligands will prevent confusion between tris- and bis- coordinate centers within the SCNPs.

Additionally, the MeBip ligand system is modular in that it allows for alteration of ligand attachment points, as well as substituents that can alter the steric or electronic nature of the ligand. For example, ligand 6 can be easily synthesized as shown in Scheme 6. It can then be used as a force-bearing crosslinker in networks or ring-closed to become a monomer for linear polymers appropriate for ultrasonication and SMFS. This ligand structure dramatically changes the direction of force transduction through the metal center.

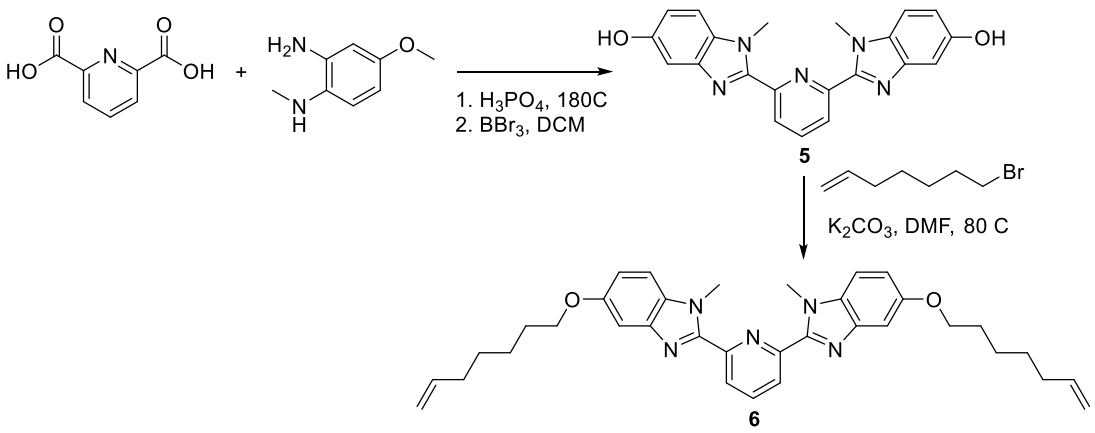

Scheme 6. Synthetic route to a MeBip-type ligand with polymer attachment points at the sides, rather than at the center of the pyridine.

In another example, ligands 7 and 8 can be synthesized and used as sidechains in the same way as discussed in this work (Scheme 7). However, 7 is functionalized with an electron-donating group, while 8 is functionalized with an electron-withdrawing group. This enables the exploration of electronic effects in the ligand sphere and their consequences for force-bearing metal-ligand bonds. A final example is ligand 9, the study of which in the same experiments as described here can elucidate steric effects on the coupling of force to metal-ligand bonds.

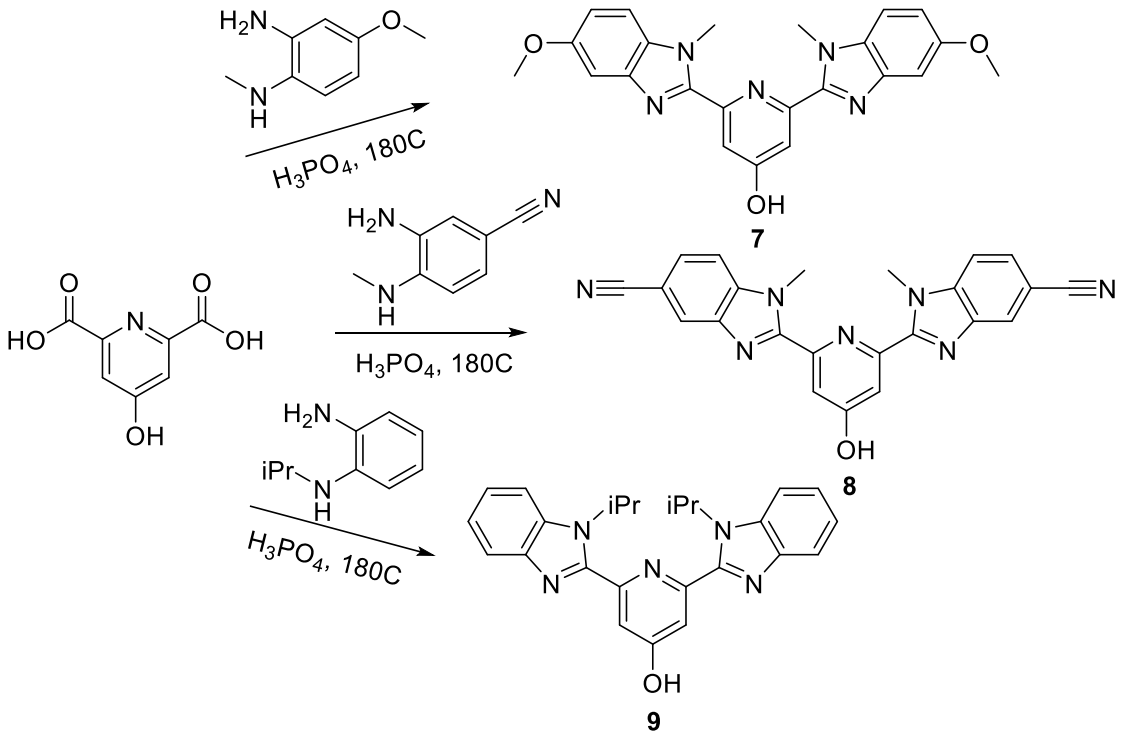

Scheme 7. Facile synthesis of ligands 7-9, incorporating electron-donating, electron-withdrawing, and sterically bulky groups.

In conclusion, this work demonstrates that the MeBip ligand platform as a sidechain for creating homogenous elastomeric networks, the properties of which can be manipulated by simply changing the metal identity. It also lays the groundwork for systematic study of a variety of metals with a modular ligand that provides access to different polymer attachment points, electronic effects, and steric effects.

3.8 Experimental

3.8.1 General Considerations

All reagents and solvents were ordered from VWR, Intl. or Sigma Aldrich and used without further purification. ^{1}H NMR were collected on a Bruker 500 MHz spectrometer with reference to solvent peak $CDCl_3$ (^{1}H $\delta = 7.26$). All chemical shifts are given in ppm (δ) and coupling constants (J) in Hz as singlet (s), doublet (d), triplet (t), quartet (q), multiplet (m), or broad (br). Column (flash) chromatography was performed using Silicycle F60 (230 - 400 mesh) silica gel. Rheological data was collected using an Anton Paar 502e model rheometer. DSC data was collected using a TA DSC2500. Gel permeation chromatography (GPC) was performed with an Agilent 1260 Infinity LC system, using 2 in-series Agilent PLgel mixed-C columns (10 5 Å, 7.5x300 mm, 5 μm, part number PL1110-6500) at room temperature at a flow rate of 1.0 mL/min in THF. Molecular weights were calculated using an in line Wyatt miniDAWN TREOS multi-angle light scattering detector with Wyatt Optilab T-rEX refractive index detector. The refractive index increment (dn/dc) values were determined by online calculation based on injections of known concentration and mass. DMA, Uniaxial tensile tests, and creep tests were performed on a TA Instruments RSA III Dynamic Mechanical Analyzer (force resolution: 0.0001 N, displacement resolution: 1 μm) at Duke University's Shared Material Instrument Facility (SMIF).

3.8.2 Ligand Synthesis

To synthesize 1, chelidamic acid (1.83 g, 10 mmol, 1 eq.) and *N*-methyl-1,2-phenylenediamine (2.44 g, 20 mmol, 2 eq.) were added to a 50 mL round bottom flask with a stir bar. 5.0 mL phosphoric acid (85 wt % in water) was carefully added. The flask was fitted with a condenser and the reaction mixture heated to 180 °C overnight. Upon cooling to room temperature, the reaction mixture was poured into 400 mL stirring deionized water. 3.0 M sodium hydroxide solution was added until a light blue precipitate appeared and the pH was above 7. The precipitate was filtered off and redispersed in 10 wt % potassium carbonate until it turned pink, when it was again filtered off. The pink solid was dissolved in boiling methanol, to which concentrated hydrochloric acid was added until the color changed from dark red to dark blue. Upon cooling, light gray powdery crystals precipitated and were collected by filtration. The product 1 was dried and used without further purification for the synthesis of 3. ^{1}H NMR (500 MHz, DMSO (D_6) δ = 12.31 (s (br), 1H), 8.00 (s, 2H), 7.95 (d, 2H), 7.88 (d, 2H), 7.60-7.52 (m, 4H), 4.30 (s, 6H).

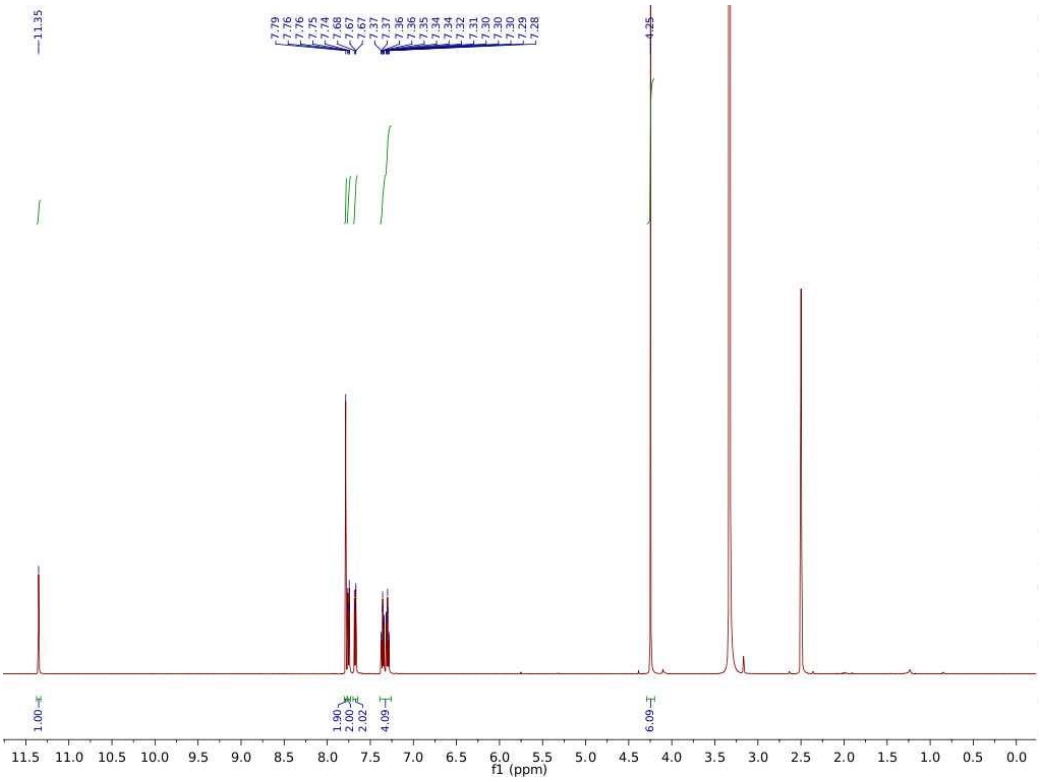

Figure 26. ^{1}H NMR spectrum of 1.

To synthesize 2, (Z)cyclooct-4-enol (1.26 g, 10.0 mmol, 1.0 eq), 6-bromohexanoic acid (2.34 g, 12.0 mmol, 1.2 eq), *N*,*N*′-dicyclohexylcarbodiimide (2.06 g, 10.0 mmol, 1.0 eq), and 4-(dimethylamino)pyridine (122 mg, 1.0 mmol, 0.10 eq) were added to a flame-dried round bottom flask with a stir bar. The flask was closed with a septum and flushed with nitrogen for 10 minutes and then 200 mL anhydrous dichloromethane was added via syringe. The reaction mixture was stirred overnight, and then the white precipitate formed was removed by filtration. The filtrate was dried onto silica and subjected to flash chromatography with an eluent of a gradient of 0 % to 20% ethyl acetate in hexane. The product 2 was collected and dried for use in synthesis of 3. ^{1}H NMR (500 MHz,

$CDCl_3$) δ = 5.72-5.58 (m, 2H), 4.87-4.80 (m, 1H), 3.40 (t, 2H), 2.38-2.25 (m, 3H), 2.19-2.06 (m, 3H), 1.92-1.82 (m, 4H), 1.73-1.65 (m, 2H), 1.66-1.56 (m, 4H), 1.51-1.43 (m, 2H).

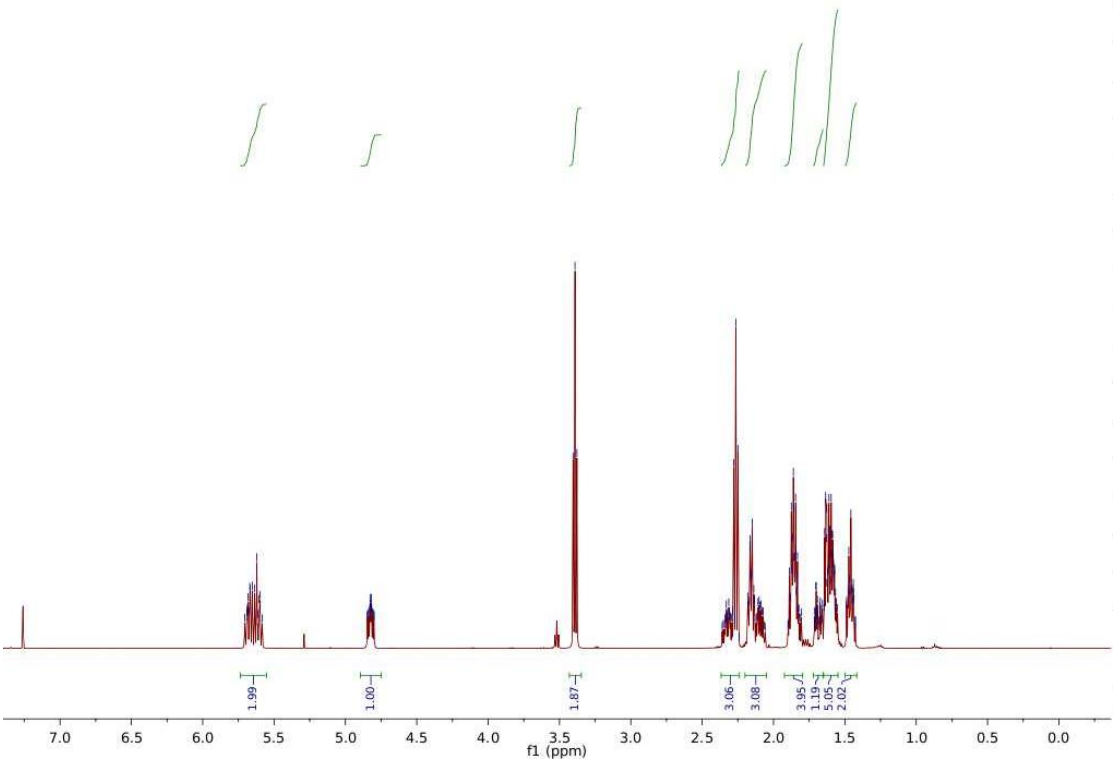

Figure 27. ^{1}H NMR spectrum of 2.

To synthesize 3, products 1 (1.78 g, 5.0 mmol, 1.0 eq) and 2 (1.44 g, 6.0 mmol, 1.2 eq) were added to a flame-dried round bottom flask with a stir bar and potassium carbonate (2.07 g, 15.0 mmol, 3.0 eq). 25 mL anhydrous dimethylformamide was added to the flask and it was fitted with a condenser. The reaction mixture was heated to 80 °C for 48 hours, after which it was cooled to room temperature and triturated with deionized water until the product precipitated as a light pink solid. The solid was redissolved in dichloromethane and then dried onto silica for flash chromatography in 0

to 10% methanol inn dichloromethane. The product 3 was collected as a light pink solid. ^{1}H NMR (500 MHz, $CDCl_3$) δ = 7.93 (s, 2H), 7.87 (d, 2H), 7.73 (d), 7.46 (d, 2H), 7.36 (m, 4H), 5.72-5.58 (m, 2H), 4.87-4.80 (m, 1H), 4.24 (s, 6H), 3.34 (t, 2H), 2.31 (m, 3H), 2.22-2.07 (m, 3H), 1.93-1.82 (m, 2H), 1.75-1.67 (m, 4H), 1.66-1.57 (m, 2H), 1.55-1.50 (m, 2H).

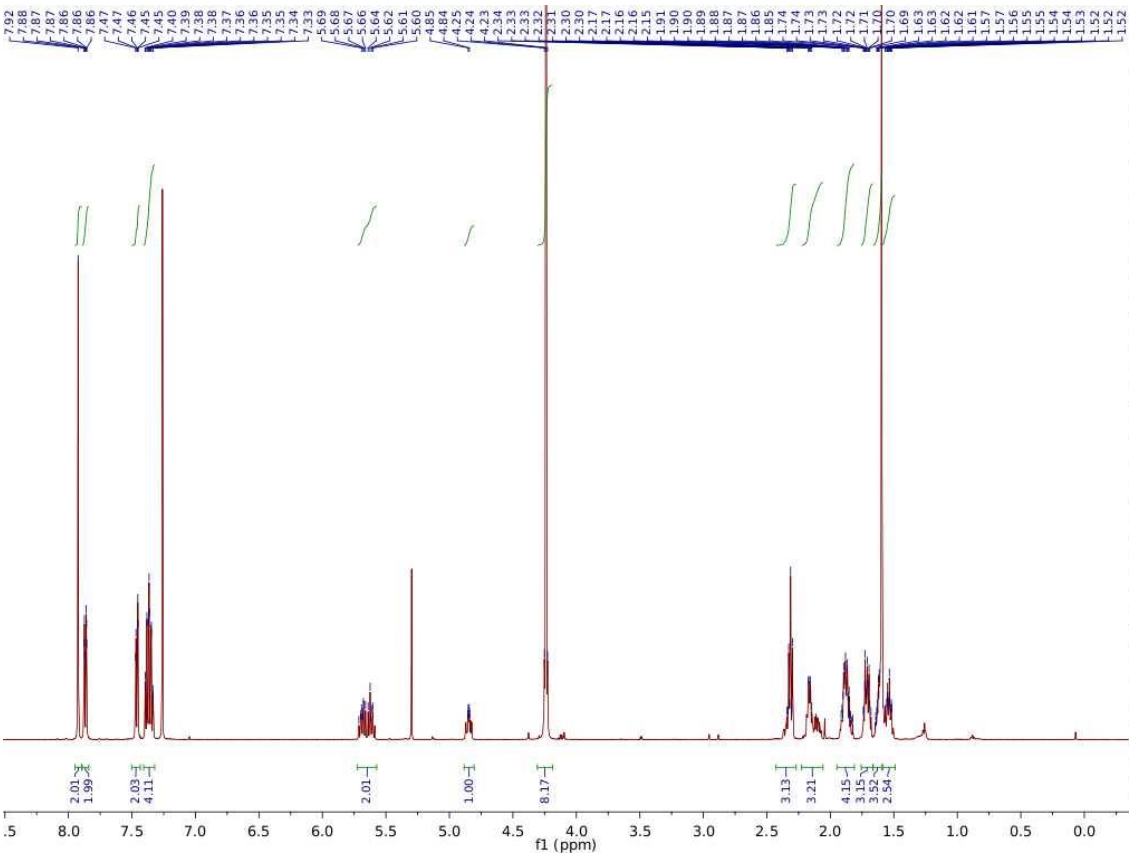

Figure 28. ^{1}H NMR spectrum of 3.

3.8.3 Titration Procedures

The titrations were undertaken in a solvent mixture of 95:5 (volume/volume) toluene: methanol. Toluene was chosen to match the solvent used in gels (see below),

and methanol was added to dissolve the metal salts before complex formation in both the small-molecule experiments.

For iron(II) trifloromethanesulfonate (iron(II) triflate), a 75.8 μM solution of iron(II) triflate was titrated in 5 μL aliquots with a 9.29 mM solution of 3 until four equivalents of **3** compared to iron(II) triflate had been added. A spectrum from 285 to 800 nm was collected upon addition of each aliquot. At the end of the titration, the solution was allowed to stand for 30 min before another full spectrum was collected to confirm there was no change in absorbance over time.

For copper(II) trifloromethanesulfonate (copper(II) triflate), a 66.8 μM solution of copper(II) triflate was titrated in 5 μL aliquots with a 4.65 mM solution of 3 until four equivalents of **3** compared to copper(II) triflate had been added. A spectrum from 285 to 800 nm was collected upon addition of each aliquot. At the end of the titration, the solution was allowed to stand for 30 min before another full spectrum was collected to confirm there was no change in absorbance over time.

In addition, a 33.41 μM solution of copper(II) triflate was titrated in 3 μL aliquots with a 4.65 mM solution of 3 until four equivalents of 3 compared to copper(II) triflate had been added. A spectrum from 285 to 800 nm was collected upon addition of each aliquot. At the end of the titration, the solution was allowed to stand for 30 minutes before another full spectrum was collected to confirm there was no change in absorbance over time.

The ligand itself absorbs in the UV region below 345 nm, but a new UV peak arises upon metal binding that is slightly red-shifted at 355 to 360 nm, depending on the metal species. Increases in absorbance of this peak were used to monitor the ligand binding. Iron(II) triflate also develops a pronounced visible-region metal-ligand-charge-transfer (MLCT) peak at approximately 572 nm, but for best comparison to the copper titrations, the UV peak at 355 nm was used to monitor ligand binding.

3.8.4 Polymer Synthesis

To make monomer 4, (*Z*)-cyclooct-4-enol (1.26 g, 10.0 mmol, 1.0 eq), octanoic acid (1.73 g, 12.0 mmol, 1.2 eq), *N*,*N*′-dicyclohexylcarbodiimide (2.06 g, 10.0 mmol, 1.0 eq), and 4-(dimethylamino)pyridine (122 mg, 1.0 mmol, 0.1 eq) were added to a flame-dried round bottom flask with a stir bar. The flask was closed with a septum and flushed with nitrogen for 10 minutes and then 200 mL anhydrous dichloromethane was added via syringe. The reaction mixture was stirred overnight, and then the white precipitate formed was removed by filtration. The filtrate was dried onto silica and subjected to flash chromatography with an eluent of a gradient of 0 % to 20% ethyl acetate in hexane. Monomer 4 was collected and dried for use in polymerization of P1. ^{1}H NMR in $CDCl_3$ δ 5.64 (2H, m), 4.82 (1H, td J = 7.5 Hz), 2.32 (1H, m), 2.24 (2H, t), 2.16 (2H, m), 2.10 (1H, m), 1.85 (2H, m), 1.69 (1H, dt), 1.59 (5H, m), 1.28 (8H, m), 0.87 (3H, t).

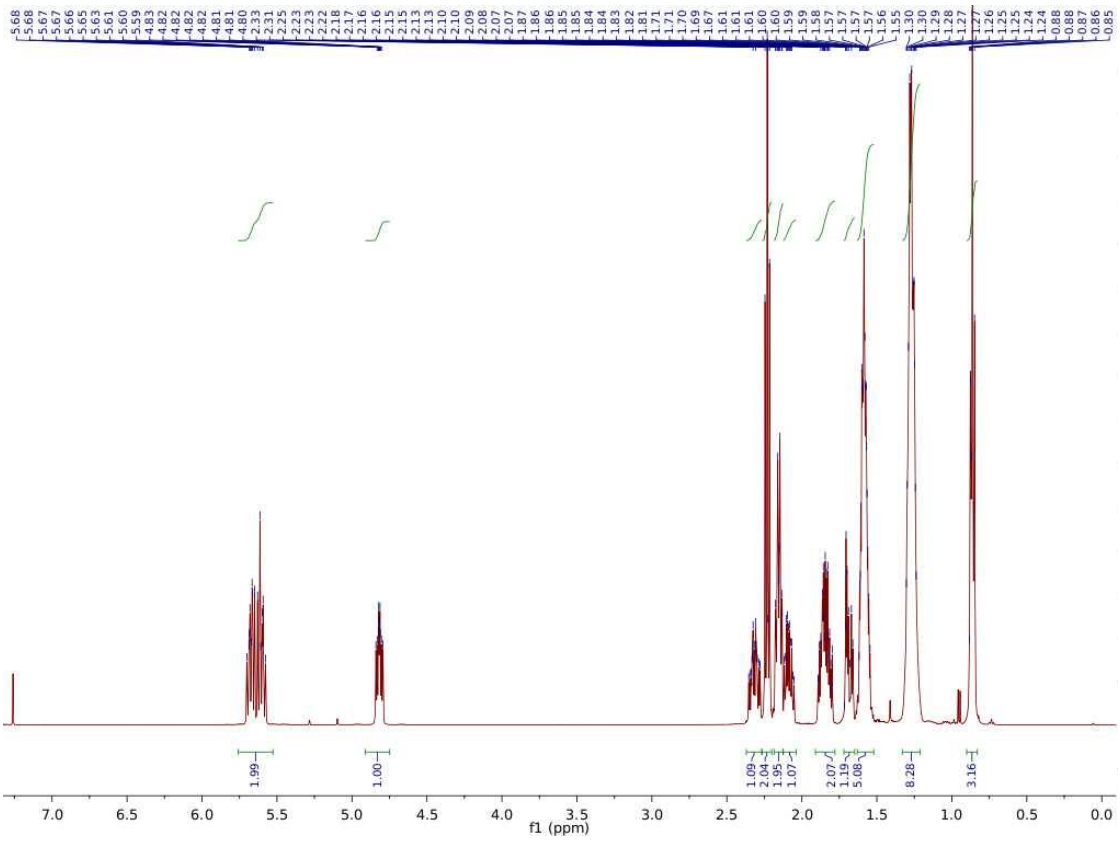

Figure 29. ^{1}H NMR spectrum of 4.

Polymer P1 was synthesized with a feed ratio of 70 mol% cis-cyclooctene, 25 mol% monomer 4 and 5 mol% monomer 3. To synthesize P1, the monomers 3 (619 mg, 5.6 mmol, 0.70 eq), 4 (507 mg, 2.0 mmol, 0.25 eq), and *cis*-cyclooctene (240 mg, 0.40 mmol, 0.050 eq) were added to a 40 mL scintillation vial with a stir bar and a septum cap. The vial was evacuated and refilled with nitrogen three times before 7.50 mL anhydrous chloroform was added via syringe. In a separate, flame-dried 7 mL scintillation vial, 13.9 mg Grubbs II was added. One mL anhydrous chloroform was added to this vial and the Grubbs II catalyst was fully dissolved. From this catalyst solution, 0.5 mL was added to the stirring monomer solution via syringe. The viscosity

of the solution could be observed to increase within five minutes of catalyst addition. The reaction mixture was allowed to stir for six hours, at which point 0.1 mL ethyl vinyl ether was added to quench the catalyst. The mixture was allowed to stir for an additional ten minutes and was then precipitated dropwise into stirring methanol. The gummy solid precipitate was collected and redissolved in minimal dichloromethane, then stirred overnight with Quadrapure-thiourea beads. The beads were allowed to settle to the bottom of the vial, then the liquid was added dropwise to stirring methanol to reprecipitate the product. The gummy solid was again dissolved in minimal dichloromethane and precipitated a third time in stirring methanol, after which it was dried and characterized by ^{1}H NMR and GPC in tetrahydrofuran. ^{1}H NMR in $CDCl_3$ δ 7.93 (s), 7.865 (d), 7.46 (d), 7. 36 (m), 5.44-5.27 (m), 4.92-4.84 (m), 4.24 (s), 2.31-2.24 (m), 2.05-1.90 (m), 1.65-1.47 (m), 1.38-1.22 (m).

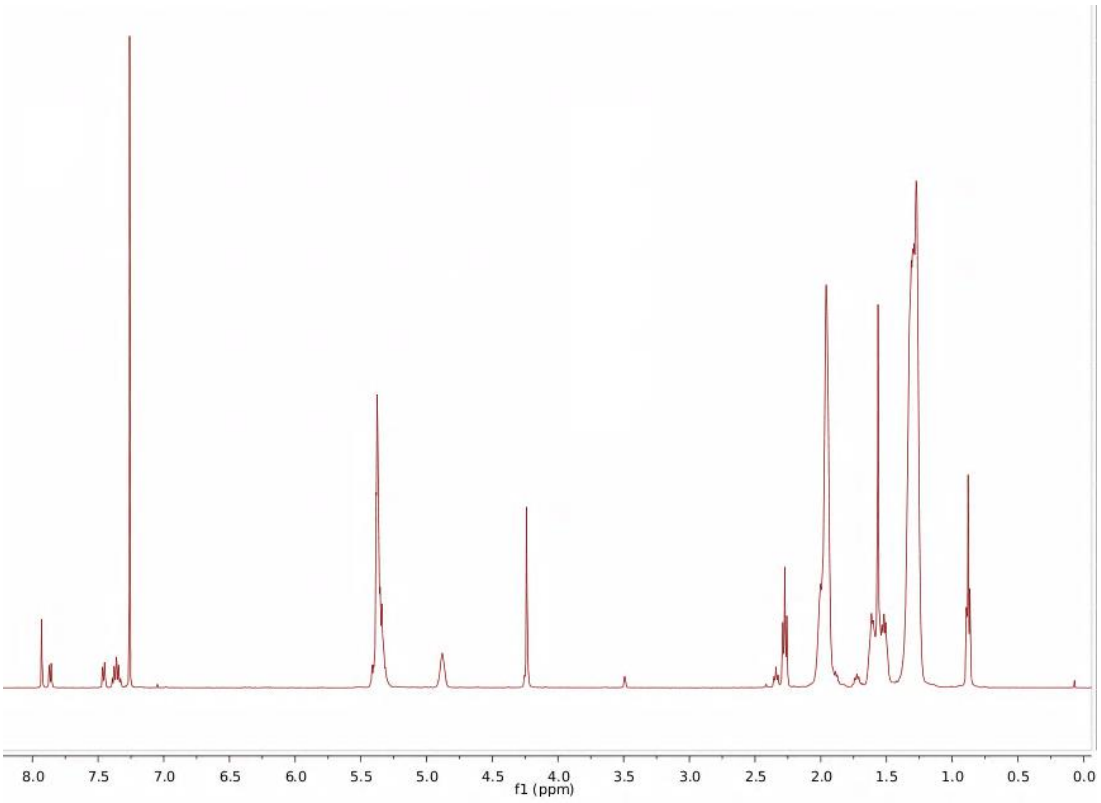

Figure 30. ^{1}H NMR spectrum of P1.

3.8.5 Film Preparation

To make coordinatively crosslinked networks, P1 was dissolved at approximately 10 wght. % in 95:5 chloroform: methanol. Solutions of either ~~i~~ron(II) trifluormethanosulfonate or copper(II) trifluoromethanosulfonate in the same solvent mixture were added to obtain a metal:3 ratio of 1:2, generating networks P1•Fe and P1•Cu, respectively. The solutions were cast into Teflon molds, covered with a glass slide, and allowed to dry slowly under positive nitrogen flow for 24 h. They were then uncovered and allowed to dry under positive nitrogen flow for another 12 h. Finally,

they were transferred to a vacuum chamber for 24 h to ensure complete removal of chloroform and methanol, generating films F1•Fe and F1•Cu.

To make the uncrosslinked film F1, P1 was dissolved at approximately 10 weight percent in 95:5 chloroform:methanol and cast into a Teflon mold, covered with a glass slide, and allowed to dry slowly under positive nitrogen flow for 24 h. It was then uncovered and allowed to dry under positive nitrogen flow for another 12 h. Finally, it was transferred to a vacuum chamber for 24 h to ensure complete removal of chloroform and methanol, generating film F1.

3.8.6 Uniaxial Tensile Testing and Stress Relaxation Testing

Tensile testing was performed on films that were approximately 1.0 mm in width by 3.0 mm in height by 0.3 mm in thickness. Uniaxial tensile tests of these film were carried out at the nominal strain rate of 10%/s. The nominal strain (ε) was measured through the distance between clamps (recorded by DMA instrument), and the nominal stress was calculated as the measured load divided by the original cross-sectional area vertical to the load. Stress relaxation tests were conducted using the same sets of samples. Once clamped onto the instrument, the samples were strained at a strain rate 50%/s up to 50% strain, then held at 50% strain for 500 s while the nominal stress was recorded by the instrument.

4. Rheological Characterization of Coordinatively Crosslinked Organogels

As previously mentioned, there is a platform that has connected single-molecule experiments with gel characterization.[8] The platform P1 described in Chapter 3 of this work was characterized in the elastomeric state and can be extended in the future to single-molecule experiments. In this section, we explore the properties of gels made from P1 and metal coordination.

4.1 Introduction

Noncovalent crosslinks in gels are expected to display more kinetically dynamic behavior than solid elastomers because the solvent allows for easier diffusion of molecules within the network.[87] The solvent also provides the opportunity for loading of the gel solution with small molecules such as catalytic substrates[93] or drug molecules.[94] However, it is unknown whether the same force-mediated behavior should be expected in gels as in the solvent-free environment of solid elastomers crosslinked by organometallic complexes. To address this knowledge gap, we sought to determine whether the same platform reported in Chapter 3 for solid elastomers could be extended to work in organogels. The first challenge was to make self-standing gels, which was found to be more easily done by swelling dry films than by adding metal to crosslink concentrated polymer solutions. The second step was to characterize the gels to determine whether changing the metal identity changes the material properties.

4.2 Results and Discussion

It was assumed that when the solid films were swollen with toluene, the structural similarity observed between the metalated films (described in Chapter 3) would persist. Upon swelling, frequency sweeps were conducted on each material to determine whether the gel moduli were affected by the crosslinking metal identity. Representative rheological frequency sweeps are shown in Figure 28.

Qualitatively, the metal-containing gels P1●Cu and P1●Fe were self-standing materials while the polymer solution P1 was a viscous liquid. In addition, the storage and loss modulus curves of the metal-containing gels P1●Cu and P1●Fe differ significantly from those of the uncrosslinked polymer solution of P1. Both the loss and storage moduli of the metal-containing films are also at least an order of magnitude higher than those of the uncrosslinked film at all frequencies (Figure 31), indicating that the metal ions and chelating units are indeed crosslinking the polymer to create the gels.

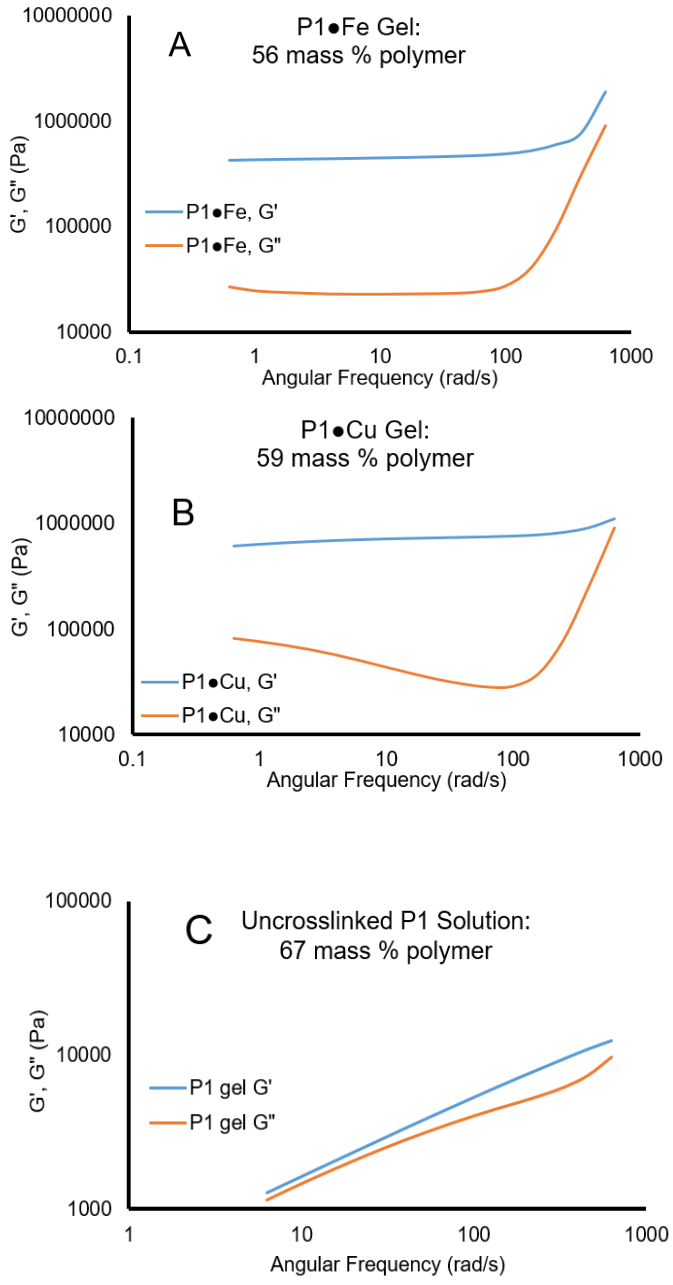

Figure 31. Rheological frequency sweeps of polymer gels in toluene. Storage moduli *G′* and loss moduli *G″* of (A) gel P1●Cu at 59 mass% polymer, (B) gel P1●Fe at 56 mass% polymer, and (C) un-crosslinked solution P1 at 67 mass% polymer. Sweeps for P1●Cu and P1●Fe were performed at 23 °C in air at 5% amplitude with 8mm parallel plate geometry. Sweep for P1 solution was performed at 23 °C in air at 5 % amplitude with 25 mm cone and plate geometry.

As expected, the storage moduli of the crosslinked gels P1●Cu and P1●Fe decrease as more solvent is added (Figure 32). When *G′* versus volume fraction polymer is plotted at the approximate plateau modulus (at the frequency 99.6 rad/s), the copper-crosslinked gels P1●Cu decrease in modulus slightly more quickly with decreasing volume fraction polymer than the iron crosslinked gels P1●Fe. The volume fraction was calculated using the mass of the gel, the mass of polymer originally used, and the densities of the majority monomer *cis*-cycloocetene and the solvent toluene.

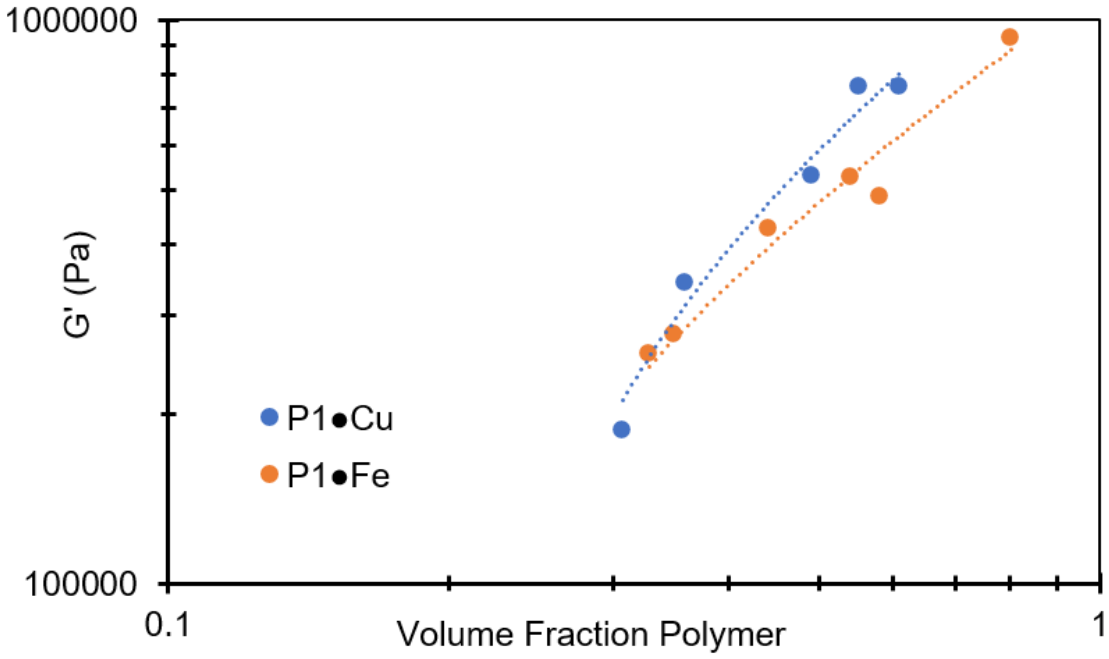

Figure 32. For P1●Cu and P1●Fe, the plateau modulus (*G′* at 99.6 rad/s) is plotted as a function of the volume fraction of polymer.

The plateau region for *G′* becomes increasingly narrow as the volume fraction of polymer decreased for P1●Cu (Figure 33). This behavior essentially brings the crosslinked gels closer to the behavior of the uncrosslinked P1 solution, for which no

plateau modulus was reached and across entire frequency regime tested. We attribute this data to more quickly relaxing Cu(II) crosslinks compared to Fe(II) crosslinks, and to faster relaxation in more dilute conditions (decreased polymer volume fraction). At low volume fractions of polymer, when the ligand is essentially more dilute, the copper likely transitions to a mixture of 1:1 and 2:1 binding with the ligand, lowering the number of effective crosslinks. A decrease in number of crosslinks would explain why the storage modulus of the Cu(II) gels decreases faster than that of the Fe(II) gels. This is an important piece of information because, if some of the Cu(II) crosslinks are dissociating to 1:1 complexes, then the overall number of active strands due to crosslinks is changing in comparison to the Fe(II) gel.

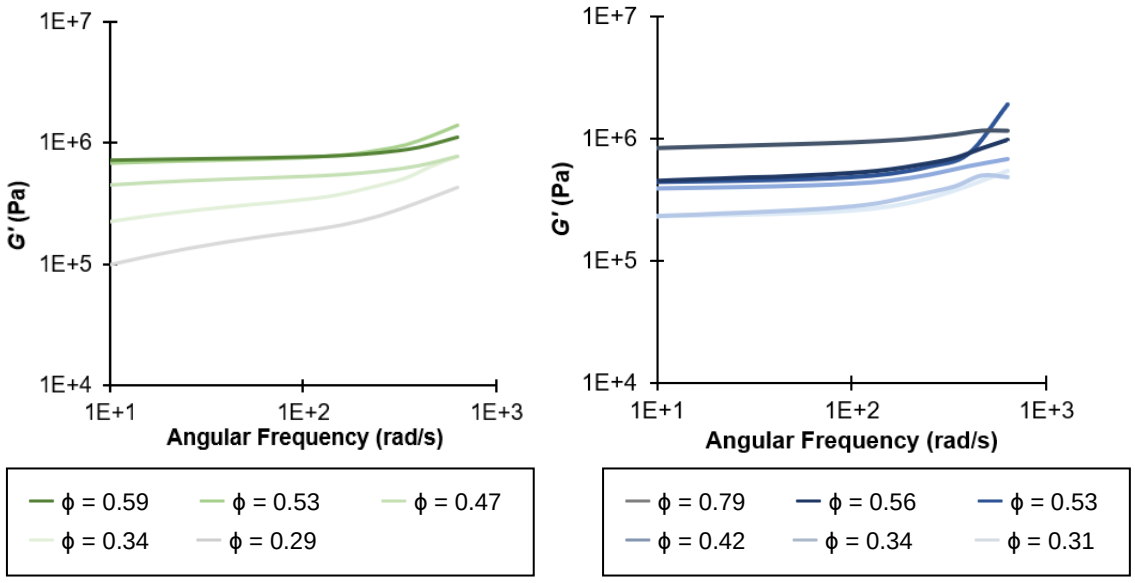

Figure 33. G′ of P1●Cu and P1●Fe, showing increased frequency dependency with decreasing polymer content for P1●Cu. ϕ is the mass percent polymer of the sample. Frequency sweeps were conducted at 5% amplitude in air at 23 °C with 8 mm parallel plate geometry.

So, preliminary rheological characterization suggests that, while these gels can be used to determine the effect of the metal center on material properties at high polymer contents, in dilute conditions, part of the change in material properties will be due to change in the number of crosslinks. This platform is most applicable to the goal of determining force-mediated network behavior in high-polymer-content gels. At lower polymer concentrations, the solution-state kinetics of Cu(II)-ligand dissociation become more important and therefore must be explored further. One way to explore the kinetics of ligand dissociation is by functionalizing the ligand with a fluorescent marker that is quenched upon metal association. It is difficult to determine kinetic constants with the current system and UV-visible spectroscopy because of the overlap in the UV spectra of the metal complex and the free ligand. Fluorescence spectroscopy could provide a more quantitative picture of the concentration dependence of Cu(II) versus Fe(II) binding, which could in turn be correlated with gel polymer content.

Relaxation of the copper complexes is also observed in the loss modulus data; the lower the volume fraction of polymer, higher the frequency at which *G*" peaks (Figure 34). That is, when there is more solvent in the environment, the copper complexes relax faster. It is possible that this faster relaxation is due to increasing dissociation constant with decreasing concentration. The iron complexes do not exhibit relaxation in the frequency range explored, supporting the hypothesis that they are more kinetically stable than the copper complexes.

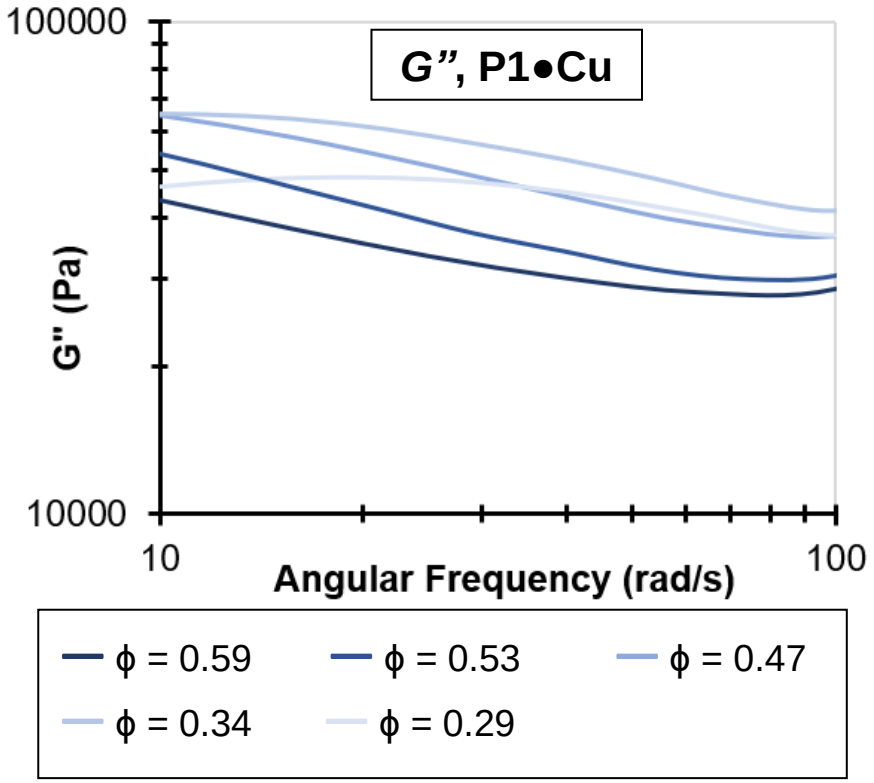

Figure 34. *G”* curves focusing on the relaxation of the crosslinks from frequency sweeps of the copper-crosslinked gels P1●Cu. ϕ is the mass percent polymer of the sample. Frequency sweeps were conducted at 5% amplitude in air at 23 °C with 8 mm parallel plate geometry.

These gel studies have revealed first and foremost that in a material context, copper binds at least partially in a 2:1 stoichiometry with the ligand at all volume fractions tested. Secondly, the material properties of the gels, namely the relaxation timescales, can be tuned by changing the metal identity even at high polymer content where 2:1 ligand:metal binding dominates for both metal species.

4.3 Conclusion

We have demonstrated that the polymeric platform used to create homogenous elastomers can be extended to create self-standing gels of various polymer content. Furthermore, we have demonstrated that the relaxation time of these gels can be tuned by manipulating the metal identity and the gel polymer content. Further tuning of the relaxation time could be achieved with characterization of additional metal species. It would also be interesting to create gels with more than one metal species, for example 50% Cu(II) and 50% Fe(II), to achieve materials with multiple relaxations. This does not require high polymer content and could afford gels with desirable mechanical properties, such as being self-standing like low-polymer-content Fe(II)-crosslinked gels, at the same time exhibiting functionalities such as self-healing based on fast-relaxing crosslinks like the Cu(II) complexes. One could even imagine the use of such a gel to release metal ions into the surrounding environment. If a Cu(II) gel was made, then put at the interface between a dilute Fe(II) solution and a metal-free solution, the Fe(II) would slowly exchange with the Cu(II), releasing Cu(II) into the metal-free solution. Since the relaxation time of the Fe(II) crosslinks, once formed, is very slow, the Fe(II) network would release few Fe(II) ions into the initially metal-free solution. Such a system could be used to control the timescale of copper release into an environment, for example to achieve antimicrobial functionality.[95,96] Alternatively, depending on the relative relaxation times of toxic metals such as chromium, the quickly-relaxing Cu(II)

crosslinked gel could act as a filter, releasing environmentally-benign Cu(II) and capturing toxic metals with slow relaxation times (Figure 35). If the toxic metal had a slow enough relaxation time, the filter could be removed before any was re-released into the environment.

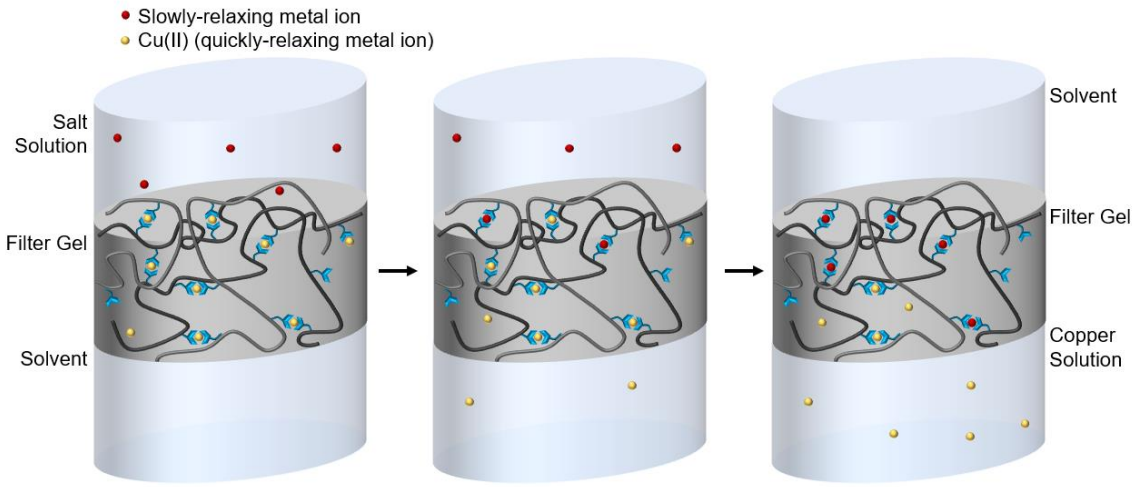

Figure 35. Schematic representation of a filter system exploiting the quickly-relaxing Cu(II)-crosslinked gel discussed in this work.

4.4 Experimental

4.4.1 General Considerations

The monomers and polymer P1 were synthesized as described in Chapter 3. Anhydrous toluene was used as received from VWR. All rheological characterization was conducted on an Anton Paar MCR 702 rheometer.

4.4.2 Gel Preparation

Films F1•Fe and F1•Cu were swollen with toluene to make gels for rheological characterization. Toluene was used for its high boiling point, which facilitated rheological testing, as well as to enable better comparison to the solution state UV-Vis studies in 95:5 v/v toluene: methanol. Each film's mass was recorded using a microbalance, then toluene was added dropwise to the top of the film. The film and toluene were allowed to equilibrate for one h, at which time the mass was recorded again to determine the relative content of solvent and network. The gel was then immediately subjected to a rheological frequency sweep at 5% amplitude using 8 mm parallel plate geometry, after which more solvent was added and the procedure was repeated. This process yielded frequency sweeps for gels with a range of polymer content.

Conclusion

As the mechanochemistry of organometallic complexes has yet to be systematically studied in the context of molecule-to-material relationships, and as it has potential for useful application in functional materials, the aims of this work were: (i) to explore prior work related to the molecular-level activation of metal-ligand bonds by mechanical force, and (ii) to design and characterize a polymeric network crosslinked by metal-ligand complexes that can be used as a modular platform for systematic investigation of the effects of mechanical force on metal-ligand bonding. Regarding (i), there is much valuable relevant work which sets the stage for a more systematic study of the effects of metal identity and ligand sphere sterics and electronics. Regarding (ii), we have demonstrated the use of metal-ligand complexes as modular crosslinks in a polymer network and designed them with careful consideration of variables affecting mechanical properties of the materials outside of the crosslinking metal identity, namely aggregation of the crosslinks and the density of active strands. Changing the metal identity from Fe(II) to Cu(II) does not appreciably change the aggregation behavior or active strand density observed in crosslinked films of the polymer P1, but it was clearly demonstrated that this change in metal identity did significantly alter the extensibility and tearing energy of the films. For the copper-crosslinked films, the extensibility was three times that of the iron-crosslinked films, and the tearing energy was approximately twice that of the iron-crosslinked films. We tentatively attribute this behavior to the

faster relaxation of the Cu(II) crosslinks, which allows the dissipation of energy without breaking backbone carbon-carbon bonds. Due to the reversible nature of the metal-ligand bonds, the crosslinks can reform on the timescale of tensile testing and fracture testing, allowing the material to flow but also reform its crosslinks before carbon-carbon bond rupture leads to film rupture.

The same polymer system tested in the dry elastomer state was also investigated rheologically as toluene organogels. This investigation lent support to the hypothesis that the Cu(II) complexes are more susceptible to the dissociation of one ligand because as the gels' polymer concentration decreased, the storage modulus because increasingly frequency dependent, indicating a decrease in the number of active crosslinks despite the same number of chelating repeat units in the polymer. The gel studies also highlighted the possibilities associated with multiple relaxation times in multi-metal gels, including self-healing materials.

Looking to the future, these polymers can be used with little or no synthetic modification for single molecule force spectroscopy and characterization by ultrasonication. While this work describes the material aspect of the molecule-to-material relationship in this system, it also provides a direct avenue for investigation of the molecular aspect. Furthermore, we have designed the ligand-bearing repeat units to be synthetically accessible with a range of substituents to afford facile, systematic alteration of the electronics and sterics of the ligand sphere. This adds another handle to

manipulate the behavior under force of these complexes, outside the metal identity manipulation demonstrated in this work.

An additional application of this ligand that could be useful in further defining the molecule-to-material relationship of this system is a covalently-bridged dimer of ligands to form a nonscissile loop-like mechanophore. Such a structure would provide an alternative means to obtain single-molecule force spectroscopy characterization of this type of system and would enable the release of stored length from the rupture of a metal-ligand bond. A schematic of such a structure is shown in Scheme 8, and the synthetic details of intermediates in the progress towards this loop ligand are contained in the Appendix of this dissertation.

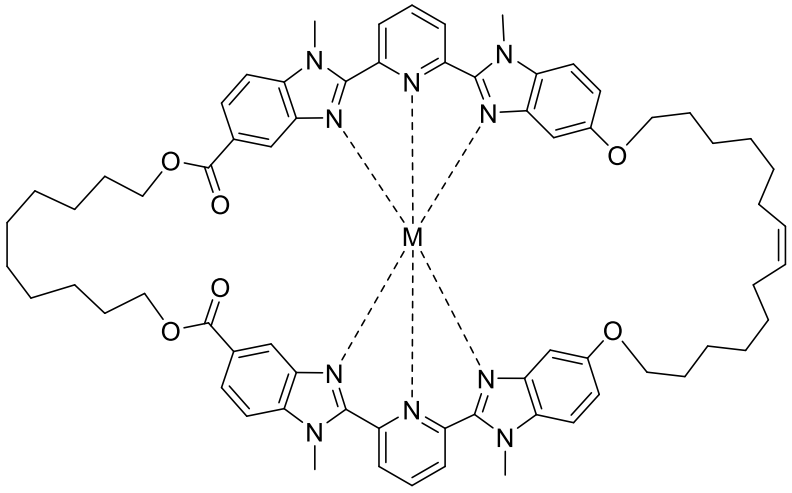

Scheme 8. Schematic of suggested macrocyclic monomer amenable to ring-opening metathesis polymerization.

Appendix

Synthesis of Intermediates Toward Loop Ligand

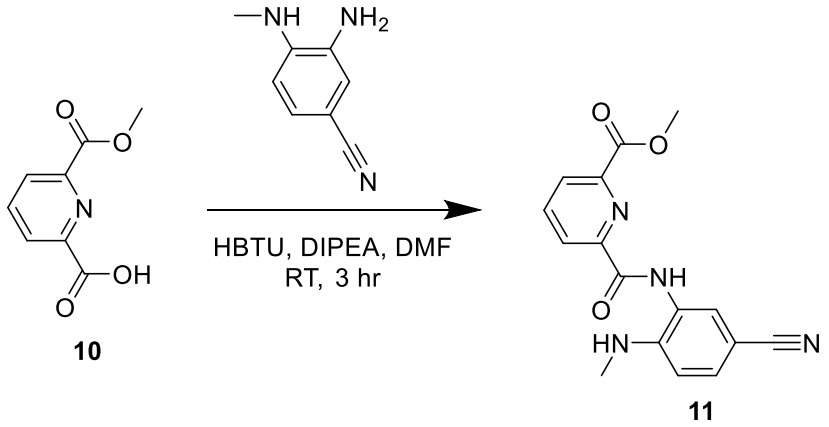

Scheme 9. Synthesis of 11.

Preparation of 11 (methyl 6-((5-cyano-2-(methylamino)phenyl)carbamoyl)picolinate): 453 mg (2.50 mmol, 1.0 eq) of 10, 368 mg (2.50 mmol, 1.0 eq), and 948 mg (2.50 mmol, 1.0 eq) HBTU were added to a flame-dried 40 mL scintillation vial with a septum cap and stir bar. A needle was used to evacuate and refill the vial with a nitrogen atmosphere three times. 5.0 mL anhydrous DMF was added via syringe to the and it was stirred to disperse the solids. 1.0 mL DIPEA was added to the stirring reaction mixture in one portion via syringe, immediately initiating a change from cloudy brown solution to clear, reddish pink solution. Within 15 minutes, fluffy light pink precipitate began to form. The mixture was stirred overnight, then opened to air and diluted with 15 mL cold, deionized water. This caused the precipitation of a very light pink, fluffy solid, which was filtered out of the solution and

washed three times with 15 mL each of cold, deionized water. The resulting light pink powdery solid was dried in vacuo to yield 563 mg (72.6%) and was used without further purification. ^{1}H NMR (500 MHz, DMSO [D_6]) δ = 9.77 (s, 1H), 8.27 (m, 3H), 7.57 (d, 1H), 7.54 (dd, 1H), 6.71 (d, 1H), 6.33 (s(br), 1H), 3.95 (s, 3H), 2.76 (s, 3H). ^{13}C NMR (500 MHz, DMSO [D_6]) δ = 165.18, 163.40, 150.73, 149.06, 146.99, 139.90, 132.60, 130.97, 127.86, 126.13, 122.79, 120.59, 110.69, 95.83, 53.22, 29.79. MS (ESI$^+$): *m*/*z* 311.1 (MH^+).

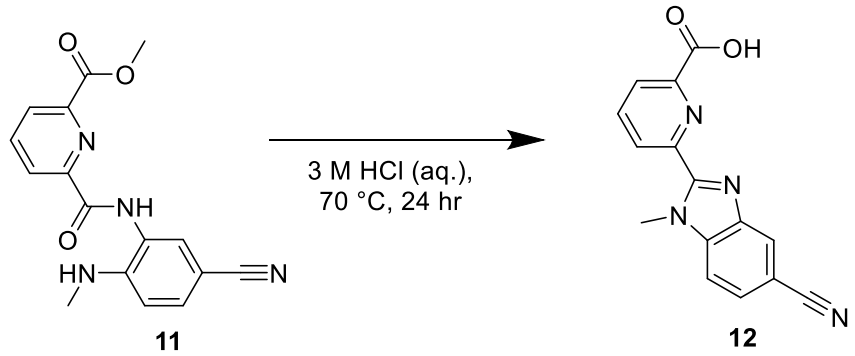

Scheme 10. Synthesis of 12.

Preparation of 12 (6-(5-cyano-1-methyl-1H-benzo[d]imidazol-2-yl)picolinic acid): 310 mg (1.0 mmol, 1eq.) of the solid 11 was dispersed in 14.0 mL of 3.0 M hydrochloric acid (aq.) in a 25 mL round bottom flask with a stirbar and a small vigreaux condenser. The mixture of pink solid and pink liquid was heated to 70 C and stirred 18 hours. The mixture was cooled to room temperature and 5.0 M sodium hydroxide solution (aq.) was added dropwise until the pH was between 5 and 6. The solid was filtered off and washed three times with 10 mL cold, deionized water. Drying in vacuo resulted in 266 mg (95.7%) of off-white solid that was used without further purification. ^{1}H NMR (500

MHz, DMSO [D_6]) δ = 13.33 (s(br), 1H), 8.545 (dd, 1H), 8.295 (d, 1H), 8.24-8.16 (m, 2H), 7.89 (d, 1H), 7.73 (dd, 1H), 4.38 (s, 3H). ^{13}C NMR (500 MHz, DMSO [D_6]) δ = 8.53 (dd, 1H), 8.285 (d, 1H), 8.211 (t, 1H), 8.177 (dd, 1H), 7.886 (d, 1H), 7.731 (dd, 1H), 4.379 (s, 3H). MS (ESI$^+$): *m*/*z* 279.1 (MH^+).

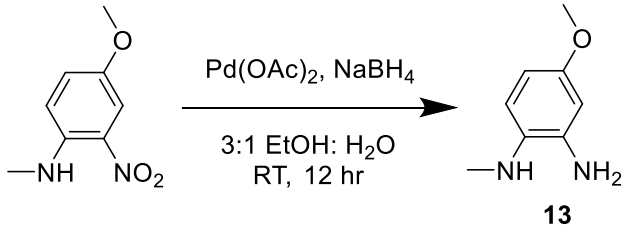

13

Scheme 11. Synthesis of 13.

Preparation of 13 (4-methoxy-N1-methylbenzene-1,2-diamine): 911 mg (5.0 mmol, 1.0 eq) of N-methyl-4-methoxy-2-nitroaniline and 378 mg (10.0 mmol, 2.0 eq) sodium borohydride was added to a 250 mL round bottom flask with a stirbar and closed with a rubber septum. The flask was evacuated and refilled three times with a nitrogen atmosphere. In a separate flask, 60.0 mL ethanol and 20.0 mL deionized water were mixed and sparged for 20 minutes with nitrogen. A cannula was used to transfer the solvent mixture from its flask to the reaction flask containing the nitroaniline. Meanwhile, 11.2 mg (0.050 mmol, 0.010 eq) palladium(II) acetate was added to a flame-dried 7 mL scintillation vial with a septum cap. 1.0 mL of ethanol was added to this vial to dissolve the catalyst. A syringe was used to transfer the catalyst solution from the vial to the vigorously stirring reaction mixture in one portion. Upon its addition, the color of the reaction mixture changed immediately from orange to red, and continued to darken

to brown over time. The reaction was stirred at room temperature for 18 hours, after which TLC in ethyl acetate showed no remaining starting material. 50 mL brine was added and the mixture was extracted three times with 50 mL each of ethyl acetate. The combined organic layers were washed with 50 mL deionized water once, then dried with magnesium sulfate, filtered, and dried in vacuo to yield a dark brown, oily solid. A silica plug using ethyl acetate as the eluent was run. The resulting 498 mg (63.8%) of dark brown, sticky solid was kept under nitrogen atmosphere and used without further purification. ^{1}H NMR (500 MHz, DMSO [D_6]) δ = 6.29 (d, 1H), 6.20 (s, 1H), 6.085 (dd, 2H), 4.25 (s(br), 2H), 4.16 (s(br), 1H), 3.58 (s, 3H), 2.64 (s, 3H). ^{13}C NMR (500 MHz, DMSO [D_6]) δ = 151.92, 136.91, 131.35, 109.99, 101.14, 101.04, 54.87, 30.91. MS (ESI$^+$): *m*/*z* 153.1 (MH^+).

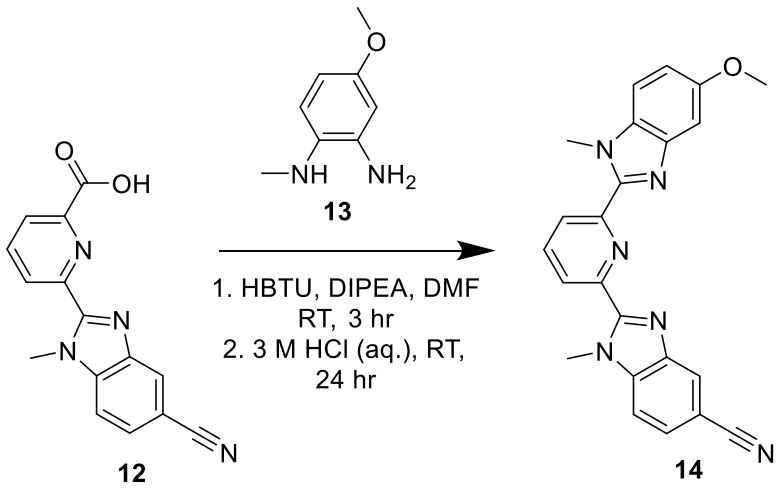

Scheme 12. Synthesis of 14.

Preparation of 14 (2-(6-(5-methoxy-1-methyl-1H-benzo[d]imidazol-2-yl)pyridin-2-yl)-1-methyl-1H-benzo[d]imidazole-5-carbonitrile): A flame-dried 250 mL round

bottom flask with a stirbar and septum was charged with 1.09 g (3.90 mmol, 1.0 eq) 12, 594 mg (3.90 mmol, 1.0 eq) 13, and 1.48 g (1.0 mmol, 1.0 eq) HBTU. The sealed flask was evacuated and refilled with nitrogen atmosphere three times. 10.0 mL anhydrous DMF was added to the vial via syringe. With vigorous stirring, 2.0 mL DIPEA was added to the reaction mixture via syringe. The mixture was stirred at 50 °C for 12 hours. After 12 hours, 10.0 mL 3.0 M hydrochloric acid (aq) was added to the vial via syringe, which caused an immediate change in color from light pink to bright magenta. The mixture was stirred at room temperature overnight. To obtain the product, the pH was adjusted to 7 with 5.0 M sodium hydroxide solution (aq), which caused a light brown solid to precipitate. The solid was filtered off and washed three times with 10 mL cold, deionized water, then dried to yield 1.35 g (87.8%) light brown solid that was used without further purification. ^{1}H NMR (500 MHz, DMSO [D_6]) δ = 8.426 (d, 1H), 8.390 (d, 1H), 8.340 (s, 1H), 8.231 (t, 1H), 7.929 (d, 1H), 7.761 (dd, 1H), 7.589 (d, 1H), 7.277 (d, 1H),7.003 (dd, 1H), 4.287 (s, 3H), 4.231 (s, 3H), 3.828 (s, 3H). MS (ESI^+): *m*/*z* 395.3 (MH^+).

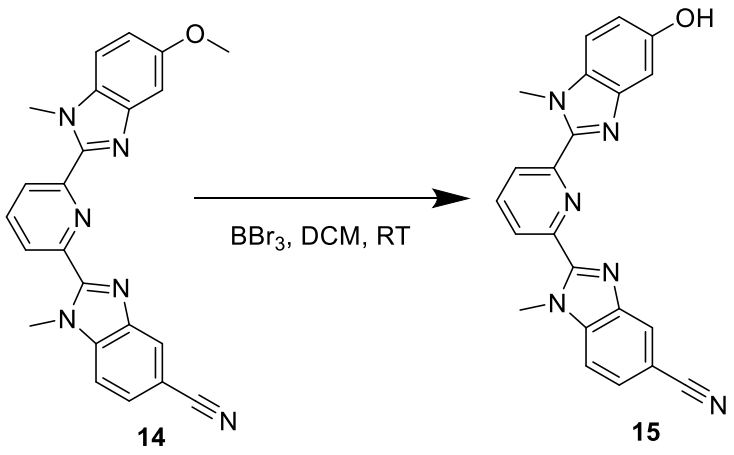

Scheme 13. Synthesis of 15.

Preparation of 15 (2-(6-(5-hydroxy-1-methyl-1H-benzo[d]imidazol-2-yl)pyridin-2-yl)-1-methyl-1H-benzo[d]imidazole-5-carbonitrile): A flame-dried 2-neck 50 mL round bottom flask was fitted with a reflux condenser and then was charged with 1.35 g (3.42 mmol, 1.0 eq) of 14. Septa were used to close the system, and it was then evacuated and refilled with nitrogen three times. 10.0 mL anhydrous dichloromethane was added to the vial via syringe to disperse the solid **5**. 10.3 mL 1.0 M (10.3 mmol, 3.0 eq) boron tribromide solution in dichloromethane (commercial, Sigma Aldrich) was added slowly to the stirring reaction vial in one portion via syringe. The cloudy light brown solution turned cloudy mauve. After stirring for 12 hours at 40 °C, the solution was opened to air and 20.0 mL water was added. The mixture was poured into a beaker containing 50 mL di water. The pH was adjusted to 7.0 with 10 M NaOH (aq) solution. The brown precipitate was then filtered from the mixture, washed four times with 20 mL di water, and dried. This yielded 951 mg (73.2%) of a light brown solid. ^{1}H NMR (500 MHz,

DMSO [D_6]) δ = 9.22 (s, 1H), 8.415 (dd, 1H), 8.395 (dd, 1H), 8.330 (d, 1H), 8.212 (t, 1H), 7.916 (d, 1H), 7.756 (dd, 1H), 7.475 (d, 1H), 7.057 (d, 1H), 6.875 (d, 1H), 4.288 (s, 3H), 4.194 (s, 3H). δ. MS (ESI^+): *m*/*z* 381.3 (MH^+).

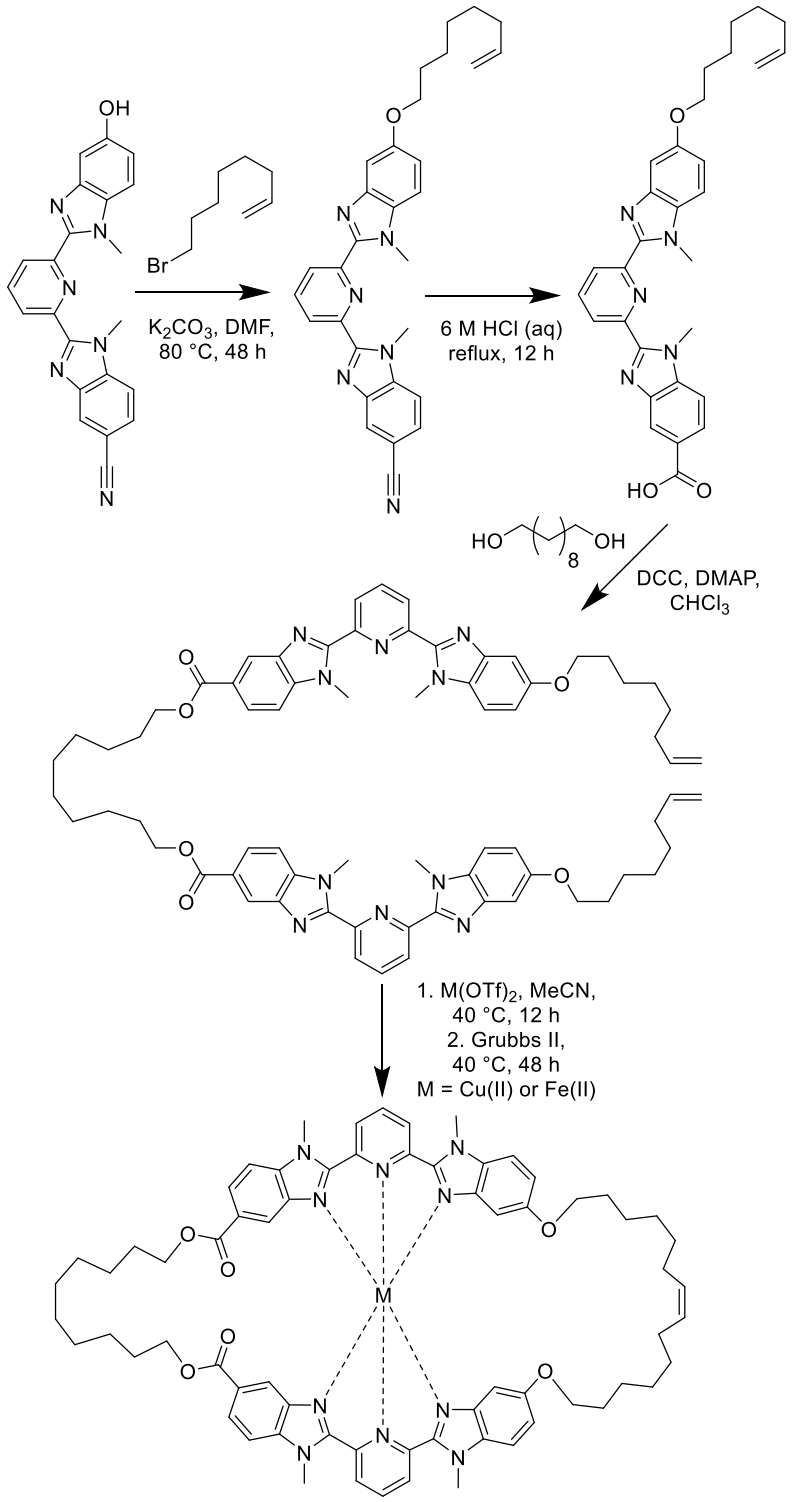

Scheme 14. Suggested route for remaining synthetic steps to loop ligand.

Fitting Information for SAXS Data

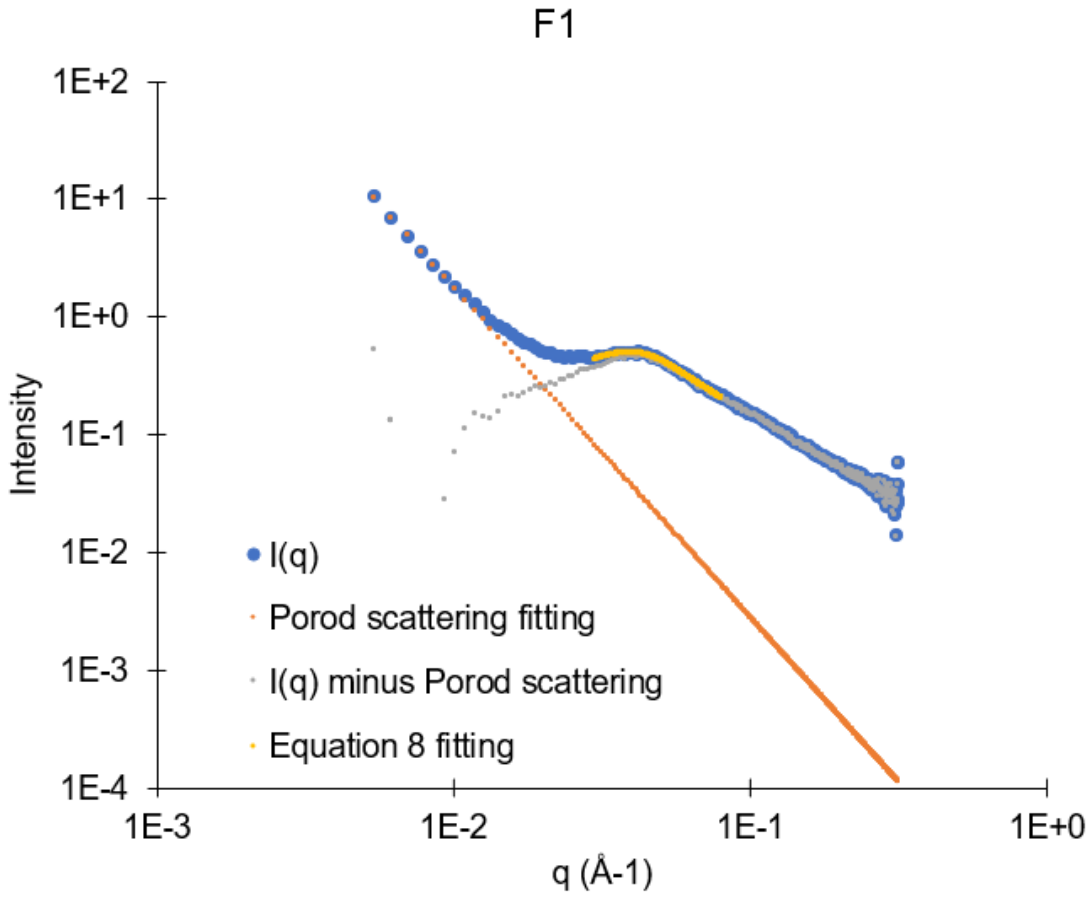

Figure 36. Fitting of SAXS data for F1. Blue points are the raw intensity data. Yellow points are the fitting of Equation 8 to the raw data between q = 0.02 and 0.06. Orange points are the fitting of the data between q = 0.00541 and 0.01, representing Porod law scattering. Gray points are this fitting from Porod's law subtracted from the raw data. Origin was used to plot and fit all data.

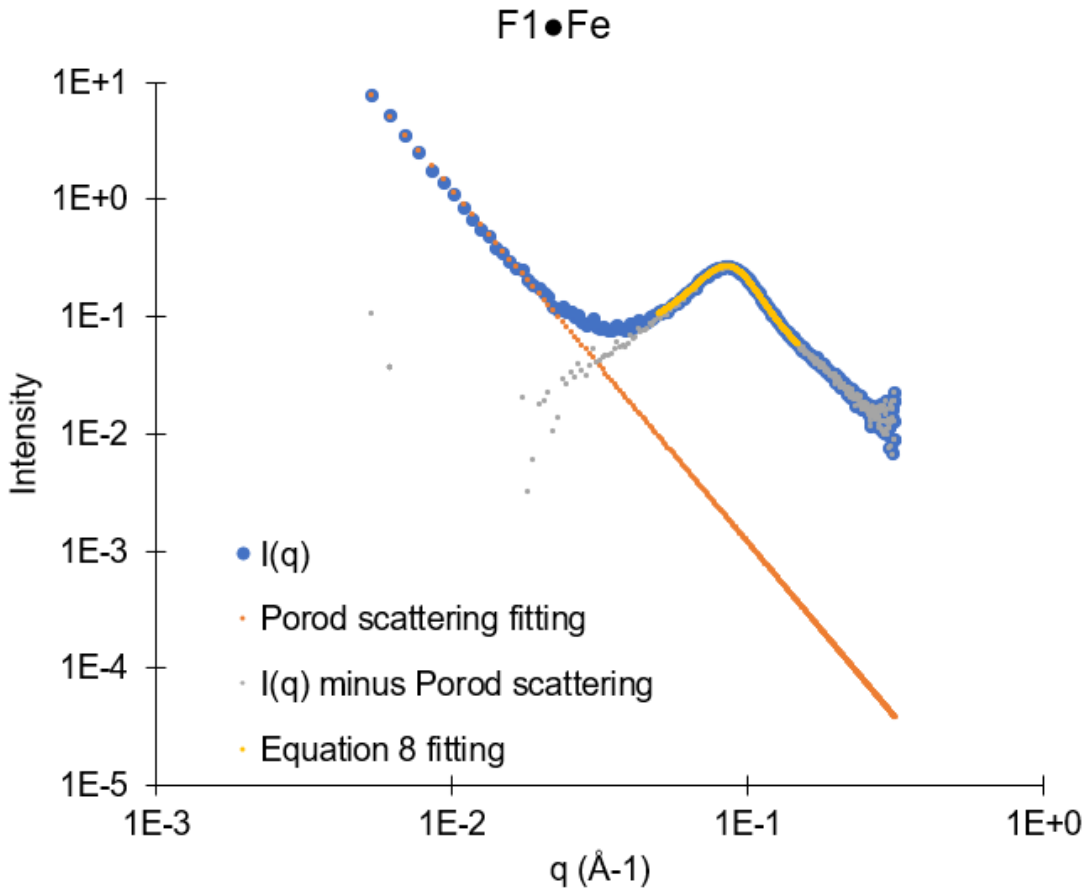

Figure 37. Fitting of SAXS data for F1●Fe. Blue points are the raw intensity data. Yellow points are the fitting of Equation 8 to the raw data between q = 0.05 and 0.15. Orange points are the fitting of the data between q = 0.00541 and 0.01, representing Porod law scattering. Gray points are this fitting from Porod's law subtracted from the raw data. Origin was used to plot and fit all data.

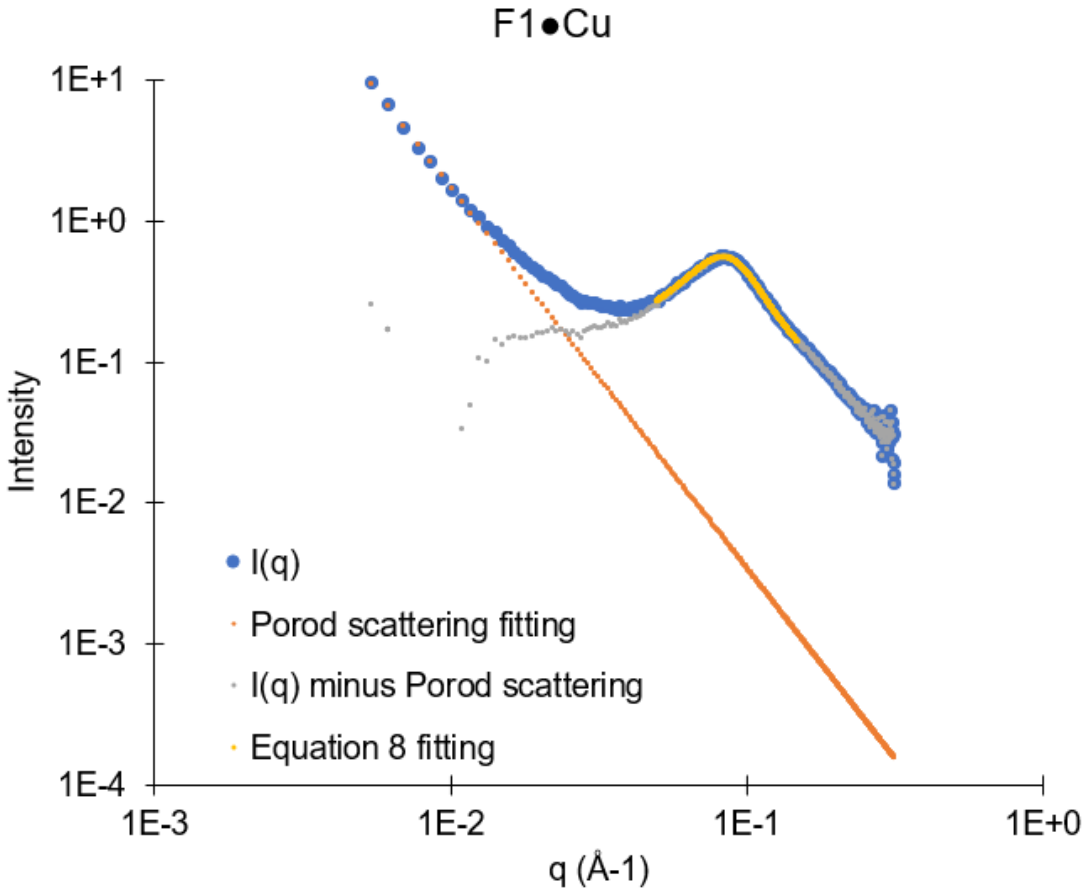

Figure 38. Fitting of SAXS data for F1●Cu. Blue points are the raw intensity data. Yellow points are the fitting of Equation 8 to the raw data between q = 0.05 and 0.15. Orange points are the fitting of the data between q = 0.00541 and 0.01, representing Porod law scattering. Gray points are this fitting from Porod's law subtracted from the raw data. Origin was used to plot and fit all data.

Table 5. Fitting parameters for Equation 8 for raw SAXS data *I(q)*. F1●Fe and F1●Cu were fit between *q* = 0.05 and 0.15. F1 was fit between *q* = 0.02 and 0.06.

	F1●Fe before correction by Porod law		F1●Cu before correction by Porod law		F1 before correction by Porod law	
Parameter	value	+/-	value	+/-	value	+/-
A	1.32E-05	1.25E-07	3.13E-05	2.56E-07	6.86E-06	1.03E-07
B	3.87E-06	2.25E-08	3.00E-06	1.94E-08	1.46E-07	5.07E-09
R_a (Å)	16.73	0.09	16.53	0.07	26.95	0.20
R_c (Å)	32.05	0.05	32.23	0.06	65.29	0.39

Table 6. Fitting parameters for Equation 8 for raw SAXS data minus the value of I_{Porod} for Porod law scattering at each *q*, *I'(q)*. F1●Fe and F1●Cu were fit between *q* = 0.05 and 0.15. F1 was fit between *q* = 0.02 and 0.06.

	F1●Fe after correction by Porod law		F1●Cu after correction by Porod law		F1 after correction by Porod law	
Parameter	value	+/-	value	+/-	value	+/-
A	1.34E-05	1.51E-07	3.18E-05	2.65E-07	7.38E-06	7.59E-07
B	3.98E-06	2.51E-08	3.14E-06	2.13E-08	1.95E-07	8.91E-09
R_a (Å)	16.42	0.10	16.18	0.08	25.19	1.06
R_c (Å)	32.12	0.05	32.32	0.05	64.02	0.77

Table 7. Fitting parameters K and a for Porod's law (Equation 29) for raw SAXS data between *q* = 0.00514 and 0.01.

	F1●Fe	F1●Cu	F1
K	1.2E-06	7.0E-06	4.5E-06
a	3.0	2.7	2.8

A Porod law can be used to describe the differences in density between areas in a material.[97] To determine whether scattering resulting from differing areas of density in

the material, indicated by the trend of increasing I at low values of q in the SAXS data, affected the fitting of Equation 8 to the SAXS data, the data between q = 00.514 and 0.01 was fit with a modified Porod law[97]

$$I = \frac{K}{q^{\alpha}} \qquad \text{Equation 29}$$

where I is the scattering intensity, K is the Porod scaling factor, and α is the Porod exponent, which is related to the interface between the polymer-rich and polymer-lean regions in the swollen networks. α is 4 for smooth surfaces, but higher and lower values indicate a surface density gradient and a rough surface, respectively.

The resulting fitting parameters from the modified Porod law were used to find I_{Porod} at each value of q. Next, I_{Porod} was subtracted from each value of I in the raw dataset to get $I'(q)$. Finally, the new dataset $I'(q)$ was again fit with Equation 8, and the resulting fitting parameters R_a, R_C, a, and b were compared to the original fitting parameters for Equation 8 with the raw data. As can be seen by comparing Tables 5 and 6, the subtraction of Porod's law scattering does not significantly alter the fitting parameters for Equation 8, and therefore does not detract from the fact that the size and spacing of the small aggregates observed in F1●Fe and F1●Cu are nearly identical to each other.

References

(1) Rubinstein, M., 1956 December 20-; Colby, R. H. *Polymer Physics*; Oxford ; New York : Oxford University Press, 2003.: Oxford, 2003.

(2) Balkenende, D. W. R.; Coulibaly, S.; Balog, S.; Simon, Y. C.; Fiore, G. L.; Weder, C. Mechanochemistry with Metallosupramolecular Polymers. *J. Am. Chem. Soc.* **2014**, *136* (29), 10493–10498. https://doi.org/10.1021/ja5051633.

(3) Golkaram, M.; Loos, K. A Critical Approach to Polymer Dynamics in Supramolecular Polymers. *Macromolecules* **2019**. https://doi.org/10.1021/acs.macromol.9b02085.

(4) Yuan, J.; Zhang, H.; Hong, G.; Chen, Y.; Chen, G.; Xu, Y.; Weng, W. Using Metal–Ligand Interactions to Access Biomimetic Supramolecular Polymers with Adaptive and Superb Mechanical Properties. *J. Mater. Chem. B* **2013**, *1* (37), 4809–4818. https://doi.org/10.1039/C3TB20647E.

(5) Mozhdehi, D.; Neal, J. A.; Grindy, S. C.; Cordeau, Y.; Ayala, S.; Holten-Andersen, N.; Guan, Z. Tuning Dynamic Mechanical Response in Metallopolymer Networks through Simultaneous Control of Structural and Temporal Properties of the Networks. *Macromolecules* **2016**, *49* (17), 6310–6321. https://doi.org/10.1021/acs.macromol.6b01626.

(6) Vidavsky, Y.; Buche, M. R.; Sparrow, Z. M.; Zhang, X.; Yang, S. J.; DiStasio, R. A.; Silberstein, M. N. Tuning the Mechanical Properties of Metallopolymers via Ligand Interactions: A Combined Experimental and Theoretical Study. *Macromolecules* **2020**, *53* (6), 2021–2030. https://doi.org/10.1021/acs.macromol.9b02756.

(7) Sha, Y.; Zhang, Y.; Xu, E.; McAlister, C. W.; Zhu, T.; Craig, S. L.; Tang, C. Generalizing Metallocene Mechanochemistry to Ruthenocene Mechanophores. *Chem. Sci.* **2019**, *10* (19), 4959–4965. https://doi.org/10.1039/C9SC01347D.

(8) Kersey, F. R.; Loveless, D. M.; Craig, S. L. A Hybrid Polymer Gel with Controlled Rates of Cross-Link Rupture and Self-Repair. *J. R. Soc. Interface* **2007**, *4* (13), 373–380. https://doi.org/10.1098/rsif.2006.0187.

(9) Musgrave, R. A.; Russell, A. D.; Hayward, D. W.; Whittell, G. R.; Lawrence, P. G.; Gates, P. J.; Green, J. C.; Manners, I. Main-Chain Metallopolymers at the Static–Dynamic Boundary Based on Nickelocene. *Nat. Chem.* **2017**, *9* (8), 743–750. https://doi.org/10.1038/nchem.2743.

(10) Yount, W. C.; Loveless, D. M.; Craig, S. L. Small-Molecule Dynamics and Mechanisms Underlying the Macroscopic Mechanical Properties of Coordinatively Cross-Linked Polymer Networks. *J. Am. Chem. Soc.* **2005**, *127* (41), 14488–14496. https://doi.org/10.1021/ja054298a.

(11) Kumpfer, J. R.; Wie, J. J.; Swanson, J. P.; Beyer, F. L.; Mackay, M. E.; Rowan, S. J. Influence of Metal Ion and Polymer Core on the Melt Rheology of Metallosupramolecular Films. *Macromolecules* **2012**, *45* (1), 473–480. https://doi.org/10.1021/ma201659d.

(12) Jakobs, R. T. M.; Sijbesma, R. P. Mechanical Activation of a Latent Olefin Metathesis Catalyst and Persistence of Its Active Species in ROMP. *Organometallics* **2012**, *31* (6), 2476–2481. https://doi.org/10.1021/om300161z.

(13) Rowan, S. J.; Beck, J. B. Metal–Ligand Induced Supramolecular Polymerization: A Route to Responsive Materials. *Faraday Discuss.* **2005**, *128* (0), 43–53. https://doi.org/10.1039/B403135K.

(14) Burnworth, M.; Knapton, D.; Rowan, S. J.; Weder, C. Metallo-Supramolecular Polymerization: A Route to Easy-To-Process Organic/Inorganic Hybrid Materials. *J. Inorg. Organomet. Polym. Mater.* **2007**, *17* (1), 91–103. https://doi.org/10.1007/s10904-006-9075-2.

(15) Razgoniaev, A. O.; Glasstetter, L. M.; Kouznetsova, T. B.; Hall, K. C.; Horst, M.; Craig, S. L.; Franz, K. J. Single-Molecule Activation and Quantification of Mechanically Triggered Palladium–Carbene Bond Dissociation. *J. Am. Chem. Soc.* **2021**, *143* (4), 1784–1789. https://doi.org/10.1021/jacs.0c13219.

(16) Clough, J. M.; Balan, A.; van Daal, T. L. J.; Sijbesma, R. P. Probing Force with Mechanobase-Induced Chemiluminescence. *Angew. Chem. Int. Ed.* **2016**, *55* (4), 1445–1449. https://doi.org/10.1002/anie.201508840.

(17) Chen, Y.; Mellot, G.; Luijk, D. van; Creton, C.; P. Sijbesma, R. Mechanochemical Tools for Polymer Materials. *Chem. Soc. Rev.* **2021**, *50* (6), 4100–4140. https://doi.org/10.1039/D0CS00940G.

(18) Bowser, B. H.; Craig, S. L. Empowering Mechanochemistry with Multi-Mechanophore Polymer Architectures. *Polym. Chem.* **2018**, *9* (26), 3583–3593. https://doi.org/10.1039/C8PY00720A.

(19) Bell, G. I. Models for the Specific Adhesion of Cells to Cells. *Science* **1978**, *200* (4342), 618–627.

(20) Makarov, D. E. Perspective: Mechanochemistry of Biological and Synthetic Molecules. *J. Chem. Phys.* **2016**, *144* (3), 030901. https://doi.org/10.1063/1.4939791.

(21) Lee, B.; Niu, Z.; Wang, J.; Slebodnick, C.; Craig, S. L. Relative Mechanical Strengths of Weak Bonds in Sonochemical Polymer Mechanochemistry. *J. Am. Chem. Soc.* **2015**, *137* (33), 10826–10832. https://doi.org/10.1021/jacs.5b06937.

(22) Brown, C. L.; Bowser, B. H.; Meisner, J.; Kouznetsova, T. B.; Seritan, S.; Martinez, T. J.; Craig, S. L. Substituent Effects in Mechanochemical Allowed and Forbidden Cyclobutene Ring-Opening Reactions. *J. Am. Chem. Soc.* **2021**, *143* (10), 3846–3855. https://doi.org/10.1021/jacs.0c12088.

(23) Sha, Y.; Zhang, Y.; Xu, E.; Wang, Z.; Zhu, T.; Craig, S. L.; Tang, C. Quantitative and Mechanistic Mechanochemistry in Ferrocene Dissociation. *ACS Macro Lett.* **2018**, *7* (10), 1174–1179. https://doi.org/10.1021/acsmacrolett.8b00625.

(24) Gossweiler, G. R.; Kouznetsova, T. B.; Craig, S. L. Force-Rate Characterization of Two Spiropyran-Based Molecular Force Probes. *J. Am. Chem. Soc.* **2015**, *137* (19), 6148–6151. https://doi.org/10.1021/jacs.5b02492.

(25) Zhang, Y.; Wang, Z.; Kouznetsova, T. B.; Sha, Y.; Xu, E.; Shannahan, L.; Fermen-Coker, M.; Lin, Y.; Tang, C.; Craig, S. L. Distal Conformational Locks on Ferrocene Mechanophores Guide Reaction Pathways for Increased Mechanochemical Reactivity. *Nat. Chem.* **2021**, *13* (1), 56–62. https://doi.org/10.1038/s41557-020-00600-2.

(26) Li, Y.; Wen, J.; Qin, M.; Cao, Y.; Ma, H.; Wang, W. Single-Molecule Mechanics of Catechol-Iron Coordination Bonds. *ACS Biomater. Sci. Eng.* **2017**, *3* (6), 979–989. https://doi.org/10.1021/acsbiomaterials.7b00186.

(27) Lee, H.; Scherer, N. F.; Messersmith, P. B. Single-Molecule Mechanics of Mussel Adhesion. *Proc. Natl. Acad. Sci.* **2006**, *103* (35), 12999. https://doi.org/10.1073/pnas.0605552103.

(28) Schmitt, L.; Ludwig, M.; Gaub, H. E.; Tampé, R. A Metal-Chelating Microscopy Tip as a New Toolbox for Single-Molecule Experiments by Atomic Force Microscopy. *Biophys. J.* **2000**, *78* (6), 3275–3285. https://doi.org/10.1016/S0006-3495(00)76863-9.

(29) Cao, Y.; Yoo, T.; Li, H. Single Molecule Force Spectroscopy Reveals Engineered Metal Chelation Is a General Approach to Enhance Mechanical Stability of Proteins. *Proc. Natl. Acad. Sci.* **2008**, *105* (32), 11152–11157. https://doi.org/10.1073/pnas.0803446105.

(30) Zheng, P.; Li, H. Direct Measurements of the Mechanical Stability of Zinc-Thiolate Bonds in Rubredoxin by Single-Molecule Atomic Force Microscopy. *Biophys. J.* **2011**, *101* (6), 1467–1473. https://doi.org/10.1016/j.bpj.2011.08.021.

(31) Zheng, P.; Li, H. Highly Covalent Ferric−Thiolate Bonds Exhibit Surprisingly Low Mechanical Stability. *J. Am. Chem. Soc.* **2011**, *133* (17), 6791–6798. https://doi.org/10.1021/ja200715h.

(32) Hao, X.; Zhu, N.; Gschneidtner, T.; Jonsson, E. Ö.; Zhang, J.; Moth-Poulsen, K.; Wang, H.; Thygesen, K. S.; Jacobsen, K. W.; Ulstrup, J.; Chi, Q. Direct Measurement and Modulation of Single-Molecule Coordinative Bonding Forces in a Transition Metal Complex. *Nat. Commun.* **2013**, *4* (1), 2121. https://doi.org/10.1038/ncomms3121.

(33) Xia, J.; Zuo, J.; Li, H. Single Molecule Force Spectroscopy Reveals That the Oxidation State of Cobalt Ions Plays an Important Role in Enhancing the Mechanical Stability of Proteins. *Nanoscale* **2019**, *11* (42), 19791–19796. https://doi.org/10.1039/C9NR06912G.

(34) Zheng, P.; Chou, C.-C.; Guo, Y.; Wang, Y.; Li, H. Single Molecule Force Spectroscopy Reveals the Molecular Mechanical Anisotropy of the FeS4 Metal Center in Rubredoxin. *J. Am. Chem. Soc.* **2013**, *135* (47), 17783–17792. https://doi.org/10.1021/ja406695g.

(35) Zheng, P.; Takayama, S. J.; Mauk, A. G.; Li, H. Single Molecule Force Spectroscopy Reveals That Iron Is Released from the Active Site of Rubredoxin by a Stochastic

Mechanism. *J. Am. Chem. Soc.* **2013**, *135* (21), 7992–8000. https://doi.org/10.1021/ja402150q.

(36) Yadav, A.; Paul, S.; Venkatramani, R.; Ainavarapu, S. R. K. Differences in the Mechanical Unfolding Pathways of Apo- and Copper-Bound Azurins. *Sci. Rep.* **2018**, *8* (1), 1989. https://doi.org/10.1038/s41598-018-19755-7.

(37) Beedle, A. E. M.; Lezamiz, A.; Stirnemann, G.; Garcia-Manyes, S. The Mechanochemistry of Copper Reports on the Directionality of Unfolding in Model Cupredoxin Proteins. *Nat. Commun.* **2015**, *6* (1), 7894. https://doi.org/10.1038/ncomms8894.

(38) Yuan, G.; Ma, Q.; Wu, T.; Wang, M.; Li, X.; Zuo, J.; Zheng, P. Multistep Protein Unfolding Scenarios from the Rupture of a Complex Metal Cluster Cd3S9. *Sci. Rep.* **2019**, *9* (1), 10518. https://doi.org/10.1038/s41598-019-47004-y.

(39) Kudera, M.; Eschbaumer, C.; Gaub, H. E.; Schubert, U. S. Analysis of Metallo-Supramolecular Systems Using Single-Molecule Force Spectroscopy. *Adv. Funct. Mater.* **2003**, *13* (8), 615–620. https://doi.org/10.1002/adfm.200304359.

(40) Martin K. Beyer. The Mechanical Strength of a Covalent Bond Calculated by Density Functional Theory. *J. Chem. Phys.* **2000**, *112* (17), 7307–7312. https://doi.org/10.1063/1.481330.

(41) Paulusse, J. M. J.; Sijbesma, R. P. Reversible Mechanochemistry of a PdII Coordination Polymer. *Angew. Chem. Int. Ed.* **2004**, *43* (34), 4460–4462. https://doi.org/10.1002/anie.200460040.

(42) Paulusse, J. M. J.; Huijbers, J. P. J.; Sijbesma, R. P. Quantification of Ultrasound-Induced Chain Scission in PdII–Phosphine Coordination Polymers. *Chem. – Eur. J.* **2006**, *12* (18), 4928–4934. https://doi.org/10.1002/chem.200600120.

(43) Paulusse, J. M. J.; Sijbesma, R. P. Selectivity of Mechanochemical Chain Scission in Mixed Palladium(Ii) and Platinum(Ii) Coordination Polymers. *Chem. Commun.* **2008**, No. 37, 4416–4418. https://doi.org/10.1039/B806978F.

(44) Lenhardt, J. M.; Black Ramirez, A. L.; Lee, B.; Kouznetsova, T. B.; Craig, S. L. Mechanistic Insights into the Sonochemical Activation of Multimechanophore Cyclopropanated Polybutadiene Polymers. *Macromolecules* **2015**, *48* (18), 6396–6403. https://doi.org/10.1021/acs.macromol.5b01677.

(45) Wei, K.; Gao, Z.; Liu, H.; Wu, X.; Wang, F.; Xu, H. Mechanical Activation of Platinum–Acetylide Complex for Olefin Hydrosilylation. *ACS Macro Lett.* **2017**, *6* (10), 1146–1150. https://doi.org/10.1021/acsmacrolett.7b00487.

(46) Piermattei, A.; Karthikeyan, S.; Sijbesma, R. P. Activating Catalysts with Mechanical Force. *Nat. Chem.* **2009**, *1* (2), 133–137. https://doi.org/10.1038/nchem.167.

(47) Karthikeyan, S.; Potisek, S. L.; Piermattei, A.; Sijbesma, R. P. Highly Efficient Mechanochemical Scission of Silver-Carbene Coordination Polymers. *J. Am. Chem. Soc.* **2008**, *130* (45), 14968–14969. https://doi.org/10.1021/ja806887k.

(48) Groote, R.; Szyja, B. M.; Pidko, E. A.; Hensen, E. J. M.; Sijbesma, R. P. Unfolding and Mechanochemical Scission of Supramolecular Polymers Containing a Metal–Ligand Coordination Bond. *Macromolecules* **2011**, *44* (23), 9187–9195. https://doi.org/10.1021/ma201722e.

(49) Groote, R.; van Haandel, L.; Sijbesma, R. P. The Effect of Molecular Weight and Catalyst Concentration on Catalytic Activity in Mechanochemically Activated Transesterification Using Silver(I)-N-Heterocyclic Carbene Latent Catalysts. *J. Polym. Sci. Part Polym. Chem.* **2012**, *50* (23), 4929–4935. https://doi.org/10.1002/pola.26323.

(50) Michael, P.; Binder, W. H. A Mechanochemically Triggered "Click" Catalyst. *Angew. Chem. Int. Ed.* **2015**, *54* (47), 13918–13922. https://doi.org/10.1002/anie.201505678.

(51) Michael, P.; Mehr, S. K. S.; Binder, W. H. Synthesis and Characterization of Polymer Linked Copper(I) Bis(N-Heterocyclic Carbene) Mechanocatalysts. *J. Polym. Sci. Part Polym. Chem.* **2017**, *55* (23), 3893–3907. https://doi.org/10.1002/pola.28775.

(52) Funtan, S.; Michael, P.; Binder, W. H. Synthesis and Mechanochemical Activity of Peptide-Based Cu(I) Bis(N-Heterocyclic Carbene) Complexes. *Biomimetics* **2019**, *4* (1), 24. https://doi.org/10.3390/biomimetics4010024.

(53) Di Giannantonio, M.; Ayer, M. A.; Verde-Sesto, E.; Lattuada, M.; Weder, C.; Fromm, K. M. Triggered Metal Ion Release and Oxidation: Ferrocene as a

Mechanophore in Polymers. *Angew. Chem. Int. Ed.* **2018**, *57* (35), 11445–11450. https://doi.org/10.1002/anie.201803524.

(54) Cha, Y.; Zhu, T.; Sha, Y.; Lin, H.; Hwang, J.; Seraydarian, M.; Craig, S. L.; Tang, C. Mechanochemistry of Cationic Cobaltocenium Mechanophore. *J. Am. Chem. Soc.* **2021**, *143* (30), 11871–11878. https://doi.org/10.1021/jacs.1c05233.

(55) Liang, B.; Tong, R.; Wang, Z.; Guo, S.; Xia, H. High Intensity Focused Ultrasound Responsive Metallo-Supramolecular Block Copolymer Micelles. *Langmuir* **2014**, *30* (31), 9524–9532. https://doi.org/10.1021/la500841x.

(56) Hannewald, N.; Enke, M.; Nischang, I.; Zechel, S.; Hager, M. D.; Schubert, U. S. Mechanical Activation of Terpyridine Metal Complexes in Polymers. *J. Inorg. Organomet. Polym. Mater.* **2020**, *30* (1), 230–242. https://doi.org/10.1007/s10904-019-01274-1.

(57) Kersey, F. R.; Yount, W. C.; Craig, S. L. Single-Molecule Force Spectroscopy of Bimolecular Reactions: System Homology in the Mechanical Activation of Ligand Substitution Reactions. *J. Am. Chem. Soc.* **2006**, *128* (12), 3886–3887. https://doi.org/10.1021/ja058516b.

(58) Xu, D.; Craig, S. L. Strain Hardening and Strain Softening of Reversibly Cross-Linked Supramolecular Polymer Networks. *Macromolecules* **2011**, *44* (18), 7478–7488. https://doi.org/10.1021/ma201386t.

(59) Xu, D.; Liu, C.-Y.; Craig, S. L. Divergent Shear Thinning and Shear Thickening Behavior of Supramolecular Polymer Networks in Semidilute Entangled Polymer Solutions. *Macromolecules* **2011**, *44* (7), 2343–2353. https://doi.org/10.1021/ma2000916.

(60) Wang, R.; Johnson, J. A.; Olsen, B. D. Odd–Even Effect of Junction Functionality on the Topology and Elasticity of Polymer Networks. *Macromolecules* **2017**, *50* (6), 2556–2564. https://doi.org/10.1021/acs.macromol.6b01912.

(61) Beck, J. B.; Rowan, S. J. Multistimuli, Multiresponsive Metallo-Supramolecular Polymers. *J. Am. Chem. Soc.* **2003**, *125* (46), 13922–13923. https://doi.org/10.1021/ja038521k.

(62) Jackson, A. C.; Beyer, F. L.; Price, S. C.; Rinderspacher, B. C.; Lambeth, R. H. Role of Metal–Ligand Bond Strength and Phase Separation on the Mechanical

Properties of Metallopolymer Films. *Macromolecules* **2013**, *46* (14), 5416–5422. https://doi.org/10.1021/ma401077d.

(63) Beck, J. B.; Rowan, S. J. Multistimuli, Multiresponsive Metallo-Supramolecular Polymers. *J. Am. Chem. Soc.* **2003**, *125* (46), 13922–13923. https://doi.org/10.1021/ja038521k.

(64) Liu, S.-G.; Zhang, L.-P.; Liu, J.; Su, W.-Y.; Shi, X.-B. Syntheses, Crystal Structure and Luminescent Properties of Cadmium Complexes Based on 2,6-Bis(1-Phenylbenzimidazol-2-Yl)Pyridine. *Spectrochim. Acta. A. Mol. Biomol. Spectrosc.* **2012**, *97*, 464–469. https://doi.org/10.1016/j.saa.2012.06.039.

(65) Zare, D.; Doistau, B.; Nozary, H.; Besnard, C.; Guénée, L.; Suffren, Y.; Pelé, A.-L.; Hauser, A.; Piguet, C. CrIII as an Alternative to RuII in Metallo-Supramolecular Chemistry. *Dalton Trans.* **2017**, *46* (28), 8992–9009. https://doi.org/10.1039/C7DT01747B.

(66) Kose, M.; McKee, V. Mn(II) Complexes of a Tridentate Benzimidazole Ligand: Synthesis, Structural Characterisation and Catalase Mimetic Studies. *Polyhedron* **2014**, *75*, 30–39. https://doi.org/10.1016/j.poly.2014.03.012.

(67) Pan, R.-K.; Song, J.-L.; Li, G.-B.; Lin, S.-Q.; Liu, S.-G.; Yang, G.-Z. Copper(II), Cobalt(II) and Zinc(II) Complexes Based on a Tridentate Bis(Benzimidazole)Pyridine Ligand: Synthesis, Crystal Structures, Electrochemical Properties and Antitumour Activities. *Transit. Met. Chem.* **2017**, *42* (3), 253–262. https://doi.org/10.1007/s11243-017-0129-9.

(68) Yuan, L.-Z.; Ge, Q.; Zhao, X.-F.; Ouyang, Y.; Li, S.-H.; Xie, C.-Z.; Xu, J.-Y. Syntheses, Crystal Structures, and DNA Bindings of Co(III) and Ni(II) Complexes Based on 2,6-Bis(Benzimidazol- 2-Yl)-4-Hydroxypyridine Ligand. *Synth. React. Inorg. Met.-Org. Nano-Met. Chem.* **2014**, *44* (8), 1175–1182. https://doi.org/10.1080/15533174.2013.797459.

(69) Shinomiya, T.; Ozawa, H.; Mutoh, Y.; Haga, M. A Redox-Active Porous Coordination Network Film Based on a Ru Complex as a Building Block on an ITO Electrode. *Dalton Trans.* **2013**, *42* (45), 16166–16175. https://doi.org/10.1039/C3DT51484F.

(70) Shao, J.-Y.; Zhong, Y.-W. Monometallic Osmium(II) Complexes with Bis(N-Methylbenzimidazolyl)Benzene or -Pyridine: A Comparison Study with

Ruthenium(II) Analogues. *Inorg. Chem.* **2013**, *52* (11), 6464–6472. https://doi.org/10.1021/ic400385b.

(71) Chan, M. H.-Y.; Leung, S. Y.-L.; Yam, V. W.-W. Controlling Self-Assembly Mechanisms through Rational Molecular Design in Oligo(p-Phenyleneethynylene)-Containing Alkynylplatinum(II) 2,6-Bis(N-Alkylbenzimidazol-2′-Yl)Pyridine Amphiphiles. *J. Am. Chem. Soc.* **2018**, *140* (24), 7637–7646. https://doi.org/10.1021/jacs.8b03628.

(72) André, N.; Jensen, T. B.; Scopelliti, R.; Imbert, D.; Elhabiri, M.; Hopfgartner, G.; Piguet, C.; Bünzli, J.-C. G. Supramolecular Recognition of Heteropairs of Lanthanide Ions: A Step toward Self-Assembled Bifunctional Probes. *Inorg. Chem.* **2004**, *43* (2), 515–529. https://doi.org/10.1021/ic0351996.

(73) Piguet, C.; Williams, A. F.; Bernardinelli, G.; Buenzli, J. C. G. Structural and Photophysical Properties of Lanthanide Complexes with Planar Aromatic Tridentate Nitrogen Ligands as Luminescent Building Blocks for Triple-Helical Structures. *Inorg. Chem.* **1993**, *32* (19), 4139–4149. https://doi.org/10.1021/ic00071a029.

(74) Neumann, L. N.; Gunkel, I.; Barron, A.; Oveisi, E.; Petzold, A.; Thurn-Albrecht, T.; Schrettl, S.; Weder, C. Structure–Property Relationships of Microphase-Separated Metallosupramolecular Polymers. *Macromolecules* **2020**, *53* (13), 5068–5084. https://doi.org/10.1021/acs.macromol.0c00876.

(75) Thordarson, P. Determining Association Constants from Titration Experiments in Supramolecular Chemistry. *Chem. Soc. Rev.* **2011**, *40* (3), 1305–1323. https://doi.org/10.1039/C0CS00062K.

(76) Bénech, J.-M.; Piguet, C.; Bernardinelli, G.; Bünzli, J.-C. G.; Hopfgartner, G. Square-Planar Rhodium(I) Complexes with Aromatic Bent Terdentate Nitrogen Ligands as Candidates for Rod-like Extended Materials. *J. Chem. Soc. Dalton Trans.* **2001**, No. 5, 684–689. https://doi.org/10.1039/B009051O.

(77) Pan, R.; Li, G.; Liu, S.; Zhou, X.; Yang, G. Synthesis, Crystal Structure, Electrochemical Property, and Antioxidant Activity of Copper(II) Complex Based on 4-Butyloxy-2,6-Bis(1-Methyl-2-Benzimidazolyl)Pyridine. *Monatshefte Für Chem. - Chem. Mon.* **2016**, *147* (7), 1189–1196. https://doi.org/10.1007/s00706-015-1632-3.

(78) Gong, D.; Jia, X.; Wang, B.; Zhang, X.; Jiang, L. Synthesis, Characterization, and Butadiene Polymerization of Iron(III), Iron(II) and Cobalt(II) Chlorides Bearing 2,6-Bis(2-Benzimidazolyl)Pyridyl or 2,6-Bis(Pyrazol)Pyridine Ligand. *J. Organomet. Chem.* **2012**, *702*, 10–18. https://doi.org/10.1016/j.jorganchem.2011.11.025.

(79) Kotova, O.; Daly, R.; dos Santos, C. M. G.; Kruger, P. E.; Boland, J. J.; Gunnlaugsson, T. Cross-Linking the Fibers of Supramolecular Gels Formed from a Tripodal Terpyridine Derived Ligand with d-Block Metal Ions. *Inorg. Chem.* **2015**, *54* (16), 7735–7741. https://doi.org/10.1021/acs.inorgchem.5b00626.

(80) Allmann, R.; Henke, W.; Reinen, D. Presence of a Static Jahn-Teller Distortion in Copper(II) Terpyridine Complexes. 1. Crystal Structure of Diterpyridinecopper(II) Nitrate. *Inorg. Chem.* **1978**, *17* (2), 378–382. https://doi.org/10.1021/ic50180a040.

(81) Sanni, S. B.; Behm, H. J.; Beurskens, P. T.; Albada, G. A. van; Reedijk, J.; Lenstra, A. T. H.; Addison, A. W.; Palaniandavar, M. Copper(II) and Zinc(II) Co-Ordination Compounds of Tridentate Bis(Benzimidazole)Pyridine Ligands. Crystal and Molecular Structures of Bis[2,6-Bis(1′-Methylbenzimidazol-2′-Yl)Pyridine]Copper(II) Diperchlorate Monohydrate and (Acetonitrile)[2,6-Bis(Benzimidazol-2′-Yl)Pyridine](Perchlorato)Copper(II) Perchlorate. *J. Chem. Soc. Dalton Trans.* **1988**, No. 6, 1429–1435. https://doi.org/10.1039/DT9880001429.

(82) Skoog, D. A.; Leary, J. J. *Principles of Instrumental Analysis*; Saunders College Pub., 1992.

(83) Yarusso, D. J.; Cooper, S. L. Microstructure of Ionomers: Interpretation of Small-Angle x-Ray Scattering Data. *Macromolecules* **1983**, *16* (12), 1871–1880. https://doi.org/10.1021/ma00246a013.

(84) Flory, P. J. Molecular Theory of Rubber Elasticity. *Polym. J.* **1985**, *17* (1), 1–12. https://doi.org/10.1295/polymj.17.1.

(85) Lin, T.-S.; Wang, R.; Johnson, J. A.; Olsen, B. D. Revisiting the Elasticity Theory for Real Gaussian Phantom Networks. *Macromolecules* **2019**, *52* (4), 1685–1694. https://doi.org/10.1021/acs.macromol.8b01676.

(86) Zhong, M.; Wang, R.; Kawamoto, K.; Olsen, B. D.; Johnson, J. A. Quantifying the Impact of Molecular Defects on Polymer Network Elasticity. *Science* **2016**, *353* (6305), 1264–1268. https://doi.org/10.1126/science.aag0184.

(87) Ferry, J. D. *Viscoelastic Properties of Polymers*; Wiley, 1970.

(88) Ronan, S.; Alshuth, T.; Jerrams, S.; Murphy, N. Long-Term Stress Relaxation Prediction for Elastomers Using the Time–Temperature Superposition Method. *Mater. Des.* **2007**, *28* (5), 1513–1523. https://doi.org/10.1016/j.matdes.2006.03.009.

(89) Rubinstein, M.; Semenov, A. N. Dynamics of Entangled Solutions of Associating Polymers. *Macromolecules* **2001**, *34* (4), 1058–1068. https://doi.org/10.1021/ma0013049.

(90) Ramaraj, B. Crosslinked Poly(Vinyl Alcohol) and Starch Composite Films. II. Physicomechanical, Thermal Properties and Swelling Studies. *J. Appl. Polym. Sci.* **2007**, *103* (2), 909–916. https://doi.org/10.1002/app.25237.

(91) Constable, E. C.; Housecroft, C. E.; Price, J. R.; Zampese, J. A. When Five Are Six: The Myth of Five-Coordinate Copper(II) in Supramolecular Chemistry. *CrystEngComm* **2010**, *12* (10), 3163–3171. https://doi.org/10.1039/C0CE00019A.

(92) Brachňaková, B.; Kožíšková, J. A.; Kožíšek, J.; Melníková, E.; Gál, M.; Herchel, R.; Dubaj, T.; Šalitroš, I. Low-Spin and Spin-Crossover Iron(II) Complexes with Pyridyl-Benzimidazole Ligands: Synthesis, and Structural, Magnetic and Solution Study. *Dalton Trans.* **2020**, *49* (48), 17786–17795. https://doi.org/10.1039/D0DT03497E.

(93) Smith, N. L.; Coukouma, A. E.; Wilson, D. C.; Ho, B.; Gray, V.; Asher, S. A. Stimuli-Responsive Pure Protein Organogel Sensors and Biocatalytic Materials. *ACS Appl. Mater. Interfaces* **2020**, *12* (1), 238–249. https://doi.org/10.1021/acsami.9b18191.

(94) Esposito, C. L.; Kirilov, P.; Roullin, V. G. Organogels, Promising Drug Delivery Systems: An Update of State-of-the-Art and Recent Applications. *J. Controlled Release* **2018**, *271*, 1–20. https://doi.org/10.1016/j.jconrel.2017.12.019.

(95) Montero, D. A.; Arellano, C.; Pardo, M.; Vera, R.; Gálvez, R.; Cifuentes, M.; Berasain, M. A.; Gómez, M.; Ramírez, C.; Vidal, R. M. Antimicrobial Properties of a Novel Copper-Based Composite Coating with Potential for Use in Healthcare Facilities. *Antimicrob. Resist. Infect. Control* **2019**, *8* (1), 3. https://doi.org/10.1186/s13756-018-0456-4.

(96) Beeton, M. L.; Aldrich-Wright, J. R.; Bolhuis, A. The Antimicrobial and Antibiofilm Activities of Copper(II) Complexes. *J. Inorg. Biochem.* **2014**, *140*, 167–172. https://doi.org/10.1016/j.jinorgbio.2014.07.012.

(97) Zhang, X.; Kyriakos, K.; Rikkou-Kalourkoti, M.; Kitiri, E. N.; Patrickios, C. S.; Papadakis, C. M. Amphiphilic Single and Double Networks: A Small-Angle X-Ray Scattering Investigation. *Colloid Polym. Sci.* **2016**, *294* (6), 1027–1036. https://doi.org/10.1007/s00396-016-3856-0.

Biography

Patricia Nicole Johnson is a chemist and materials scientist who received her Bachelor of Science from the University at Buffalo in 2016 and attended Duke University for her PhD in chemistry from 2016 to 2022. During her graduate career, she was awarded the NDSEG Fellowship and a Fulbright Student Research Fellowship to study in Switzerland.